High Power Capacitive Power Transfer for Electric Vehicle Charging Applications

by

Fei Lu

A dissertation submitted in partial fulfillment
of the requirements for the degree of
Doctor of Philosophy
(Electrical Engineering: Systems)
in The University of Michigan
2017

Doctoral Committee:

Professor Chris Mi, Co-Chair
Associate Professor Heath Hofmann, Co-Chair
Professor Anthony Grbic
Professor Ian Hiskens
Professor Huei Peng

Fei Lu

feilu@umich.edu

ORCID ID: 0000-0002-0539-5887

DEDICATION

To my wife, Hua, and my son, Leon, with full of love
And to my parents, for all the support and understanding

ACKNOWLEDGMENTS

Life is a journey, and the PhD study is one of the most challenging adventures and explorations. All the time through five years and all the way across Ann Arbor, Dearborn, and San Diego, with happiness and pain, it finally will be completed in the next month. It is not the end of my academic learning, but the beginning of next-stage more fantastic trip.

I would like to express my deep gratitude to my advisors, Professor Mi and Professor Hofmann, for their generosity, guidance, and mentorship in my difficult time. I cannot come to this graduation stage without their help. They have been teaching me the way to deal with challenges not only in studying and researching, but also in the real life. I will always remember that winter day when Professor Hofmann carried me from Ann Arbor to Dearborn to first meet Professor Mi and continue my academic future. It is my fortune and honor to have this opportunity to study and work with them from all this time.

I also would like to thank Professor Grbic, Professor Hiskens, and Professor Peng, not only for serving in my committee, but also for providing me so many valuable advices to improve my researches. This dissertation wok becomes more complete, logical, and convincing with all their suggestions and help. I would like to thank all the Professors in University of Michigan who have taught me courses in the past few years. I have learnt both the mathematical tools and the methods to solve practical problems from all these courses. I would like to thank Professor Su in Dearborn for his generous financial support in the last year.

Additionally, I would like to thank my colleagues for their help in my researches and experiments. They are Jun Hou, Kan Zhou, Tianze Kan, Weihan Li, Wei Zhang, Shuai Mao, Xianzhi Gong, Chenwen You, Bing Xia, Yunlong Shang, and Junfeng Yang. Especially, I would like to thank Junjun Deng for introducing me into the world of wireless power transfer.

Finally, it comes to the great time to express gratitude to my wife, dear Hua. She is the person who gave me hints when I was stocked in a question; she is the person who corrected all my wrongs at the right time; she is the person who built up all my Maxwell simulation; she is the person who set up all the high-power prototypes for me; she is the person who stayed up all the night to run the experiments for me; she is the person who put her hand between the metal plates to test the safety of my capacitive power transfer system; she is the person who kept helping me do experiments until one hour before she gave birth to our baby. She is a great colleague, a considerate wife, and a brave mother. I would like to share the authorship of this dissertation with her. I also would like to thank my son, Leon, my perfect graduation gift of my PhD study, for all the happiness he has brought to our family. I also would like to thank my parents and my brother. Five years studying abroad have missed too much time to share with them. Thanks for all the support and understanding during this long time.

TABLE OF CONTENTS

DEDICATION ii

ACKNOWLEDGMENTS iii

LIST OF FIGURES viii

LIST OF TABLES xi

LIST OF ABBREVIATIONS xii

ABSTRACT xiii

CHAPTER

I. INTRODUCTION 1

1.1. Background of Wireless Power Transfer 1

1.1.1. Category of WPT Systems 1

1.1.2. Comparison of WPT Technologies 1

1.2. Development of Electric Vehicle Charging Technology 7

1.2.1. Conductive Charging 7

1.2.2. Inductive Charging 9

1.3. Motivation of Capacitive Power Transfer 12

1.3.1. PWM-Converter-Based CPT System 12

1.3.2. Power Amplifier-Based CPT System 13

1.3.3. Full-Bridge Inverter based CPT System 14

1.4. Challenges in Capacitive Power Transfer 15

1.4.1. Transfer Distance, Power, and Efficiency 15

1.4.2. Dynamic CPT System 16

1.4.3. Power Density and Electric Field Emission 17

1.5. Contributions of This Dissertation 18

1.6. References 19

II. DOUBLE-SIDED LCLC-COMPENSATED CPT SYSTEM 28

2.1. Introduction 28
2.2. Capacitive Coupler Design 29
2.3. LCLC Compensation Circuit 33
2.3.1. Circuit Topology 33
2.3.2. Circuit Working Principle 34
2.3.3. Output Power Calculation 36
2.3.4. CLLC Compensation Circuit 38
2.4. Example Double-Sided LCLC-Compensated CPT System 39
2.4.1. Circuit Parameter Design 39
2.4.2. Circuit Simulation 41
2.5. Experimental Results of Double-Sided LCLC-Compensated CPT System 42
2.5.1. Experimental Setup 42
2.5.2. Experimental Results 43
2.6. Discussion: Comparison between LC and LCLC Compensation 47
2.7. Conclusion 52
2.8. References 52

III. IPT AND CPT COMBINED SYSTEM 54

3.1. Introduction 54
3.2. Inductive and Capacitive Coupler Design 55
3.2.1 Inductive Coupler Design 55
3.2.2 Capacitive Coupler Design 58
3.3. LC-Compensated IPT and CPT Combined System 62
3.3.1 Circuit Topology 62
3.3.2 Circuit Working Principle 63
3.3.3 System Power Calculation 65
3.4. Design Example of an LC-Compensated IPT and CPT Combined System 67
3.4.1 Power Ratio of IPT and CPT Systems 67
3.4.2. System Parameters Design 68
3.4.3. System Simulation 70
3.5. Experimental Results 71
3.5.1. Experimental setup 72
3.5.2. Well-Aligned Experiment 73
3.5.2. Misalignment Experiment 74
3.5.3. Comparison of Modeled and Experimental Results 75
3.6. Conclusion 78
3.7. References 79

IV. DYNAMIC CAPACITIVE POWER TRANSFER 81

4.1. Introduction 81
4.2. Dynamic Capacitive Coupler Design 83

4.2.1 Coupler Structure 83
4.2.2 Circuit Model 85
4.2.3 Maxwell Simulation 86
4.3 An Example of LCLC-Compensated Dynamic CPT System 88
4.3.1 Circuit Topology 88
4.3.2 Circuit Parameters Design 90
4.3.3 Circuit Simulation 90
4.4 Experimental Results 91
4.4.1. Experimental Setup 91
4.4.2. Stationary Experiments 92
4.4.3. Dynamic Experiments 94
4.4.4. Discussion: Challenges in Dynamic CPT System 96
4.5. Conclusion 99
4.6. References 99

V. SAFETY ISSUE AND FOREIGN OBJECT IMPACT 102

5.1. Introduction 102
5.2. Voltage Stresses between Metal Plates 103
5.2.1. General Mathematical Model of CPT System Power 103
5.2.2. General Mathematical Model of Plate Voltages 106
5.2.3. Plate Voltages in an LCLC-Compensated CPT System 109
5.3. Electric Field Emissions 112
5.3.1. Electric Fields Emission of Horizontal Plates 112
5.3.2. Electric Field Emissions of Vertical Plates 115
5.4. Foreign Object Influence to CPT System 119
5.4.1. Position of Foreign Objects 119
5.4.2. Metallic Foreign Object Influence to CPT System 120
5.4.3. Dielectric Foreign Object Influence to CPT System 122
5.5. CPT System Influence to Foreign Object 125
5.5.1. CPT System Influence to Metallic Foreign Object 125
5.5.2. Conductive Power losses in Foreign Object 127
5.6. Conclusion 130
5.7. References 131

VI. CONCLUSIONS AND FUTURE WORK 133

6.1. Conclusions 133
6.2. Future Works 135

LIST OF FIGURES

Fig. 1-1. Category of wireless power transfer systems 1
Fig. 1-2. Structure of an acoustic power transfer system 2
Fig. 1-3. Structure of an optical power transfer system 3
Fig. 1-4. Structure of a microwave power transfer system 4
Fig. 1-5. Structure of an inductive power transfer system 5
Fig. 1-6. Structure of a capacitive power transfer system 6
Fig. 1-7. Structures of conductive charging systems for electric vehicles 8
Fig. 1-8. Structures of an inductive charging system for electric vehicles 9
Fig. 1-9. Circuit topologies of capacitor compensation 10
Fig. 1-10. Circuit topologies of inductor-capacitor compensations 11
Fig. 1-11. CPT system based on a Sepic converter 13
Fig. 1-12. CPT system based on a class E converter 14
Fig. 1-13. CPT system based on a full-bridge inverter with series inductors 15

Fig. 2-1. Structure and dimension of a horizontally arranged capacitive coupler 29
Fig. 2-2. Simplified circuit model of a horizontally arranged capacitive coupler 30
Fig. 2-3. Maxwell-simulated coupling capacitance C_{M1} at different plate lengths l_1 30
Fig. 2-4. Maxwell simulated coupling capacitance C_{M1} at different x misalignments 32
Fig. 2-5. Maxwell simulated coupling capacitance C_{M1} at different air-gap distances d 32
Fig. 2-6. Circuit topology of a double-sided LCLC-compensated CPT system 33
Fig. 2-7. Fundamental harmonics approximation of a double-sided LCLC-compensated CPT system 34
Fig. 2-8. Circuit topology of a double-sided CLLC-compensated CPT system 38
Fig. 2-9. Parameters of LCLC compensation circuit at different k_C 40
Fig. 2-10. LTspice-simulated input and output waveforms of and LCLC-compensated CPT system 41
Fig. 2-11. Prototype of a double-sided LCLC-compensated CPT system 42
Fig. 2-12.Experimental results of the LCLC-compensated CPT system at well-aligned position 43
Fig. 2-13. Power losses distributions among circuit components in full-power and well-aligned case 44
Fig. 2-14. Experimental results of LCLC-compensated CPT system at x misalignments 45
Fig. 2-15. Experimental results of LCLC-compensated CPT system at air-gap distance d variations 46

Fig. 2-16. Circuit topology of a double-sided LC-compensated CPT system 47
Fig. 2-17. Theoretical Maximum achievable efficiency of LC- and LCLC-compensated CPT networks 50
Fig. 2-18. Comparison of efficiencies of LC- and LCLC-compensation networks 51

Fig. 3-1. Structure and dimensions of an inductive coupler 56
Fig. 3-2. Maxwell-simulated equivalent parameters of an inductive coupler at different dimensions 57
Fig. 3-3. Structure and dimensions of a vertically arranged capacitive coupler 59
Fig. 3-4. Circuit model of a vertically arranged capacitive coupler 60
Fig. 3-5. Maxwell-simulated equivalent capacitances of a capacitive coupler at different dimensions 61
Fig. 3-6. Circuit topology of a double-sided LC-compensated IPT and CPT combined system .. 62
Fig. 3-7. Equivalent circuit of a double-sided LC-compensated IPT and CPT combined system 63
Fig. 3-8. Fundamental harmonics approximation of an LC-compensated IPT and CPT combined system 64
Fig. 3-9. Relationship of circuit parameters in an IPT and CPT combined system 69
Fig. 3-10. Maxwell-simulated normalized C_M and k at different misalignments 70
Fig. 3-11. LTspice-simulated waveforms of an LC-compensated IPT and CPT combined system 71
Fig. 3-12. Experimental prototype of an IPT and CPT combined system 72
Fig. 3-13. Experimental results of an IPT and CPT combined system at well-aligned position .. 73
Fig. 3-14. Output power and efficiency of an IPT and CPT combined system 74
Fig. 3-15. Comparison of waveforms in simulated and experimental results 76
Fig. 3-16. Comparison of experimental and calculated power 77

Fig. 4-1. Structure of dynamic charging system with different transmitter lengths 82
Fig. 4-2. Structure and dimensions of a capacitive coupler for dynamic charging 83
Fig. 4-3. Behavior source model of the capacitive coupler 85
Fig. 4-4. Maxwell-simulated equivalent capacitances at different receiver position y 87
Fig. 4-5. Maxwell-simulated equivalent capacitances at different x misalignment 88
Fig. 4-6. Circuit topology of a double-sided LCLC-compensated dynamic CPT system 88
Fig. 4-7. Equivalent circuit of a double-sided LCLC-compensated dynamic CPT system 89
Fig. 4-8. LTspice-simulated input and output waveforms of a dynamic CPT system 91
Fig. 4-9. Prototype of a double-sided LCLC-compensated dynamic CPT system 92
Fig. 4-10. Experimental results of the dynamic CPT system at well-aligned position when y=450mm 93
Fig. 4-11. Estimated power loss distribution in the dynamic CPT system 93
Fig. 4-12. Experimental dc-dc efficiency at different output power 94
Fig. 4-13. Experimental and simulated output power at different position y 95
Fig. 4-14. Experimental and simulated output power at different x misalignment 95

Fig. 4-15. A long-track CPT system with multiple receivers at different positions 96
Fig. 4-16. Maxwell-simulated electric field emission of the designed dynamic CPT system 97
Fig. 4-17. Relationship between switching frequency f_{sw} and quarter wavelength λ/4 98

Fig. 5-1. A general circuit topology of a CPT system with behavior source model 104
Fig. 5-2. The apparent power S_M transferred to the secondary side 105
Fig. 5-3. The relationship between reactive power Q_M and active power P_M 105
Fig. 5-4. A general circuit topology of a CPT system with six-capacitor model 106
Fig. 5-5. Calculated voltage stresses between metal plates when P_M=3.0 kW and f_{sw}=1MHz ... 109
Fig. 5-6. Circuit topology of an LCLC-compensated CPT system with behavior source model 109
Fig. 5-7. Phase different θ and sin(θ) at different k_C in LCLC-Compensated CPT system 110
Fig. 5-8. Calculated voltages in an LCLC-compensated CPT system when C_M=18.4 pF and k_C=0.15 111
Fig. 5-9. Electric field emission of a horizontal capacitive coupler 113
Fig. 5-10. Electric field vector distribution in a horizontal capacitive coupler when P_M=3.0 kW 113
Fig. 5-11. Electric field emission of a horizontal coupler at misalignment cases 114
Fig. 5-12. Calculated voltages in an LCLC-compensated CPT system when C_M=11.2 pF and k_C=0.094 115
Fig. 5-13. Electric field emission of a vertical coupler 116
Fig. 5-14. Electric field vector distribution in a vertical capacitive coupler when P_M=3.0 kW ..116
Fig. 5-15. Electric field emission of a vertical coupler at 300 mm *x* misalignment 117
Fig. 5-16. Electric field emissions of a six-plate coupler when P_M=3.0kW 118
Fig. 5-17. Typical positions of a foreign object in a horizontal coupler 119
Fig. 5-18. Electric field emissions of a horizontal coupler with a 610mm×610mm aluminum plate at position A3 121
Fig. 5-19. A dielectric foreign object at position A2 around a capacitive coupler 122
Fig. 5-20. Maxwell-simulated capacitance C_{M1} with dielectric foreign objects 123
Fig. 5-21. A dielectric foreign object in a horizontal capacitive coupler 123
Fig. 5-22. Maxwell-simulated equivalent capacitances of a horizontal coupler with a dielectric foreign object 124
Fig. 5-23. A symmetric circuit topology to reduce current flowing through human body 126
Fig. 5-24. Charge relaxation time of a foreign object at different ε_r and σ_0 127
Fig. 5-25. Power losses in a foreign object at different ε_r and σ_0 129

LIST OF TABLES

Table I-1. Comparison of WPT technologies [1] 6

Table II-1. Dimensions of a horizontally arranged capacitive coupler 31
Table II-2. System specifications and circuit parameters 40

Table III-1. System parameters of a 3.0kW IPT and CPT combined system 70

Table IV-1. Dimensions of a capacitive coupler for dynamic power transfer 84
Table IV-2. Maxwell-simulated capacitances at the middle position when y=450mm 86
Table IV-3. System specifications and circuit parameter values 90

Table V-1. Voltages between metal plates 108
Table V-2. Simplified voltages between metal plates in a symmetric coupler 108
Table V-3. Influence of foreign aluminum plate to equivalent capacitances 120

LIST OF ABBREVIATIONS

EMI Electromagnetic Interference

CPT Capacitive Power Transfer

FEA Finite Element Analysis

FHA Fundamental Harmonics Approximation

IC Integrated Circuits

ICNIRP International Commission on Non-Ionizing Radiation Protection

IEC International Electrotechnical Commission

IPT Inductive Power Transfer

OLEV On-line Electric Vehicle

PP Parallel-Parallel

PS Parallel-Series

PV Photovoltaic

PWM Pulse Width Modulation

RF Radio Frequency

SiC Silicon Carbide

SP Series-Parallel

SS Series-Series

WPT Wireless Power Transfer

ABSTRACT

Capacitive power transfer (CPT) technology is an effective way to charge electric vehicles, in which electric fields between metal plates are used to transfer power. Compared to the conventional inductive power transfer (IPT) system, a CPT system has three advantages: it does not generate eddy-current loss in nearby metal objects; it can reduce the system weight and cost; it has better misalignment performance. However, the coupling capacitance in a CPT system is usually in the pF range, which limits the CPT system power and efficiency.

Through overcoming the limitation of small capacitance in a CPT system, this dissertation has achieved three breakthroughs in CPT technology: the system power is increased from several tens of watts to several kW; the transfer distance is increased from less than 1 mm to hundreds of mm; the transfer efficiency is increased from about 30% to over 90%.

A double-sided LCLC compensation circuit has been proposed to realize high-power and long-distance capacitive power transfer. The compensation circuit provides resonances with the coupling capacitance, and increases the voltages on metal plates to kV level to achieve kW power transfer. A prototype has been constructed and validates the proposed circuit. Experimental results show that the prototype realizes 2.4 kW power transfer across an air-gap distance of 150 mm with a dc-dc efficiency of 90.8%. The experiments also show that the CPT system has better misalignment performance than the conventional IPT system.

An IPT-CPT combined system has also been proposed to integrate the IPT and CPT technology together. The combination can increase the efficiency of the CPT system, and improve the misalignment performance of the IPT system. A prototype has been constructed to validate the combined idea. Experimental results show that the prototype realizes 2.84 kW power transfer across an air-gap distance of 150 mm with a dc-dc efficiency of 94.4%.

Using the designed LCLC compensation circuit, a dynamic CPT system has been proposed to realize power transfer to receivers in moving status. A long-track coupler structure is used to reduce the pulsation of received power. A prototype has been constructed to validate dynamic charging. Experimental results show that the prototype realizes 154W power transfer across an air-gap distance of 50 mm with a dc-dc efficiency of 85.4%.

Considering practical applications, the safety issues and foreign object influence have been studied in this dissertation. The high voltage issue can be solved by reliable insulation, and the electric field emissions can be reduced through capacitive coupler structure design. The foreign object, either metallic or dielectric, can influence the coupling capacitances in a CPT system depends on the position and size. The CPT system can also influence the voltage and power loss in the foreign object.

To sum up, this dissertation has demonstrated that the CPT technology is a good solution to realize the charging of electric vehicles. In future work, the power density and efficiency of the CPT system will be further improved to make it more competitive with the inductive and conductive charging technology.

CHAPTER I

INTRODUCTION

1.1. Background of Wireless Power Transfer

1.1.1. Category of WPT Systems

Wireless power transfer (WPT) is a technology that can transfer electric power without direct metal-to-metal contact, but rather with the energy contained in fields, which can be acoustic or electromagnetic [1]-[3]. Taking advantages of these fields, the WPT systems can be classified as shown in Fig. 1-1, listed as acoustic power transfer [4], optical power transfer [5], microwave power transfer [6], inductive power transfer (IPT) [7], and capacitive power transfer (CPT) [8].

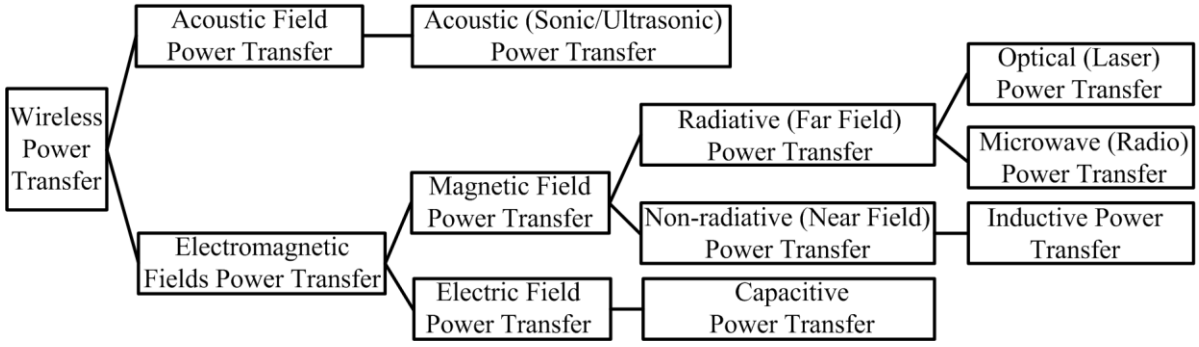

Fig. 1-1. Category of wireless power transfer systems

1.1.2. Comparison of WPT Technologies

A. Acoustic Power Transfer

Acoustic power transfer systems utilize sonic and ultrasonic sound waves to transfer power, and their structure is shown in Fig. 1-2 [9], [10]. At the primary side, an electro acoustic device,

typically a piezoelectric device is used to convert electric power into acoustic power and transmit it through the medium. At the secondary side, another electro acoustic device converts the acoustic power back into electrical form and provides it to the load. In some cases, an intermediate matching layer is placed between the transducer and the medium to match the mechanical impedance and thereby maximize the output power [11], [12]. Impedance matching can also be realized by the electric circuit at the secondary side, where a dc-dc converter is usually connected between the output rectifier and the load [13], [14].

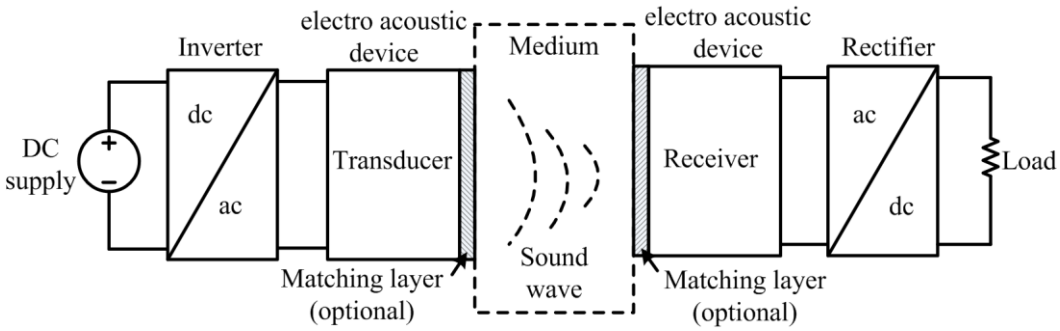

Fig. 1-2. Structure of an acoustic power transfer system

The advantage of acoustic power transfer technology is that it is relatively lies in its safety to the human body, and can penetrate through metal barriers. Research has been done in both low and high power applications, such as implantable medical devices [15], energy harvesting [16], underwater sensor networks [17], and through-metal power transfer [18]. Depending on the mechanical properties of the electro acoustic devices, the transmission frequency varies from the several tens of kHz to the MHz level. The low power system usually has an efficiency lower than 1%. When the size of the device increases, the system power can reach 1 kW with 80% efficiency in high power applications [19], [20]. However, the cost of the device also increases rapidly with its size, which limits its commercial application in high power areas.

B. Optical Power Transfer

Optical power transfer system utilizes laser light, which is essentially high frequency electromagnetic waves in the THz range, to transfer power, and its structure is shown in Fig. 1-3 [21], [22]. At the primary side, the laser generator is used to convert electric power to light. At

the secondary side, a photovoltaic (PV) device receives the light and converts it back into electric form. Laser generator types include gas laser, crystal lasers, active fiber lasers, and semiconductor diode lasers, in which the diode laser has smaller size and higher efficiency [23].

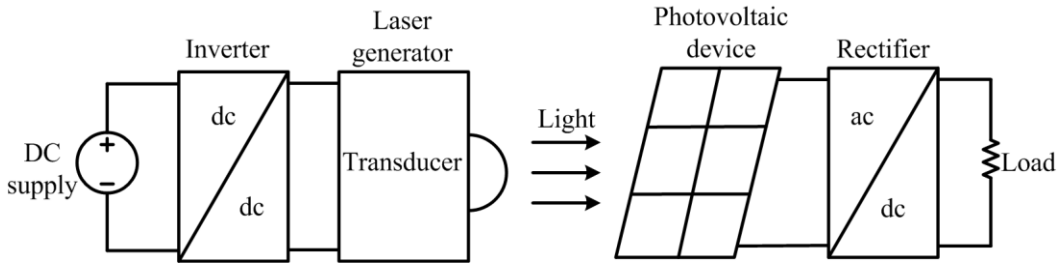

Fig. 1-3. Structure of an optical power transfer system

The most significant advantage of optical power transfer technology is its effective collimation ability, which means there is little power leakage from the beaming path [24]. This technology was initially developed for outer space applications of spacecraft and satellites [25]. Recently, it has been extended to the underwater environment [26] and low-power implantable biomedical devices [27]. With the development of semiconductor technology, the electric-to-optical efficiency of a laser diode can reach 50% [28], and the optical-to-electric efficiency can reach 64% [29], which makes the overall dc-dc efficiency about 30%. Another critical concern is the danger to human safety, particularly eye protection [30]. Therefore, laser systems usually work in discontinuous mode to limit the power density of light [23]. Considering the power and efficiency limitations, significant effort is still required to make this technology practical in more applications.

C. Microwave Power Transfer

Microwave power transfer is also called radio frequency (RF) power transfer, which utilizes electromagnetics wave in the GHz range, as shown in Fig. 1-4 [31]. An antenna acts as the power transducer at the primary side, and a rectenna acts as the receiver at the secondary side [32]. In this system, the RF inverter and rectifier are both high-frequency resonant converters, and their impedances are designed to match the impedances of the antenna and rectenna to maximize the system power [33].

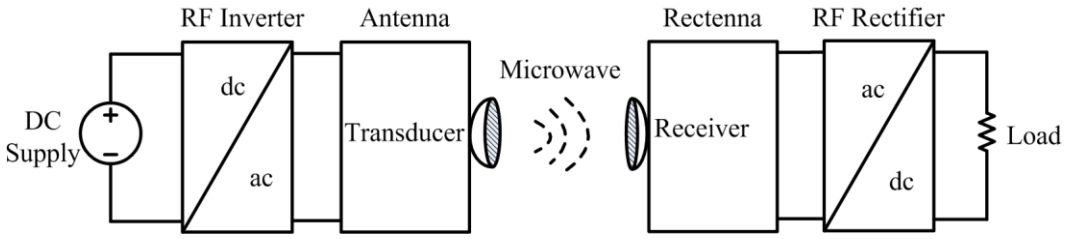

Fig. 1-4. Structure of a microwave power transfer system

The advantage of microwave power transfer technology is its ability to transfer power over a long distance property. In low-power applications, a large-scale cellular network has realized effective data and power transfer simultaneously [34], and a wireless sensor network has been self-powered from microwaves in free space [35], [36]. In high-power applications, reflection tubes are introduced to realize good collimation [37], and 30 kW power has been transferred through a distance of 1.6 km with a dc-dc efficiency of approximately 6.7% [38]. Since the 1990s, novel semiconductor materials, such as gallium nitride (GaN), have been used to improve the system efficiency [39]. Because of the high power capability, microwave power transfer can also be used in vehicle charging applications [40]. However, the size and cost of current microwave power transfer systems are still not acceptable for commercial applications, and human safety is also an important concern [41], [42].

D. Inductive Power Transfer

Inductive power transfer (IPT) system utilizes non-radiative magnetic fields, typically in the kHz to MHz range, to realize power transfer. Since there are resonances in the circuit, it is also called magnetic resonance [43], [44]. The system structure is shown in Fig. 1-5 [45], [46]. Two planar coils form a loosely-coupled transformer, which is called a magnetic or inductive coupler, to generate magnetic fields. Since there is a large air-gap between the coils, their magnetic coupling is relatively low [47]. Therefore, magnetic ferrites can be used to enhance the coupling. At both the primary and secondary sides, compensation networks, including inductors and capacitors, are required to resonate with the coils. The resonances can significantly increase the currents flowing through the coils, and generate stronger magnetic fields [48], [49]. In this way, sufficient power transfer is achieved.

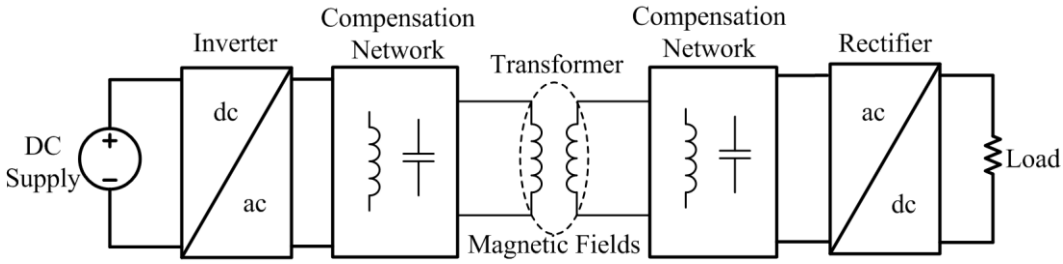

Fig. 1-5. Structure of an inductive power transfer system

The advantage of inductive power transfer is its high efficiency and high power capability, and it has been the most commercially successful WPT technology. Its application areas widely include integrated circuits (IC) [50], biomedical devices [51], sensor networks [52], portable electronic products [53], and electric vehicles [54]. The system efficiency is closely related to the circuit resonances and load condition [55], and it can achieve over 90% dc-dc efficiency when the transfer distance is in the hundreds of mm range [56]. The distance can be further extended using intermediate resonant coils without significant influence to the efficiency [57]. Three-dimensional (3D) omnidirectional power transfer can also be realized with an optimized transmitter structure [58]. Moreover, with the shared channel of the coils, parallel transmission of power and data can be achieved through the inductive coupling [59]-[61]. However, in practical application, safety concerns regarding the field emissions, and overheating caused by eddy-current losses in nearby metal objects are becoming limitations [62], [63].

E. Capacitive Power Transfer

Capacitive power transfer (CPT) systems utilize high-frequency electric fields to transfer power. A common system structure is shown in Fig. 1-6 [64], [65]. Two pairs of metal plates form two capacitors, which is also called capacitive coupler, to establish the electric fields [66]. The two capacitors provide a power flow loop from the input source to the output load. The coupling capacitances depend on the plate area, plate distance, and the dielectric material between the plates [67]. Similar to the IPT system, two compensation networks are required at both the primary and secondary sides to resonate with the capacitors to increase the voltages on the plates for power transfer [68].

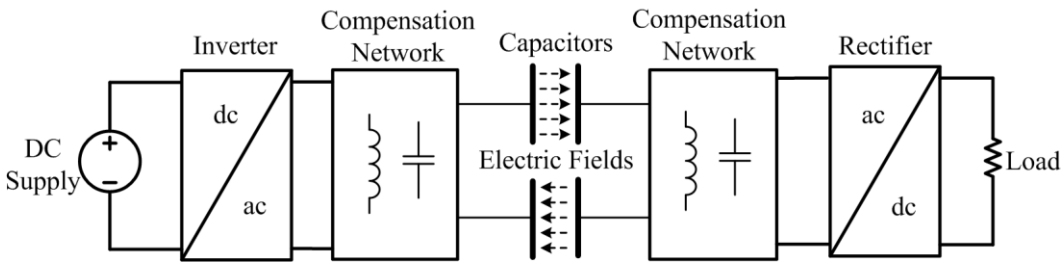

Fig. 1-6. Structure of a capacitive power transfer system

The advantage of the capacitive power transfer system with respect to IPT systems is its low cost and low eddy-current loss in nearby metals. Compared to the inductive coupler, the capacitive coupler can eliminate the usage of magnetic ferrite to reduce the system cost and weight. Also, the electric fields in a CPT system do not generate significant losses in nearby metal objects. CPT technology has been used in lots of applications, such as integrated circuits (IC) [69], biomedical devices [70], [71], synchronous machine excitation [72], and electric vehicles [73]. If the transfer distance is hundreds of mm, since the free space permittivity ε_0 is only 8.85×10^{-12} F/m and the relative permittivity of the dielectric material is usually less than 10, the coupling capacitance is small, which makes it challenging to transfer high level of power.

Table I-1. Comparison of WPT technologies [1]

technology	frequency	power	efficiency	distance	cost	size	applications
acoustic	kHz-MHz	medium	medium	long	high	small	biomedical, energy harvest underwater, metal wall[15-18]
optical	THz	low	low	long	high	small	biomedical, space, underwater[25-27]
microwave	GHz	high	low	long	high	large	cellular and sensor network, space[34-38]
inductive	kHz-MHz	high	high	medium	medium	medium	biomedical, IC, sensor network portable device, electric vehicle[50-54]
capacitive	kHz-MHz	medium	high	medium	low	medium	biomedical, IC, electric machine, electric vehicle[69-73]

A comparison of the five categories of WPT technologies is presented in Table I-1. It can be concluded that the IPT system is a good solution to realize wireless power transfer for electric

vehicle charging application. However, CPT technology has the potential of a more promising future to reduce the system cost and realize a more successful commercial product. In this dissertation, the high-power and long-distance CPT technology will be studied for electric vehicle charging applications, which can achieve several kW power transfer across hundreds of mm with over 90% dc-dc efficiency.

1.2. Development of Electric Vehicle Charging Technology

The electric vehicle is a clean and environmentally friendly alternative to the conventional combustion vehicle. It usually carries large amount of Lithium-Ion batteries, instead of fossil fuel, on board to store electric energy for vehicle propulsion [74]. Batteries are expensive, heavy, and their energy density is much lower than fossil fuel. Also, it usually takes a relatively long time to fully charge the batteries. Therefore, charging technology is important to the success of electric vehicles, and it is important to study and develop more effective, efficient, and convenient methods of charging.

Current vehicle-charging technology can be classified as conductive and inductive charging [75]. For conductive charging, there is direct metal-to-metal connection between the charger and the vehicle. Inductive charging utilizes the IPT technology mentioned above, in which resonant circuit is used to transfer power to vehicles through magnetic fields [76].

1.2.1. Conductive Charging

Conductive charging is also called plug-in charging, in which the electric vehicle is connected to the power source through electric cables [77]. The system power level varies from several kW to hundreds of kW according to the power requirements of different vehicles, such as passenger cars, heavy duty pick-up truck and buses. Conductive chargers can be classified as on-board and off-board chargers depending on the installation position of the power electronics converters, as shown in Figs. 1-7(a) and (b), respectively. According to the SAE-J1772 standard [78], the on-board charger is mostly for level 1 (≤1.92kW) and level 2 (≤19.2 kW) systems, and the off-board charger is for level 3 (≤240kW) systems.

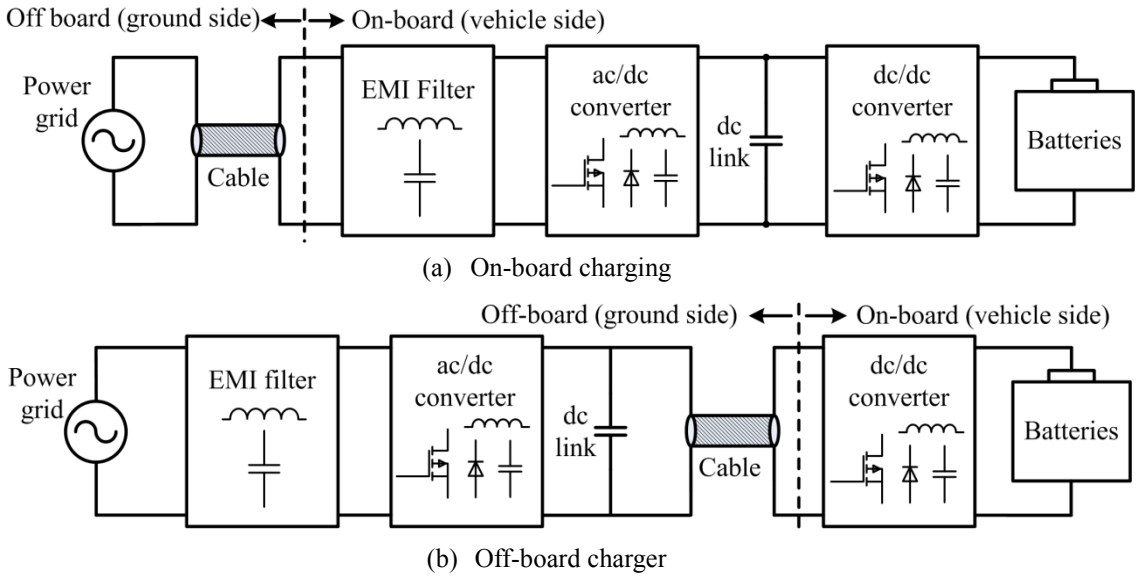

Fig. 1-7. Structures of conductive charging systems for electric vehicles

Fig. 1-7(a) shows the structure of an on-board charger, in which the ac power grid is directly connected to the vehicle through cables [79]. In this system, the size and weight of the filter and power electronics converters are small enough to be installed on the vehicle side, which helps to reduce the cost of infrastructure on the ground side. Therefore, it can be widely used in home garages for overnight charging, or at the work place for daytime charging.

Fig. 1-7(b) shows the structure of an off-board charger, in which the dc supply voltage is connected to the vehicle through cables [80]. The power is usually at the hundreds of kW level, and it is typically used in fast-charging stations for the general public. The circuit topology is similar to that of the on-board charger, but it has to be installed on the ground side, considering its size, weight, and cost.

The most significant advantages of conductive charging are its high power density and efficiency [81]. For both on- and off-board chargers, the system structure consists of three stages, listed as EMI filter, ac/dc converter, and the dc/dc converter as shown in Fig. 1-7 [82]. The researches of conductive chargers focus on the two converters to reduce their size and increase their efficiency. Non-isolated single switching converters, such as boost and buck converters, are typically used to realize the front-end ac/dc converter [83]. The peak efficiency of the ac/dc converter can reach 98.9% [84], and the overall efficiency from the ac grid to battery can reach

97.6% [85]. To reduce shocking hazards, isolated dc/dc converters, such as phase-shift full bridge converters [86], [87], LCC [88], and LLC [89] resonant converters, are used to provide galvanic isolation between the vehicle and the power grid. Although there is an isolation transformer in the circuit, the system efficiency can be improved through optimizing the circuit parameters [90], and the dc-dc efficiency can reach 97.6% at full-load conditions [91], [92]. The converters can also realize bidirectional power flow [93], and the batteries installed on the vehicle can act as distributed generators to inject power back into the power grid and contribute to the control of power grid [94], [95].

1.2.2. Inductive Charging

Inductive charging of electric vehicles is a typical application area of the IPT technology mentioned above, in which a separable transformer is used to transfer power [96]. The primary side of the transformer is at the ground side as a transmitter, and the secondary side is at the vehicle side as a receiver. Power is transferred through magnetic fields and there is no ohmic contact between the charger and the vehicle. The structure of an inductive charging system for electric vehicles is shown in Fig. 1-8 [97], [98]. The transfer distance between the transmitter and receiver can be as large as hundreds of mm.

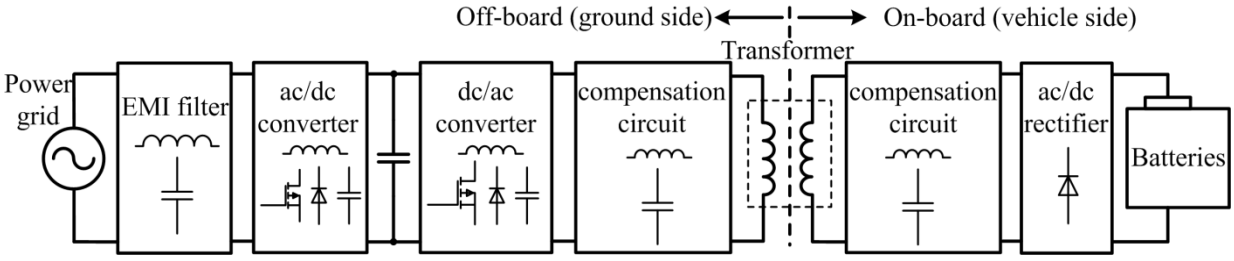

Fig. 1-8. Structures of an inductive charging system for electric vehicles

In the small-distance applications, the SAE-J1773 standard recommends physical, electrical, and performance requirements of the charging coupler [99], [100], in which the transformer is in the traditional EE or EI shape and the transmitter is connected with a long cable to allow it inserted into the receiver [101]. Therefore, the leakage inductance is limited, and there is a strong magnetic coupling in the transformer to transfer high levels of power [102]. Also, compensation

capacitors can be used to resonate with the transformer to further improve the system power and efficiency [103], [104]. This system structure was proposed in the 1990s and has been applied in commercial products. Compared to the conductive charging, the advantage of low-distance inductive charging is that it can provide insulation on the surface of the transmitter, and there is no concern of electric shock.

In large-distance applications, the SAE-J2954 standard provides the specification requirements for light-duty plug-in hybrid and electric vehicles [105]. Compared to conductive and small-distance inductive charging, the long cable is eliminated and the vehicle is automatically charged when it is parked near a charging pad [106]. Since the air-gap distance is in the range of hundreds of mm, the magnetic coupling coefficient is relatively small, which results in a loosely-coupled inductive charging system. Compensation circuits are required at both the primary and secondary sides to increase the system power [107], [108]. Large-distance inductive charging systems can be classified by the compensation circuit topologies.

A. Capacitor Compensation

In a loosely-coupled IPT system, compensation capacitors are required at both the primary and secondary sides. According to the position of the compensation capacitors, there are four different topologies, listed as series-series (SS) [109], series-parallel (SP) [110], parallel-series (PS) [111], and parallel-parallel (PP) [112] compensations, which are shown in Figs. 1-9(a), (b), (c), and (d), respectively.

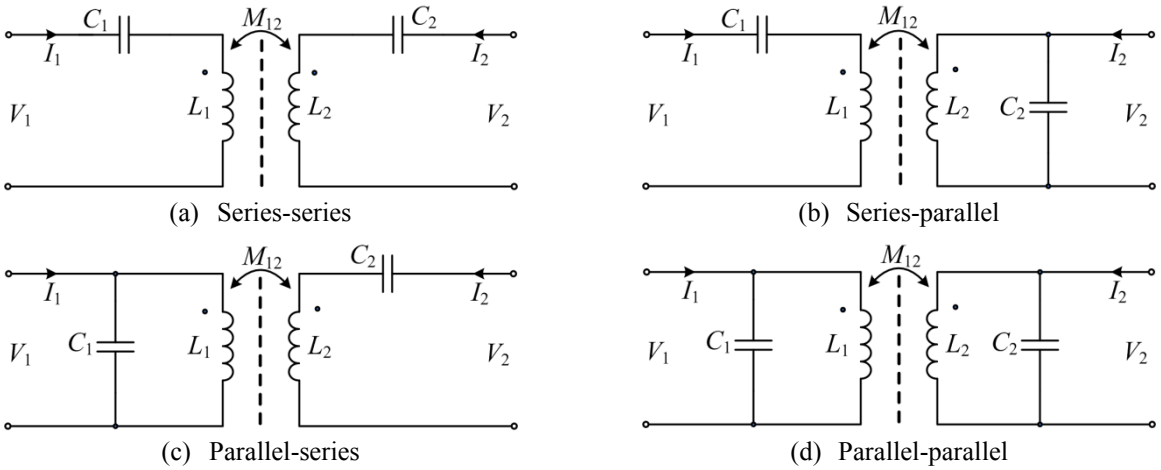

(a) Series-series (b) Series-parallel

(c) Parallel-series (d) Parallel-parallel

Fig. 1-9. Circuit topologies of capacitor compensation

The capacitors are designed to compensate the self or leakage inductances of the transformer, which results in a constant-current or constant-voltage working mode [113]. In electric vehicle charging applications, the constant-current mode is preferred, because the batteries behave as a constant voltage load at the output side. The advantage of capacitor compensation is simplicity. The SS compensation circuit has been well studied and applied in vehicle charging applications [114]. However, the system power is inversely proportional to the magnetic coupling coefficient. When there is misalignment between the transmitter and receiver, the input current significantly increases, and may exceed the component ratings.

B. Inductor-Capacitor Compensation

To overcome the limitation of capacitor compensation circuits, more complex circuits, including inductors and capacitors, have been proposed, such as the LCC [115] and CLC [116] compensations as shown in Fig. 1-10 (a) and (b), respectively.

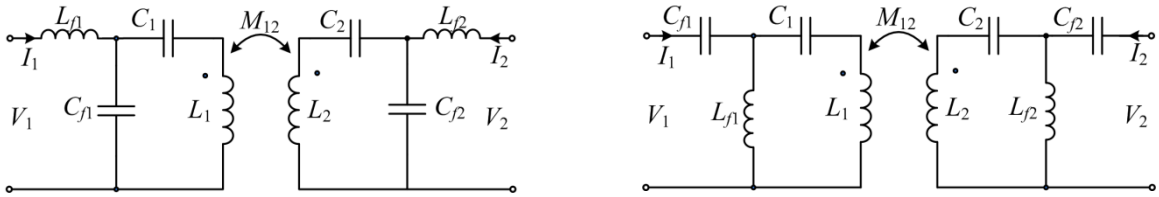

(a) Double-sided LCC (b) Double-sided CLC

Fig. 1-10. Circuit topologies of inductor-capacitor compensations

There are multiple resonances in these compensation circuits, and the components should be designed so that they all resonate at the same frequency to maximize the transferred power. In the double-sided LCC compensation circuit the output power is proportional to the magnetic coupling coefficient, and the transmitted current decreases as the receiver moves away from it [117]. Therefore, it can be used in a dynamic charging system and realize power transfer to moving vehicles [118]. Although there are more components in the circuits, the system dc-dc efficiency can still reach 96% with optimized circuit parameters, and the voltage and current stresses on the components can be reduced. In practical applications, the inter-operation between the compensation circuits in Fig. 9 and 10 is unavoidable, and their combinations can result in asymmetric topologies such as LCL-T [119] and LCL-S [120] compensations

1.3. Motivation of Capacitive Power Transfer

Although IPT technology has been widely exploited in vehicle charging applications, there are two significant limitations in practical systems. First, the IPT system is sensitive to nearby metal objects. The high-frequency magnetic field can generate significant eddy current losses in these objects, which can reduce the transferred power and the system efficiency [121]. Also, the losses can cause high temperatures and hence create a potential fire hazard. Second, the weight and cost of the IPT system are still too high for commercialization. In an IPT system, expensive Litz wire is required to make the coils to reduce conduction losses induced by the skin-effect [122]. Also, ferrite and aluminum shielding plates are necessary to improve the magnetic coupling and reduce the leakage magnetic fields, respectively [123]. However, these significantly increase the system weight and cost, and create installation difficulties.

Compared to the IPT system, CPT technology can solve the two limitations mentioned above. In a CPT system, electric fields are used to transfer power. These can experience metal objects without generating significant losses or significantly reducing power levels [124]. Usually, metal plates are used to generate electric fields, and there is no requirement on the plate thickness and shape. Therefore, it is more flexible to design the capacitive coupler depending on different applications. Also, aluminum plates can be used to further reduce the system weight and cost as compared to copper Litz wire coils.

Current CPT systems can be classified according to their circuit topologies, such as: PWM-converter-based CPT system, power-amplifier-based CPT system, and full-bridge inverter based CPT system, which will be introduced in the sequel. The CPT system structure shown in Fig. 1-6 is an example of the full-bridge CPT system.

1.3.1. PWM-Converter-Based CPT System

Power converters with a single active switch, such as buck-boost, Cuk, Sepic, Zeta, and push-pull converters [125], can be used to realize a CPT system. For example, the circuit topology of a CPT system based on a Sepic converter is shown in Fig. 1-11 [126].

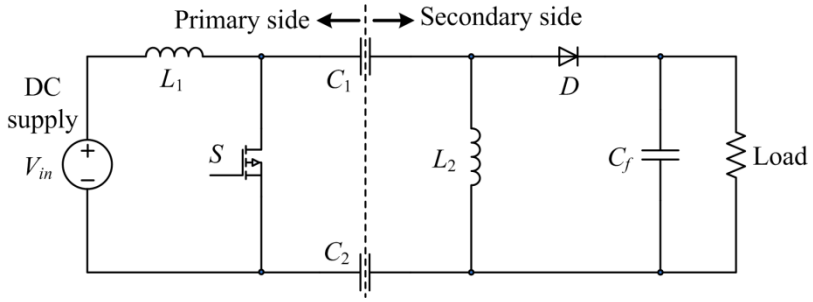

Fig. 1-11. CPT system based on a Sepic converter

Different from a conventional Sepic converter, there are two coupling capacitors C_1 and C_2 in the circuit, providing the isolation between the primary and secondary side and working as energy storage components. When the switch S turns off, the capacitors are charged by the input source. When the switch S turns on, the capacitors are discharged, and the power is transferred to the load. The coupling capacitance and switching frequency should be large enough to realize significant power transfer. For example, when the coupling capacitance increases to 24nF and the switching frequency is 200 kHz, the Sepic converter realizes more than 1 kW power transfer with 90.3% dc-dc efficiency [126].

The advantage of the PWM-converter-based CPT system is that system performance is not sensitive to circuit parameter variations. In real applications, the physical size and plate distance of the capacitive coupler can change the coupling capacitance. Also, it is common to have ±10% variations on the circuit component values [127]. In the PWM converter, as long as the parameters are large enough to achieve a continuous-current working mode, their variations cannot affect the system power. However, the disadvantage is that soft-switching condition cannot be realized in all load conditions. In this case, system efficiency is significantly reduced and the conductive EMI increases. Moreover, since there is only one active switch in the circuit, the power level of a CPT system is limited by the performance of the switch.

1.3.2. Power Amplifier-Based CPT System

High frequency power amplifier circuit, such as class D or class E converter, can also be used to realize a CPT system, as shown in Fig. 1-12 [128]. Usually, there is series inductor

connected with the capacitors to form resonance, and the two coupling capacitors C_1 and C_2 are used to replace the conventional external resonant capacitors.

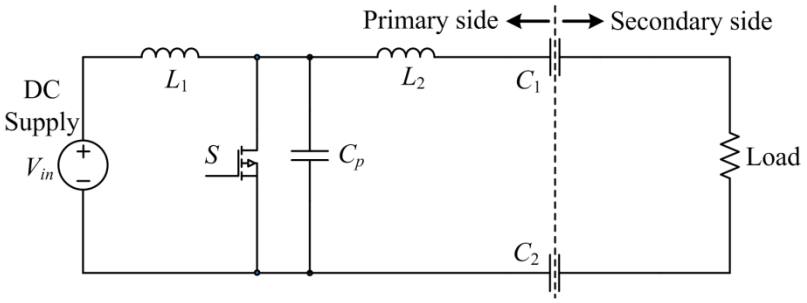

Fig. 1-12. CPT system based on a class E converter

The power amplifier can provide high-frequency switching capability to increase the system power, and the soft-switching condition can be satisfied through parameter design to improve the system efficiency. Also, the size of the passive components can be reduced due to high frequency. This circuit topology has been applied in the vehicle charging applications, in which a conformal bumper is installed in front of the vehicle to form capacitances with the charging pad [129]. When the switching frequency is 530 kHz, the system can achieve 1kW power transfer with a dc-dc efficiency of 92%.

However, the power amplifier is sensitive to parameter variations. When the coupling capacitances vary from the nominal values, the resonances in the circuit are disturbed and the system power and efficiency can be significantly reduced.

1.3.3. Full-Bridge Inverter based CPT System

The full-bridge inverter is an effective method to provide ac excitation to a CPT system, including the coupling capacitors and the compensation circuit, as shown in Fig. 1-13 [130]. The MOSFETs are driven by PWM signals, and it is convenient to adjust the switching frequency and duty ratio to regulate the system power. A diode rectifier is used at the secondary side to provide dc power to the load. Series inductors L_1 and L_2 are usually used to compensate the coupling capacitors C_1 and C_2 from both primary and secondary sides. The inductors can also provide EMI suppression function to the input [131].

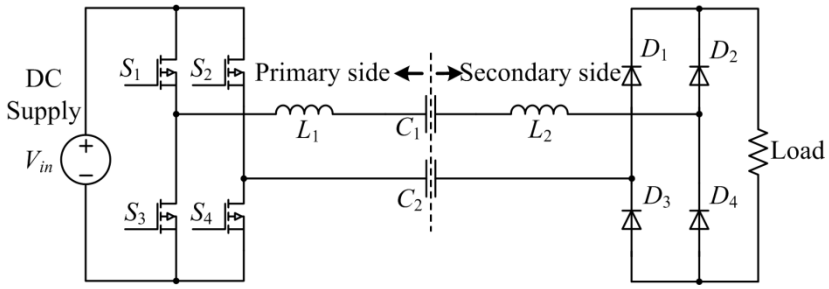

Fig. 1-13. CPT system based on a full-bridge inverter with series inductors

The advantage of series inductor compensation is its simplicity, and it can be applied in both low- and high-power applications. When it is used in biomedical devices to transfer power through human tissue, the frequency can reach hundreds of MHz [132]. It can also be applied in the excitation circuit for a synchronous motor, and the system efficiency can achieve over 90% [133], [134]. Compared to the single-switch PWM converter, the coupling capacitances can be relatively smaller and the switching frequency can be higher. In some applications, the required compensation inductor size is too large to be realized, so an active negative capacitor is proposed to replace the inductor [135], [136]. Since there are extra switches in the circuit, the system efficiency is reduced. Series compensation can also be used in electric vehicle charging applications, where the tires are used as the dielectric material to increase the coupling capacitances [137], [138]. However, it still requires the switching frequency to be in the MHz range to provide high power.

1.4. Challenges in Capacitive Power Transfer

1.4.1. Transfer Distance, Power, and Efficiency

The fundamental challenge in CPT technology comes from the tradeoffs between the transfer distance, power, and efficiency. The current CPT systems cannot achieve long distance, high power, and high efficiency simultaneously. Their performances are still not comparable with the IPT systems, so their application area has been limited. Most of the previous work focuses on small-distance and low-power applications, such as USB interface [139], LED driving [140] and robot charging [141]. When the transfer distance reaches hundreds of mm, the coupling

capacitance is small. This makes it difficult to realize high power transfer efficiently, especially for electric vehicle charging applications.

In the PWM-converter-based CPT system, the transfer distance is usually within 1 mm, which induces a relative larger capacitance. If the transfer distance is increased, the coupling capacitance decreases and the switching frequency have to be increased to transfer sufficient power. The system efficiency will therefore drop quickly due to switching losses since the soft-switching condition cannot be satisfied.

In the high-frequency power-amplifier based CPT system, the switching frequency can increase to tens of MHz range without affecting the soft-switching condition. However, the conduction losses in the passive components, such as inductors and capacitors, increase with the frequency. Therefore, the overall efficiency is still limited [142].

In the full-bridge inverter based CPT system with series inductors, the transfer distance is also typically within 1 mm to realize large coupling capacitances [143]. When the transfer distance increases, it requires either a large switching frequency in tens of MHz range or a large resonant inductor in mH range. However, too high a switching frequency makes it difficult to realize soft-switching of the MOSFETs in the full-bridge inverter, and the system efficiency is not acceptable. Besides, too large resonant inductor takes too large volume and weight, and its conduction loss also reduces the system efficiency.

Therefore, it is necessary and meaningful to investigate compensation circuit topologies which realize a long-distance, high-power, and high-efficiency CPT system for electric vehicle charging applications. The full-bridge inverter based CPT system is preferred because it can provide high power capability. The compensation circuit should resonate with the coupling capacitors and can realize high power transfer even with limited capacitance values.

1.4.2. Dynamic CPT System

The second challenge of CPT technology is its application in the dynamic charging of electric vehicles; i.e. the vehicle is charged while driving on the road. Dynamic charging has been already proposed in the IPT system [144], and the CPT system should also have this ability.

The CPT system has advantages over the IPT system when it is applied in the dynamic charging scenario. The IPT system requires circulating currents in the coils to establish magnetic fields to transfer power, so there are extra conduction stand-by losses when the receiver moves away from the transmitter. The CPT system requires voltages on plates to generate electric fields for power transfer, so stand-by losses can be reduced, as the currents can be minimal.

In dynamic charging applications, the system should be powered continuously during the moving process and the received power ripple should be minimized to protect the on-board batteries. Also, the system needs to be robust to the misalignment between the transmitter and receiver. These are the challenges we will address.

1.4.3. Power Density and Electric Field Emission

The third challenge in the application of CPT technology is the tradeoff between the system power density and electric fields emissions. The higher is power density of the capacitive coupler, the larger the electric field emissions to the surrounding environment. In a high-power charging scenario of electric vehicles, the electric field emission is a critical concern.

In most applications, it is desired to transfer as much power as possible with a limited capacitive coupler size, which means high power density is necessary to save space. However, electric field emissions are important constraint to the system power density, which is similar to the magnetic field limitations in an IPT system [145]. For human safety consideration, IEEE C95.1 standard [146] requires that the general public exposure to high-frequency electric fields at 1 MHz should be lower than 614V/m. This determines the upper limit of the CPT system power density and its safety operating area.

In long-distance CPT systems, the electric field emissions are much more significant than in short-distance systems. The electric fields are not confined between the plates. This is because the fringing fields between the parallel plates significantly increase with voltages and distance [147]. As system power increases, both voltages on the plates and the fringing electric fields increase. Therefore, the electric field emissions to the surrounding environment should be considered when designing a CPT system to realize high power density.

1.5. Contributions of This Dissertation

This dissertation focuses on the design of high-power, long-distance, and high-efficiency CPT systems for electric vehicle charging applications. Compared to previous works, this dissertation has three breakthroughs: the CPT system power is increased from several tens of Watts to several kW; the CPT system transfer distance is increased from mm to hundreds of mm; the CPT system efficiency is increased from 30% to over 90%. In the process to realize such an advanced CPT system, this dissertation has proposed several innovative approaches. The detailed contributions lie in four parts.

First, a double-sided LCLC compensation circuit topology has been proposed, that has realized a high-power, long-distance, and high-efficiency CPT system [148]. The theoretical analysis of the circuit working principle is provided. A prototype is design and implemented to validate the proposed design, which has achieved 2.4 kW power transfer across and air-gap of 150mm with a dc-dc efficiency of 90.8%.

Second, an IPT and CPT combined system has been proposed and realized to increase the system power and efficiency [149]. Magnetic and electric fields are both used in a single system to transfer power. The design method of the combined system is provided, in which the inductive and capacitive coupler resonate with each other. The power ratio between the IPT and CPT components is also studied. Since the IPT system has been widely studied and exploited in vehicle charging applications, its combination with CPT systems can help to promote the application of CPT technology. Also, a prototype is design and implemented to validate the combined idea, which has achieved simultaneous inductive and capacitive power transfer of 2.8kW across an air-gap of 150 mm, with a dc-dc efficiency of 94.4%.

Third, a dynamic CPT system has been proposed and realized to charge the electric vehicle while moving [150]. The transmitter is designed to be a long-track that can charge multiple receivers at different positions. A low-power prototype is designed and constructed to demonstrate this idea, which has achieve 154W power transfer across an air-gap of 50 mm with a dc-dc efficiency of 85.4%. When the receiver is moving along the transmitter track, it can be

continuously charged with a power pulsation within ±4.0% of the nominal power.

Fourth, safety issues and foreign object impact in a CPT system has been studied. Theoretical analysis shows that there are high voltages on the power transfer plates, which is the main reason that causes safety concerns. For safe operation, reliable insulation should be added on the plate surface. A six-plate coupler structure is proposed to reduce the electric field emission, and the safe range is 120 mm away from the coupler. Moreover, the influences on metallic and dielectric foreign objects are analyzed, which shows that a protection mechanism in the CPT system is required to protect the human body from touching.

1.6. References

[1] M.P. Kazmierkowski, A.J. Moradewicz, "Unplugged but Connected: Review of Contactless Energy Transfer System", *IEEE Ind. Electron. Mag.*, vol. 6, no.4, pp. 47-55, Dec. 2012.

[2] T. Sawant, D. Pilankar, R. Sule, S. Mahadehwar, "An Overview of Technological Advancements and Future Possibilities in Wireless Power Transmission," *Intern. J. Eng. and Tech.*, vol. 2, no. 8, pp. 260-267, Aug. 2013.

[3] S. Javadi, A. Mohamedi, "A General Review of Different Methods for Wireless Power Transmission," *Proc. Intern. Conf. on Wireless Networks* (*ICWN*), pp. 1-6, Jan. 2013.

[4] M.G.L. Roes, J.L. Duarte, M.A.M. Hendrix, E.A. Lomonova, "Acoustic Energy Transfer: A Review", *IEEE Trans. Ind. Electron.*, vol. 60, no. 1, pp. 242-248, Jan. 2013.

[5] Q. Liu, J. Wu, P. Xia, S. Zhao, Y. Yang, W. Chen, L. Hanzo, "Charging Unplugged: Will Distributed Laser Charging for Mobile Wireless Power Transfer Work?" *IEEE Veh. Techn. Mag.*, vol. 11, no. 4, pp. 36-45, Dec. 2016.

[6] K. Huang, X. Zhou, "Cutting the Last Wires for Mobile Communications by Microwave Power Transfer," *IEEE Comm. Mag.*, vol. 53, no. 6, pp. 86-93, Jun. 2015.

[7] G.A. Covic, J.T. Boys, "Inductive Power Transfer", *Proc. the IEEE*, vol. 101, no. 6, pp. 1376-1289, Jun. 2013.

[8] J. Dai, D.C. Ludois, "A Survey of Wireless Power Transfer and a Critical Comparison of Inductive and Capacitive Coupling for Small Gap Applications," *IEEE Trans. Power Electron.*, vol. 30, no. 11, pp. 6017-6029, Nov. 2015.

[9] T. Zaid, S. Saat, Y. Yusop, N. Jamal, "Contactless Energy Transfer Using Acoustic Approach – A Review," *Proc. IEEE Intern. Conf. Comp., Comm. Control Technology* (*I4CT*), pp. 376-381, Sept. 2014.

[10] T.C. Chang, M. J. Marcus, M.L. Wang, J. Charthad, B.T. Yakub, A. Arbabian, "Design of Tunable Ultrasonic Receiver for Efficient Powering of Implantable Medical Devices with Reconfigurable Power Loads," *IEEE Trans. on Ultrason. Ferroelectr. Freq. Contr.*, vol. 63, no. 10, pp. 1554-1562, Sept. 2016.

[11] D. Shmilovitz, S. Ozeri, C.C. Wang, B. Spivak, "Noninvasive Control of the Power Transferred to an Implanted Device by an Ultrasonic Transcutaneous Energy Transfer Link," *IEEE Trans. Biom. Eng.*, vol.

61, no. 4, p. 995-1004, Apr. 2014.

[12] S. Ozeri, D. Shmilovitz, S. Singer, C.C. Wang, "Ultrasonic Transcutaneous Energy Transfer using A Continuous Wave 650 kHz Gaussian Shaded Transmitter", *Ultrasonics*, vol 50, no. 7, pp. 666-674, Jun. 2010.

[13] H. Kim, S. Priya, H. Stephanou, K. Uchino, "Consideration of Impedance Matching Techniques for Efficient Piezoelectric Energy Harvesting," *IEEE Trans. on Ultrason. Ferroelectr. Freq. Contr.*, vol. 54, no. 9, pp. 1851-1859, Sept. 2007.

[14] C. Luo, H.F. Hofmann, "Wideband Energy Harvesting for Piezoelectric Devices with Linear Resonant Behavior", *IEEE Trans. Ultrason. Ferroelectr. Freq. Contr.*, vol 58, no 7, pp. 1294-1301, July. 2011.

[15] H. Vihvelin, J.R. Leadbetter, M. Bance, J.A. Brown, R.B. Adamson, "Compensating for Tissue Changes in an Ultrasonic Power Link for Implanted Medical Devices," *IEEE Trans. on Biom. Cir. and Syst.*, vol. 10, no. 2, pp. 404-411, Apr. 2016.

[16] A.L. Stein, H. Hofmann, "Autonomous Wideband Piezoelectric Energy Harvesting Utilizing a Resonant Inverter," *IEEE Trans. Power Electron.*, 2016, doi: 10.1109/TPEL.2016.2616301.

[17] Z. Zhou, Z. Peng, J.H. Cui, Z. Shi, "Efficient Multipath Communication for Time-Critical Applications in Underwater Acoustic Sensor Networks," *IEEE/ACM Trans. on Netw.*, vol. 19, no. 1, pp. 28-41, Feb. 2011.

[18] X. Zhu, Bin, Lin, L. Liu, Y. Luan, "Power Transfer Performance and Cutting Force Effects of Contactless Energy Transfer System for Rotary Ultrasonic Grinding," *IEEE Trans. Ind. Electron.*, vol. 63, no. 5, pp. 2785-2795, May. 2016.

[19] X. Bao, W. Biederman, S. Sherrit, M. Badescu, Y. Bar-Cohen, et al, "High-Power Piezoelectric Acoustic-electric Power Feedthru for Metal Walls", *Proc. SPIE*, vol. 6930, pp. 1-8, 2008.

[20] S. Sherrit, X. Bao, M. Badescu, J. Aldrich, Y. Bar-Cohen, et al, "1 kW Power Transmission using Wireless Acoustic-Electric Feed-through (WAEF)", *Proc. ASCE*, pp. 1-10, 2008.

[21] W. Zhou, k. Jin, "Efficiency Evaluation of Laser Diode in Different Driving Modes for Wireless Power Transmission," *IEEE Trans. Power Electron.*, vol. 30, no. 11, pp. 6237-6244, Nov. 2015.

[22] W. Zhou, K. Jin, "Optimal Photovoltaic Array Configuration under Gaussian Laser Beam Condition for Wireless Power Transmission," *IEEE Trans. Power Electron.*,doi:10.1109/TPEL.2016.2583502.

[23] R.M. Dicklinson, "Wireless Power Transmission Technology State of the Art: The First Bill Brown Lecture", *Acta Astronaut*, vol. 53, no. 4-10, pp. 561-570, 2003.

[24] A. Sahai, D. Graham, "Optical Wireless Power Transmission at Long Wavelength", *Proc. IEEE Intern. Conf. on Space Optical System and Application* (*ICSOS*), pp. 164-170, May. 2011.

[25] D. Shi, L. Zhang, H. Ma, Z. Wang, Y. Wang, Z. Cui, "Research on Wireless Power Transmission System between Satellites," *Proc. IEEE Wireless Power Transfer Conf.* (*WPTC*), pp. 1-4, Jun. 2016.

[26] H. Kaushal, G. Kaddoum, "Underwater Optical Wireless Communication," *IEEE Access*, vol. 4, pp. 1518-1547, Apr. 2016.

[27] K. Goto, T. Nakagawa, O. Nakamura, S. Kawata, "An Implantable Power Supply with an Optically Rechargeable Lithium Battery", *IEEE Trans. on Biom. Eng.*, vol. 48, no. 7, pp. 830-833, July. 2001

[28] S. Jarvis, J. Mukherjee, M. Perren, S. Sweeney, "Development and Characterization of Laser Power Converters for Optical Power Transfer Applications," *IET Optoelectronics*, vol. 8, no. 2, pp. 64-70, Apr. 2014.

[29] V. Rossin, E. Zucker, M. Peters, "High-Power High-Efficiency 910 to 980 nm Broad-area Laser Diodes",

Proc. SPIE, vol. 5336, pp. 196-202, 2003.

[30] K.J. Duncan, "Laser Based Power Transmission: Component Selection and Laser Hazard Analysis," *Proc. IEEE Workshop on Emerging Technologies: Wireless Power Transfer* (*WoW*), pp. 100-103, Oct. 2016.

[31] N. Shinohara, T. Ichihara, "Coexistence of Wireless Power Transfer via Microwaves and Wireless Communication for Battery-less Zigbee Sensors," *Proc. Intern. Symposium on Electromagnetic Compatibility* (*EMC*), pp. 445-448, May. 2014.

[32] N. Shinohara, "Power without Wires," *IEEE Microwave Magazine*, vol. 12, no. 7, pp. 64-73, Dec. 2011.

[33] Y. Huang, N. Shinohara, T. Mitani, "Impedance Matching in Wireless Power Transfer," *IEEE Trans. on Microwave Theory and Techniques*, 2016, doi: 10.1109/TMTT.2016.2618921.

[34] K. Huang, V. Lau, "Enabling Wireless Power Transfer in Cellular Networks: Architecture, Modeling and Deployment," *IEEE Trans. on Wireless Communications*, vol. 13, no. 2, pp. 902-912, Feb. 2014.

[35] S. Bi, C. Ho, R. Zhang, "Wireless Powered Communication: Opportunities and Challenges," *IEEE Comm. Mag.*, pp. 117-125, Apr. 2015.

[36] Z. Popvic, "Cut the Cord," *IEEE Microwave Magazine*, vol. 14, no. 2, pp. 55-62, Apr. 2013.

[37] J.O. McSpadden, J.C. Mankins, "Space Solar Power Programs and Microwave Wireless Power Transmission Technology", *IEEE Micr. Mag.*, vol. 3, no. 4, pp. 46-57, Dec. 2002.

[38] W.C. Brown, "The History of Power Transmission by Radio Waves", *IEEE Trans. Micr. Th. Tech.*, vol. MTT-32, no. 9, pp. 1230-1242, Sept. 1984.

[39] Y. Homma, T. Sasaki, K. Namura, F. Sameshima, "New Phased Array and Rectenna Array System for Microwave Power Transmission Research", *Proc.* IMWS-IWPT, pp. 59-62, Jun. 2011.

[40] H. Tonormura, J. Miyakoshi, N. Shinohara, "Research of Microwave Safety Issue of Wireless Power Transfer Technology for Commercial Vehicles," *Proc. European Conf. on Antennas and Propagation* (*EuCAP*), pp. 1-4, Apr. 2015.

[41] Q. Liu, K. Yildirim, P. Pawelczak, M. Warnier, "Safe and Secure Wireless Power Transfer Network: Challenges and Opportunities in RF-based Systems," *IEEE Comm. Mag.*, pp. 74-79, Sept. 2016.

[42] H. Toromura, Y. Huang, S. Koyama, J. Miyakoshi, N. Shinohara, "Biological Effects of High-Power Microwave Power Transfer System for Electric Vehicle," *Proc. IEEE Wireless Power Transfer Conf.* (*WPTC*), pp. 1-3, May. 2016.

[43] A. Kurs, A. Karalis, R. Moffatt, J.D. Joannopoulos, P. Fisher, M. Soljacic, "Wireless Power Transfer via Strongly Coupled Magnetic Resonances," *Science*, vol. 317, no. 83, pp. 83-86, July. 2007.

[44] S.Y. Ron Hui, "Magnetic Resonance for Wireless Power Transfer," *IEEE Power Electron. Mag.*, vol. 3, no. 1, pp. 14-30, Mar. 2016.

[45] S.Y. Hui, W. Zhong, C.K. Lee, "A Critical Review of Recent Progress in Mid-range Wireless Power Transfer," *IEEE Trans. Power Electron.*, vol. 29, no. 9, pp. 4500-4511, Sept. 2014.

[46] R. Trevisan, A. Costanzo, "State-of-the-art of Contactless Energy Transfer (CET) Systems: Design Rules and Applications," *Wireless Power Transfer*, vol. 1, no. 1, pp. 10-20, Mar. 2014.

[47] C. Chen, T. Chu, C. Lin, Z. Jou, "A Study of Loosely Coupled Coils for Wireless Power Transfer," *IEEE Trans. on Circuits and Systems-II: Express Briefs*, vol. 57, no. 7, pp. 536-540, Jul. 2010.

[48] W. Zhang, C. Mi, "Compensation Topology of High-Power Wireless Power Transfer System," *IEEE Trans. Veh. Techn.*, vol. 65, no. 6, pp. 4768-4778, Jun. 2016.

[49] J. Zhang, X. Yuan, C. Wang, Y. He, "Comparative Analysis of Two-Coil and Three-Coil Structures for

Wireless Power Transfer," *IEEE Trans. Power Electron.*, vol. 32, no.1, pp. 341-352, Jan. 2017.

[50] N. Kuo, B. Zhao, A. Niknejad, "Inductive Wireless Power Transfer and Uplink Design for a CMOS Tag with 0.01mm^2 Coil Size," *IEEE Micr. Wireless Comp. Letters*, vol. 26, no. 10, pp. 852-854, Oct. 2016.

[51] S. Stoecklin, A. Yousaf, T. Volk, L. Reindl, "Efficient Wireless Powering of Biomedical Sensor Systems for Multichannel Brain Implants," *IEEE Trans. on Instrum. Meas.*, vol. 65, no. 4, pp. 754-764, Apr. 2016.

[52] L. Xie, Y. Shi, Y.T. Hou, W. Lou, "Wireless Power Transfer and Applications to Sensor Network," *IEEE Wireless Comm.*, vol. 20, no. 4, pp. 140-145, 2013.

[53] S.Y. Hui, "Planar Wireless Charging Technology for Portable Electronic Products and Qi," *Proc. the IEEE*, vol. 101, no. 6, pp. 1290-1301, Jun. 2013.

[54] M. Kim, H. Kim, D. Kim, Y. Jeong, H. Park, S. Ahn, "A Three-Phase Wireless-Power-Transfer System for Online Electric Vehicles with Reduction of Leakage Magnetic Fields," *IEEE Trans. Micr. Th. Tech.*, vol. 63, no. 11, pp. 3806-3813, Nov. 2015.

[55] M. Zargham, P. Gulak, "Maximum Achievable Efficiency in Near-Field Coupled Power-Transfer Systems," *IEEE Trans. on Biom. Cir. and Sys.*, vol. 6, no. 3, pp. 228-245, Jun. 2012.

[56] T. Imura, Y. Hori, "Maximizing Air Gap and Efficiency of Magnetic Resonant Coupling for Wireless Power Transfer Using Equivalent Circuit and Neumann Formula," *IEEE Trans. Ind. Electron.*, vol. 58, no. 10, pp. 4746-4752, Oct. 2011.

[57] X. Liu, G. Wang, "A Novel Wireless Power Transfer System with Double Intermediate Resonant Coils," *IEEE Trans. Ind. Electron.*, vol. 63, no. 4, pp. 2174-2180, Apr. 2016.

[58] D. Lin, C. Zhang, S.Y. Ron Hui, "Mathematic Analysis of Omnidirectional Wireless Power Transfer – Part-II Three-Dimensional Systems," *IEEE Trans. Power Electron.*, vol. 32, no. 1, pp. 613-624, Jan. 2017.

[59] Y. Sun, P. Yan, Z. Wang, Y. Luan, "The Parallel Transmission of Power and Data with the Shared Channel for an Inductive Power Transfer System," *IEEE Trans. Power Electron.*, vol. 31, no. 8, pp. 5495-5502, Aug. 2016.

[60] C. Huang, C. Lin, Y. Wu, "Simultaneous Wireless Power/Data Transfer for Electric Vehicle Charging," *IEEE Trans. Ind. Electron.*, vol. 64, no. 1, pp. 682-690, Jan. 2017.

[61] S. Freitas, F. Domingos, R. Mirzavand, A. Maunder, P. Naseri, P. Mousavi, "A Novel Method for Data and Power Transmission through Metallic Structures," *IEEE Trans. Ind. Electron.*, 2016, doi: 10.1109/TIE.2016.2644602.

[62] S. Mirbozorgi, H. Bahrami, M. Sawan, B. Gosselin, "A Smart Cage with Uniform Wireless Power Distribution in 3D for Enabling Long-Term Experiments with Freely Moving Animals," *IEEE Trans. on Biom. Cir. and Sys.*, vol. 10, no. 2, pp. 424-434, Apr. 2016.

[63] C. Xiao, K. Wei, D. Cheng, Y. Liu, "Wireless Charging System Considering Eddy Current in Cardiac Pacemaker Shell: Theoretical Modeling, Experiments and Safety Simulations," *IEEE Trans. Ind. Electron.*, 2016, doi: 10.1109/TIE.2016.2645142.

[64] S. Li, Z. Liu, H. Zhao, Li. Zhu, Z. Chen, "Wireless Power Transfer by Electric Field Resonance and Its Application in Dynamic Charging," *IEEE Trans. Ind. Electron.*, vol. 63, no. 10, pp. 6602- 6612, Oct. 2016.

[65] L. Huang, A.P. Hu, A. Swain, X. Dai, "Comparison of Two High Frequency Converters for Capacitive Power Transfer," *Proc. IEEE Energy Conv. Cong. Expo.* (*ECCE*), pp. 5437-5443, Sept. 2014.

[66] M. Kline, I. Izyumin, B. Boser, S. Sanders, "Capacitive Power Transfer for Contactless Charging," *Proc.*

IEEE Appl. Power Electron. Conf. Expo. (*APEC)*, pp. 1048-2334, Mar. 2011.

[67] A. Amanci, H. Ruda, F. Dawson, "Galvanic Isolation for High-Frequency Applications Using an Integrated Dielectric Structure," *IEEE Trans. Power Electron.*, vol. 31, no. 8, pp. 5797-5804, Aug. 2016.

[68] C. Y. Xia, C. W. Li, J. Zhang, "Analysis of Power Transfer Characteristic of Capacitive Power Transfer System and Inductively Coupled Power Transfer System", *Proc. IEEE Intern. Conf. on Mechatronic Science, Electric Engineering and Computer Science*, pp. 1281-1285, Aug. 2011.

[69] E. Culurciello, A.G. Andreou, "Capacitive Inter-Chip Data and Power Transfer for 3-D VLSI", *IEEE Trans. Circuits and System – II. Express Briefs*, vol 53, no 12, pp. 1348-1352, Dec. 2006.

[70] K. Piipponen, R. Sepponen, P. Eskelinen, "A Biosignal Instrumentation System Using Capacitive Coupling for Power and Signal Isolation," *IEEE Trans. on Biom. Eng.*, vol. 54, no. 10, pp. 1822-1828, Oct. 2007.

[71] R. Jegadeesan, K. Agarwal, Y Guo, S. Yen, N. Thakor, "Wireless Power Delivery to Flexible Subcutaneous Implants Using Capacitive Coupling," *IEEE Trans. on Microwave Theory and Techniques*, 2016, doi: 10.1109/TMTT. 2016.2615623.

[72] D.C. Ludois, J.K. Reed, K. Hanson, "Capacitive Power Transfer for Rotor Field Current in Synchronous Machines," *IEEE Trans. Power Electron.*, vol. 27, no. 11, pp. 4638-4645, Nov. 2012.

[73] C. Mi, "High Power Capacitive Power Transfer for Electric Vehicle Charging Applications," *Proceeding of Intern. Conf. on Power Electron. Sys. Appl.* (*PESA*), pp. 1-4, Dec. 2015.

[74] A. Khaligh, Z. Li, "Battery, Ultracapacitor, Fuel Cell, and Hybrid Energy Storage System for Electric, Hybrid Electric, Fuel Cell, and Plug-in Hybrid Electric Vehicles: State of the Art," *IEEE Trans. Veh. Techn.*, vol. 59, no. 6, pp. 2806-2814, July. 2010.

[75] A. Khaligh, S. Dusmez, "Comprehensive Topological Analysis of Conductive and Inductive Charging Solutions for Plug-in Electric Vehicles," *IEEE Trans. Veh. Techn.*, vol. 61, no. 8, pp. 3475-3489, Oct. 2012.

[76] B. Peschiera, S.S. Williamson, "Review of Inductive Power Transfer Technology for Electric and Plug-in Hybrid Electric Vehicles," *Proceeding of IEEE Ind. Electron. Conf.* (IECON), pp. 4672-4677, Nov. 2013.

[77] M. Yilmaz, P.T. Krein, "Review of Battery Charger Topologies, Charging Power Levels, and Infrastructure for Plug-In Electric and Hybrid Vehicles," *IEEE Trans. Power Electron.*, vol. 28, no.5, pp. 2151-2169, 2013.

[78] *SAE Electric Vehicle and Plug-in Hybrid Electric Vehicle Conductive Charge Coupler*, SAE Standard J1772, Jan., 2010.

[79] H. Wang, A. Hasanzadeh, A. Khaligh, "Transportation Electrification: Conductive Charging of Electrified Vehicles," *IEEE Electrif. Mag.*, vol. 1, no. 2, pp. 46-58, Feb. 2014.

[80] M.E. Amoli, K. Choma, J. Stefani, "Rapid-charge Electric Vehicle Stations," *IEEE Trans. on Power Delivery*, vol. 25, no.3, pp. 1883-1887, 2010.

[81] D. Kim, M. Kim, B. Lee, "An Integrated Battery Charger with High Power Density and Efficiency for Electric Vehicles," *IEEE Trans. Power Electron.*, 2016, dio: 10.1109/TPEL.2016.2604404.

[82] H. Wang, S. Dusmez, A. Khaligh, "Design and Analysis of a Full Bridge LLC Based PEV Charger Optimized for Wide Battery Voltage Range," *IEEE Trans. on Veh. Techn.*, vol. 63, no. 4, pp. 1603-1613, May. 2014.

[83] F. Musavi, W. Eberle, W.G. Dunford, "A High Performance Single-Phase Bridgeless Interleaved PFC

Converter for Plug-in Hybrid Electric Vehicle Battery Chargers," *IEEE Trans. on Ind. Appl.*, vol. 47, no. 4, pp. 1833-1843, Jul. 2011.

[84] F. Musavi, M. Edington, W. Eberle, W.G. Dunford, "Evaluation and Efficiency Comparison of Front End AC-DC Plug-in Hybrid Charger Topologies," *IEEE Trans. on Smart Grid*, vol. 3, no. 1, pp. 413-421, Mar. 2012.

[85] C.Y. Oh, D.H. Kim, D.G. Woo, W.Y. Sung, Y.S. Kim, B.K. Lee, "A High Efficient Non-isolated Single Stage On Board Battery Charger for Electric Vehicles," *IEEE Trans. Power Electron.*, vol. 28, no. 12, pp. 5746-5757, Dec. 2013.

[86] B. Gu, J.S. Lai, N. Kee, C. Zheng, "Hybrid-Switching Full-bridge DC-DC Converter with Minimal Voltage Stress of Bridge Rectifier, Reduced Circulating Losses, and Filter Requirement for Electric Vehicle Battery Chargers," *IEEE Trans. Power Electron.*, vol. 28, no.3, pp. 1132-1144, Mar. 2013

[87] D.S. Gautam, F. Musavi, M. Edington, W. Eberle, W.G. Dunford, "An Automotive On Board 3.3 kW Battery Charger for PHEV Application," *IEEE Trans. Veh. Techn.*, vol. 61, no.8, pp. 3466-3474, Oct. 2012.

[88] D. Fu, F.C. Lee, Y. Qiu, F. Wang, "A Novel High Power Desnsity Three Level LCC Resonant Converter with Constant Power Factor Control for Charging Applications," *IEEE Trans. Power Electron.*, vol. 23, no. 5, pp. 2411- 2420, Sept. 2008.

[89] C. Hua, Y. Fang, C. Lin, "LLC Resonant Converter for Electric Vehicle Battery Chargers," *IET Power Electronics*, vol. 9, no. 12, pp. 2369-2376, Oct. 2016.

[90] J. Deng, S. Li, S. Hu, C. Mi, R. Ma, "Design Methodology of LLC Resonant Converters for Electric Vehicle Battery Chargers," *IEEE Trans. Veh. Techn.*, vol. 63, no. 4, pp. 1581-1592, May. 2014.

[91] H. Wang, S. Dusmez, A. Khaligh, "Maximum Efficiency Point Tracking Technique for LLC based PEV Chargers Through Variable DC Link Control," *IEEE Trans. Ind. Electron.*, vol. 61, no. 11, pp. 6041-4049, Nov. 2014.

[92] Junjun Deng, Chris Mi, Siqi Li, R. Ma, "Design of LLC Resonant Converters Based on Operation Mode Analysis for Level Two PHEV Battery Chargers," *IEEE/ASME Trans. Mech.*, vol. 20, no. 4, pp. 1595-1606, Aug. 2015.

[93] Z. Zahid, Z. Dalala, R. Chen, B. Chen, J. Lai, "Design of Bidirectional DC-DC Resonant Converter for Vehicle-to-Grid (V2G) Applications," *IEEE Trans. Transp. Electrif.*, vol. 1, no. 3, pp. 232-244, Oct. 2015.

[94] S. Zou, Z. Ma, X. Liu, I. Hiskens, "An Efficient Game for Coordinating Electric Vehicle Charging," *IEEE Trans. on Automatic Control*, 2016, doi: 10.1109/TAC.2016.2614106.

[95] P. Kydd, C. Martin, K. Jomara, P. Delgoshari, A. Riley, "Vehicle-Solar-Grid Integration II: Results in Simulated School Bus Operation," *IEEE Power Energy Techn. Sys. J.*, vol. 3, no. 4, pp. 198-206, 2016.

[96] F. Musavi, W. Eberle, "Overview of Wireless Power Transfer Technologies for Electric Vehicle Battery Charging," *IET Power Electronics*, vol. 7, no. 1, pp. 60-66, Jan. 2014.

[97] S. Samanta, A.K. Rathore, "A New Current-Fed CLC Transmitter and LC Receiver Topology for Inductive Power Transfer Application: Analysis, Design, and Experimental Results," *IEEE Trans. Transp.Electrif.*, vol. 1, no. 4, pp. 357-368, Dec. 2015.

[98] R. Bosshard, J.W. Kolar, "Inductive Power Transfer for Electric Vehicle Charging," *IEEE Power Electron. Mag.*, pp. 22-30, Sept. 2016.

[99] *SAE Electric Vehicle and Plug-in Hybrid Electric Vehicle Inductively Coupled Charging*, SAE Standard

J1773, Jun., 2014.

[100] H.H. Kutkut, K.W. Klontz, "Design Considerations for Power Converters Supplying the SAE J-1773 Electric Vehicle Inductive Coupler," *IEEE Appl. Power Electron. Conf. Expo.* (*APEC*), pp. 841-847, Mar. 1997.

[101] K.W. Klontz, A. Esser, R.R. Bacon, "An Electric Vehicle Charging System with Universal Inductive Interface," *IEEE Power Conversion Conf.*, pp. 227-232, 1993.

[102] K.W. Klontz, A. Esser, P.J. Wolfs, D.M. Divan, "Converter Selection for Electric Vehicle Charger Systems with a High-Frequency High-Power Link," *IEEE Power Electronics Specialists Conf.*, pp. 855-861, 1993.

[103] H. Ayano, K. Yamamoto, N. Hino, I. Yamato, "Highly Efficient Contactless Electrical Energy Transmission System," *IEEE Industrial Electronics Conf.* (*IECON*), pp. 1364-1369, 2002.

[104] J.G. Hayes, M.G. Egan, J.M. Murphy, S.E. Schulz, J.T. Hall, "Wide Load Range Resonant Converter Supplying the SAE J-1773 Electric Vehicle Inductive Charging Interface," *IEEE Trans. on Ind. Appl.*, vol. 35, no. 4, pp. 884-895, 1999.

[105] *SAE Wireless Power Transfer for Light-Duty Plug-In and Electric Vehicles and Alignment Methodology*, SAE Standard J2954, May, 2016.

[106] H. Sakamoto, K. Harada, S. Washimia, K. Takehara, "Large Air-Gap Coupler for Inductive Charger," *IEEE Trans. on Magnetics*, vol. 35, no.5, pp. 3526-3528, 1999.

[107] J. Kim, D. Kim, Y. Park, "Analysis of Capacitive Impedance Matching Networks for Simultaneous Wireless Power Transfer to Multiple Devices," *IEEE Trans. Ind. Electron.*, vol. 62, no. 5, pp. 2807-2813, May 2015.

[108] N. Inagaki, "Theory of Image Impedance Matching for Inductively Coupled Power Transfer Systems," *IEEE Trans. on Microwave Theory and Techniques*, vol. 62, no. 4, pp. 901-908, Apr. 2014.

[109] J. Hou, Q. Chen, S. Wong, C.K. Tse, X. Ruan, "Analysis and Control of Series/Series-Parallel Compensated Resonant Converter for Contactless Power Transfer," *IEEE J. of Emerg. and Selec. Top. Power Electron.*, vol. 3, no. 1, 124-136, Mar. 2015.

[110] Y. Sohn, B. Choi, E. Lee, G. Lim, G. Cho, C.T. Rim, "General Unified Analysis of Two-Capacitor Inductive Power Transfer Systems: Equivalence of Current-Source SS and SP Compensation," *IEEE Trans. Power Electron.*, vol. 30, no. 11, pp. 6030-6045, Nov. 2015.

[111] W. Zhang, S. Wong, C.K. Tse, Q. Chen, "Load Independent Duality of Current and Voltage Output of a Series- or Parallel Compensated Inductive Power Transfer Converter with Optimized Efficiency," *IEEE J. of Emerg. and Selec. Top. Power Electron.*, vol. 3, no. 1, 137-146, Mar. 2015.

[112] B. Wang, A.P. Hu, D. Budgett, "Maintaining Middle Zero Voltage Switching Operation of Parallel-Parallel Tuned Wireless Power Transfer," *IET Power Electron.*, vol. 7, no. 1, pp. 78-84, 2014.

[113] X. Qu, H. Han, S. Wong, C.K. Tse, W. Chen, "Hybrid IPT Topologies with Constant Current or Constant Voltage Output for Battery Charging Applications," *IEEE Trans. Power Electron.*, vol. 30, no. 11, pp. 6329-6337, Nov. 2015.

[114] C. Mi, G. Buja, S. Choi, C.T. Rim, "Modern Advances in Wireless Power Transfer Systems for Roadway Powered Electric Vehicles," *IEEE Trans. Ind. Electron.*, vol. 63, no. 10, pp. 6533-6545, Oct. 2016.

[115] S. Li, W. Li, J. Deng, T.D. Nguyen, C.C. Mi, "A Double Sided LCC Compensation Network and Its Tuning Method for Wireless Power Transfer," *IEEE Trans. Veh. Techn.*, vol. 64, no. 6, pp. 2261-2273, Jun. 2015.

[116] A.K. Swain, M.J. Nearth, U.K. Madawala, D.J. Thrimawithana, "A Dynamic Multivariable State-space Model for Bidirectional Inductive Power Transfer Systems," *IEEE Trans. Power Electron.*, vol. 27, no. 11, pp. 4772-4780, Nov, 2012.

[117] W. Li, H. Zhao, J. Deng, S. Li, C. Mi, "Comparison Study on SS and Double-Sided LCC Compensation Topologies for EV/PHEV Wireless Chargers," *IEEE Trans. Veh. Techn.*, vol. 65, no. 6, pp. 4429-4439, Jun. 2016.

[118] S. Zhou, C. Mi, "Multi-Paralleled LCC Reactive Power Compensation Networks and Their Tuning Method for Electric Vehicle Dynamic Wireless Charging," *IEEE Trans. Ind. Electron.*, vol. 63, no. 10, pp. 6546-6556, Oct. 2016.

[119] M. Borage, S. Tiwari, S. Kotaiah, "Analysis and Design of an LCL-T Resonant Converter as a Constant-Current Power Supply," *IEEE Trans. Ind. Electron.*, vol. 52, no. 6, pp. 1547-1554, Dec. 2005.

[120] J.L. Villa, J. Sallan, J.F. Osorio, A. Llombart, "High Misalignment Tolerant Compensation Topology for ICPT Systems," *IEEE Trans. Ind. Electron.*, vol. 59, no. 2, pp. 945-951, Feb. 2012.

[121] Z. Cheng, Y. Lei, K. Song, C. Zhu, "Design and Loss Analysis of Loosely Coupled Transformer for an Underwater High-Power Inductive Power Transfer System," *IEEE Trans.* on Mag., vol. 51, no. 7, 2015.

[122] S. Wang, D. Dorrell, "Copper Loss Analysis of EV Charging Coupler," *IEEE Trans. on Magnetics*, vol. 51, no. 11, Nov. 2015.

[123] J. Kim, J. Kim, S. Kong, H. Kim, I. Suh, "Coil Design and Shielding Methods for a Magnetic Resonant Wireless power Transfer," *Proc. the IEEE*, vol. 101, no. 6, pp. 1332-1342, Jun. 2013.

[124] C. Liu, A.P. Hu, N.C. Nair, "Coupling Study of a Rotary Capacitive Power Transfer System," *Proc. IEEE Intern. Conf. on Ind. Techn.* (*ICIT*), pp. 1-6, 2009.

[125] C. Liu, A.P. Hu, "Steady State Analysis of a Capacitively Coupled Contactless Power Transfer System," *Proc. IEEE Energy Conv. Cong. Expo.* (*ECCE*), pp. 3233-3238, Sept. 2009.

[126] J. Dai, D.C. Ludois, "Single Active Switch Power Electronics for KW Scale Capacitive Power Transfer," *IEEE J. of Emerg. and Selec. Top. Power Electron.*, vol. 3, no. 1, pp. 315-323, Mar. 2015.

[127] F. Lu, H. Hofmann, J. Deng, C. Mi, "Output Power and Efficiency Sensitivity to Circuit Parameter Variations in Double-Sided LCC-Compensated Wireless Power Transfer System," *Proc. IEEE Appl. Power Electron. Conf. Expo.* (*APEC*), pp. 597-601, Mar. 2015.

[128] L. Huang, A.P. Hu, A. Swain, X. Dai, "Comparison of Two High Frequency Converters for Capacitive Power Transfer," *Proc. IEEE Energy Conv. Cong. Expo.* (*ECCE*), pp. 5437-5443, Sept. 2014.

[129] J. Dai, D.C. Ludios, "Capacitive Power Transfer Through a Conformal Bumper for Electric Vehicle Charging," *IEEE J. of Emerg. and Selec. Top. Power Electron.*, vol. 4, no. 3, pp. 1015-1025, Sept. 2016.

[130] C. Liu, A.P. Hu, G.A. Covic, N.C. Nair, "Comparative Study of CCPT Systems with Two Different Inductor Tuning Positions," *IEEE Trans. Power Electron.*, vol. 27, no. 1, pp. 294-306, Jan. 2012.

[131] J. Zhu, M. Xu, J. Sun, C. Wang, "Novel Capacitor-isolated Power Converter," *Proc. IEEE Energy Conv. Cong. Expo.* (*ECCE*), pp. 1824-1829, Sept. 2010.

[132] R. Jegadeesan, Y.X. Guo, M. Je, "Electric Near-field Coupling for Wireless Power Transfer in Biomedical Applications," *Proc. IEEE Intern. Micr. Workshop RF and Wireless Techn.s* (*IMWS*), pp. 1-3, 2013.

[133] D.C. Ludois, J.K. Reed, K. Hanson, "Capacitive Power Transfer for Rotor Field Current in Synchronous Machines," *IEEE Trans. Power Electron.*, vol. 27, no. 11, pp. 4638-4645, Nov. 2012.

[134] D.C. Ludois, M.J. Erickson, J.K. Reed, "Aerodynamic Fluid Bearing for Translational and Rotating

Capacitors in Noncontact Capacitive Power Transfer Systems," *IEEE Trans. on Ind. Appl.*, vol. 50, no. 2, pp. 1025-1033, Mar. 2014.

[135] H. Funato, H. Kobayashi, T. Kitabayashi, "Analysis of Transfer Power of Capacitive Power Transfer System," *Proc. IEEE Intern. Conf. on Power Electron. and Drive Systems* (*PEDS*), pp. 1015-1020, 2013.

[136] T. Kitabayashi, H. Funato, H. Kobayashi, K. Yamaichi, "Experimental Verification of Capacitive Power Transfer Using One Pulse Switching Active capacitor for Practical Use," *Proc. IEEE Intern. Power Electron. Conf.*, pp. 2517-2522, 2014.

[137] J. Kim, R. Bien, "Electric Field Coupling Technique of Wireless Power Transfer for Electric Vehicles," *IEEE TENCON Spring Conf.*, pp. 267-271, 2013.

[138] S. Hall, "Capacitive Power Transfer to Car through Wheel- Is It Possible?" Lund University, 2012.

[139] K. Wang, S. Sanders, "Contactless USB – A Capacitive Power and bidirectional Data Transfer System," *Proc. IEEE Appl. Power Electron. Conf. Expo.* (*APEC*), pp. 1342-1347, Mar. 2014.

[140] D. Shmilovitz, S. Ozeri, M. Ehsani, "A Resonant LED Driver with Capacitive Power Transfer," *Proc. IEEE Appl. Power Electron. Conf. Expo.* (*APEC*), pp. 1384-1387, Mar. 2014.

[141] A.P. Hu, C. Liu, H.L. Li, "A Novel Contactless Battery Charging System for Soccer Playing Robot," *IEEE Intern. Conf. on Mech. and Mach. Vision Prac.* (*M2VIP*), pp. 646-650, 2008.

[142] J.S. Glaser, J.M. Rivas, "A 500 W Push-pull Dc-dc Power Converter with a 30 MHz Switching Frequency," *Proc. IEEE Appl. Power Electron. Conf. Expo.* (*APEC*), pp. 654-661, Mar. 2010.

[143] S. Mishira, R. Adda, S. Sekhar, A. Rathore, "Power Transfer using Portable Surfaces in Capacitively Coupled Power Transfer Technology," *IET Power Electronics*, vol. 9, no. 5, pp. 997-1008, 2016.

[144] F. Lu, H. Zhang, H. Hofmann, C. Mi, "A Dynamic Charging System with Reduced Output Power Pulsation for Electric Vehicles," *IEEE Trans. Ind. Electron.*, vol. 63, no. 10, pp. 6580-6590, Oct. 2016.

[145] F.Y. Lin, G.A. Covic, J.T. Boys, "Leakage Flux Control of Mismatched IPT Systems," *IEEE Trans. on Transportation Electrification*, 2016, doi: 10.1109/TTE.2016.2630922.

[146] *IEEE Standard for Safety Levels with Respect to Human Exposure to Radio Frequency Electromagnetic Fields*, 3kHz to 300 GHz, C95.1, 2005.

[147] H. Nishiyama, M. Nakamura, "Form and Capacitance of Parallel-Plate Capacitor", *IEEE Trans. Compen. Packag. Munufact. Tech.–Part A*, vol 17, pp. 477-484, 1994.

[148] F. Lu, H. Zhang, H. Hofmann, C. Mi, "A Double-sided LCLC-Compensated Capacitive Power Transfer System for Electric Vehicle Charging," *IEEE Trans. Power Electron.*, vol. 30, no. 11, pp. 6011-6014, Nov. 2015.

[149] F. Lu, H. Zhang, H. Hofmann, C. Mi, "An Inductive and Capacitive Combined Wireless Power Transfer System with LC-Compensated Topology," *IEEE Trans. Power Electron.*, vol. 31, no. 12, pp. 8471-8482, Dec. 2016.

[150] F. Lu, H. Zhang, H. Hofmann, C. Mi, "A Dynamic Capacitive Power Transfer System with Reduced Power Pulsation," *Proc. IEEE PELS Workshop on Emerging Technologies: Wireless Power Transfer (WoW)*, pp. 60-64, Oct. 2016.

CHAPTER II

DOUBLE-SIDED LCLC-COMPENSATED CPT SYSTEM

2.1. Introduction

The challenge in long-distance and high-power CPT systems comes from the extremely small coupling capacitances, which require either too high a switching frequency or too large a compensation inductor [1]. The full-bridge-inverter based series-inductor compensation circuit has the potential to provide high power capability [2], [3]. However, the compensation circuit needs to be improved to increase power density and efficiency [4].

One solution to reduce the large compensation inductor is to use an LCL compensation circuit [5], [6], which can provide the required inductive impedance at the specified switching frequency. At the front end, the LC circuit can also step up the voltage on the plates to increase the system power. A low-power CPT system is demonstrated, which can achieve 25W with 80% dc-dc efficiency for a laptop charging application. However, in this design, the series inductor is still required, which makes it difficult to be applied in high-power applications.

A more straightforward and effective method is to directly connect relatively large external capacitors with the coupling capacitances [7], [8]. The equivalent capacitances are therefore significantly increased, and the required compensation inductors and switching frequency are reduced, resulting in an LC compensation topology to realize CPT systems [9]. However, in this system, the power is inversely proportional to the coupling capacitances, which induces difficulty in practical applications [10].

In this chapter, a double-sided LCLC compensation circuit is proposed to realize a high-power CPT system for electric vehicle charging applications [11]. Compared to the

series-inductor compensation, it has the merit of significantly reducing the value of required compensation inductance. Compared to the LC compensation, it has two major advantages [10]: the output power is proportional to the coupling capacitances; the system efficiency can be designed to be higher. The detailed comparison will be provided in this chapter. At last, it needs to be mentioned that, although there are more passive components in the LCLC compensation circuit, the inductors can be integrated together to save space [12].

2.2. Capacitive Coupler Design

The structure and dimension of a horizontally-arranged capacitive coupler are shown in Fig. 2-1, consisting of four metal plates P_1-P_4. Plates P_1 and P_2 are horizontally placed in the same plane at the primary side as a power transmitter. Plates P_3 and P_4 are also placed in the same plane at the secondary side as a power receiver. In this design, all the plates have the same size, and the plate shape is chosen to be square to simplify the design process. In practical applications, it needs to be emphasized that the plate shape can vary according to different requirements.

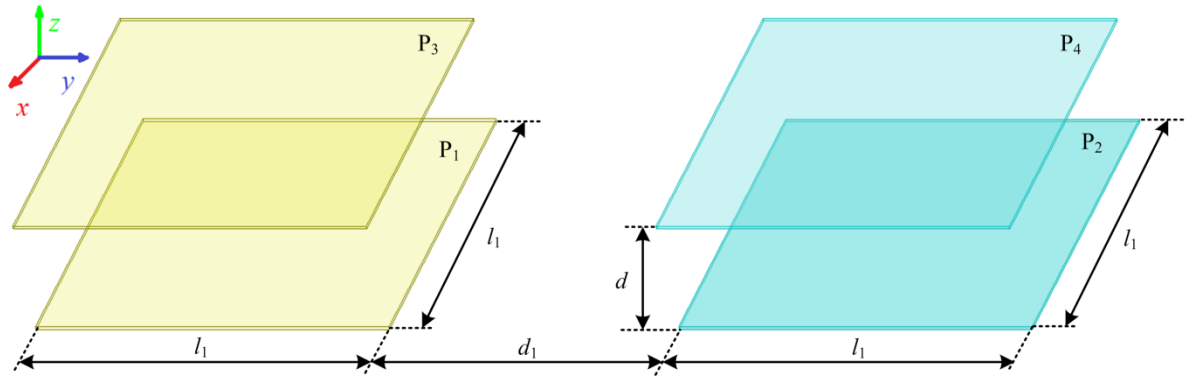

Fig. 2-1. Structure and dimension of a horizontally arranged capacitive coupler

In Fig. 2-1, the plate length is defined as l_1, the distance between same side plates is defined as d_1, and the air-gap distance between the primary and secondary plates is defined as d. The *xyz* directions are also identified, which will help when studying the misalignment performance of the coupler. In electric vehicle charging applications, the air-gap distance d is usually designed to be 150 mm, which is the ground clearance of the vehicle chassis.

In Fig. 2-1, there are coupling capacitances between each pair of plates, which introduces complexity in the circuit analysis. To simplify the circuit model, it is assumed plates P_1 and P_3 are placed far away from P_2 and P_4, which means d_1 is relatively large. Therefore, only two pairs of couplings, P_1-P_3 and P_2-P_4, need to be considered in this design. The simplified circuit model of a horizontally arranged capacitive coupler is shown in Fig. 2-2.

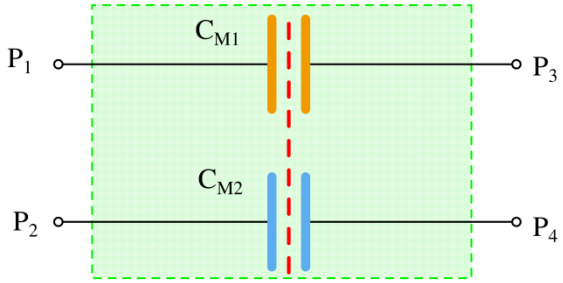

Fig. 2-2. Simplified circuit model of a horizontally arranged capacitive coupler

The coupling capacitance between P_1 and P_3 is defined as C_{M1}, and the coupling capacitance between P_2 and P_4 is defined as C_{M2}. The other capacitive couplings are neglected to simplify the circuit model. When the capacitive coupler is connected into a circuit, C_{M1} and C_{M2} form a loop for current to flow through, which means they are connected in series. Then, the equivalent coupling capacitance is defined as C_M and expressed as,

$$C_M = \frac{C_{M1} \cdot C_{M2}}{C_{M1} + C_{M2}} \tag{2-1}$$

In this design, since the four plates are identical, C_{M1}=C_{M2} and therefore C_M=C_{M1}/2. Finite element analysis (FEA) by Maxwell is used to simulate the coupling capacitances. When the plate length l_1 varies, the capacitances between plates as shown in Fig. 2-3.

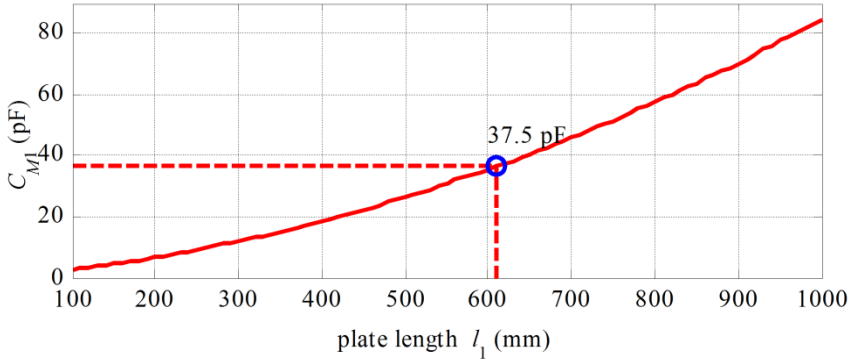

Fig. 2-3. Maxwell-simulated coupling capacitance C_{M1} at different plate lengths l_1

Fig. 2-3 shows that the coupling capacitance C_{M1} increases with increasing plate length l_1. Considering the space limitation of a vehicle chassis, l_1 can be selected to be 24 in (610 mm) as an example to design a CPT system for vehicle charging application. Fig. 2-3 indicates that the coupling capacitance C_{M1} is 37.5 pF with a plate length of 610 mm. This capacitance can also be verified by the empirical formula of parallel plate capacitance [13], in which the fringing effect of electric fields contributes to increase the coupling capacitance. Then, the capacitance is calculated to be,

$$C_{M1} = \varepsilon_0 \cdot \frac{l_1^2}{d} \cdot \left[1 + 2.343 \times \left(\frac{d}{l_1} \right)^{0.891} \right] = 36.7\text{pF} \tag{2-2}$$

where, $\varepsilon_0 = 8.85\times10^{-12}$ F/m is the permittivity of free space. The calculation result shows good agreement with the Maxwell simulated value. Since the difference is within ±2%, the simulation accuracy is then accepted.

The separation distance d_1 is chosen to be 500 mm to reduce the capacitive coupling between same side plates. The simulation also shows the plate thickness does not significantly affect the coupling capacitance, and it is selected to be 2.0 mm for installation consideration. To conclude, the dimension of the designed capacitive coupler is shown in Table II-1.

Table II-1. Dimensions of a horizontally arranged capacitive coupler

plate size l_1	610 mm	air-gap distance d	150 mm
plate thickness	2.0 mm	same side plate distance d_1	500 mm

Similar to the IPT system, there are avoidable misalignments between the transmitter and receiver in practical applications [14]. The misalignment performance of the capacitive coupler should therefore be studied [15]. As shown in Fig. 2-1, the two pairs P_1-P_3 and P_2-P_4 are placed far away from each other. Therefore, the x and y direction misalignments are considered to have the same effect, and so only the x direction misalignment is analyzed. Due to the symmetry of the coupler structure, the positive and negative misalignment performances are also the same. The Maxwell-simulated capacitance C_{M1} at different x misalignments is shown in Fig. 2-4.

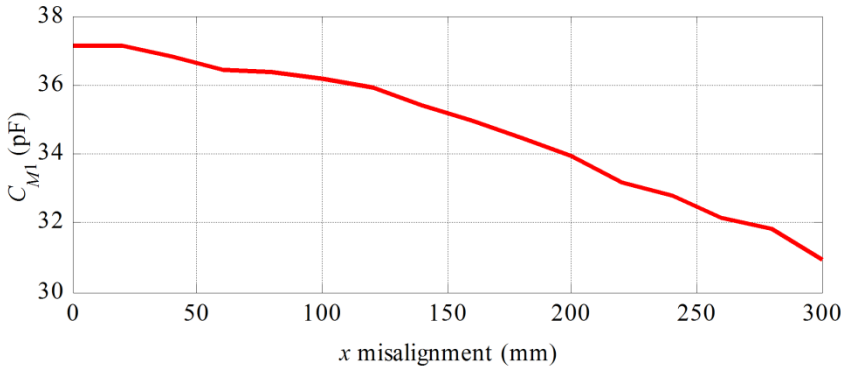

Fig. 2-4. Maxwell simulated coupling capacitance C_{M1} at different x misalignments

Fig. 2-4 shows that the coupling capacitance C_{M1} decreases with the increasing x direction misalignment. When the misalignment is 300 mm, which is about one half of the plate length l_1, C_{M1} decreases to 30.9 pF, which is about 84.2% of the well-aligned value. Therefore, it can be concluded that the horizontally-arranged capacitive coupler has good misalignment performance.

The air-gap distance d between the transmitter and receiver can also change in practical applications for different vehicles. For a passenger car, it is common to have 150 mm distance between the vehicle chassis and the gound. However, for a large size pickup truck or public transportation bus, the distance can increase to 250 mm or even 300 mm. The Maxwell-simulated capacitance C_{M1} at different air-gap distances is shown in Fig. 2-5.

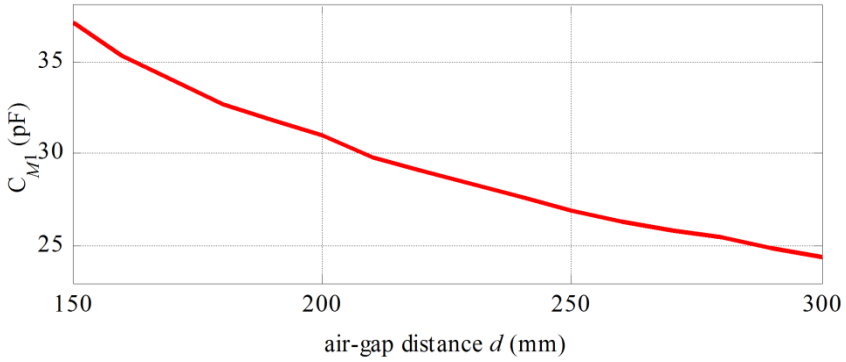

Fig. 2-5. Maxwell simulated coupling capacitance C_{M1} at different air-gap distances d

Fig. 2-5 shows that the coupling capacitance C_{M1} decreases with increasing air-gap distances as well. When the air-gap is 300 mm, which doubles the original gap distance, C_{M1} decreases to 24.4 pF, which is 66.5% of the 150 mm air-gap case.

2.3. LCLC Compensation Circuit

2.3.1. Circuit Topology

The circuit topology of a full-bridge inverter based double-sided LCLC-compensated CPT system is shown in Fig. 2-6. At the primary side, a dc voltage source V_{in} is used as the power input, and a full-bridge MOSFET inverter converts the dc voltage to a square-wave voltage to provide ac excitation to the resonant circuit. At the secondary side, a full-bridge uncontrolled diode rectifier is used to provide dc current to the load V_{out}, which can represent the batteries in an electric vehicle. Also, it needs to be pointed out that the rectifier voltage V_2 is also a square wave due to the diode action.

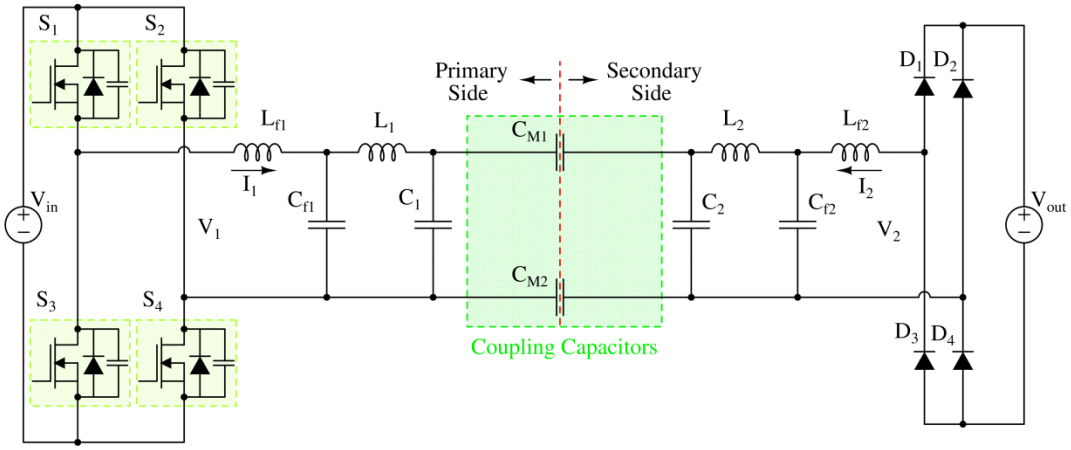

Fig. 2-6. Circuit topology of a double-sided LCLC-compensated CPT system

The horizontally-arranged capacitive coupler in Fig. 2-1 is used to realize a high-power and long-distance CPT system, in which the capacitors C_{M1} and C_{M2} are used to transfer power. At each side, an LCLC compensation circuit resonates with the capacitive coupler to boost the voltage across the plates and therefore achieve high power transfer. Capacitors C_1 and C_2 are connected in parallel with the capacitive coupler to increase the equivalent capacitances, which reduces the required switching frequency and resonant inductances L_1 and L_2. There are two parallel resonances, L_{f1}-C_{f1} and L_{f2}-C_{f2}, at the input and output sides to convert the voltage sources V_1 and V_2 to current sources. The detailed working principle of the resonant circuit is presented in the following.

2.3.2. Circuit Working Principle

Since L_{f1}-C_{f1} and L_{f2}-C_{f2} behave as low-pass filters, the square wave input and output voltages can be replaced by sinusoidal voltages to simplify the circuit analysis, and the high-order current harmonics can be neglected. The RMS values of the voltages are expressed as,

$$\begin{cases} V_1 = \dfrac{2\sqrt{2}}{\pi} \cdot V_{in} \\ V_2 = \dfrac{2\sqrt{2}}{\pi} \cdot V_{out} \end{cases} \tag{2-3}$$

The fundamental harmonics approximation (FHA) method is then used to analyze the circuit working principle as shown in Fig. 2-7. The power losses of the circuit components are also neglected to further simplify the analysis.

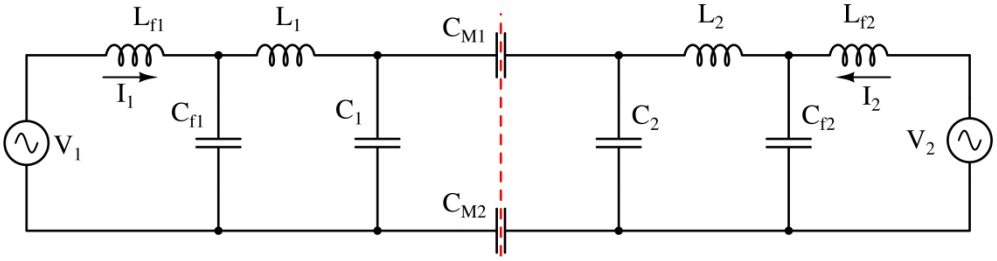

(a) Simplified resonant circuit

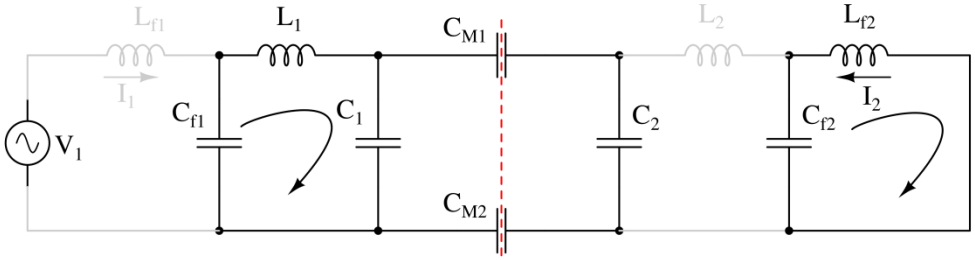

(b) Components excited by input source

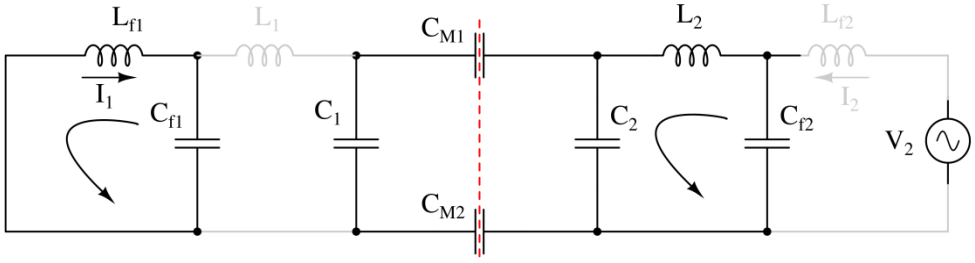

(c) Components excited by output source

Fig. 2-7. Fundamental harmonics approximation of a double-sided LCLC-compensated CPT system

Fig. 2-7(a) shows the simplified resonant circuit model, in which two sinusoidal voltages are applied at the input and output sides. Since there are two dependent voltage sources, the superposition theorem can be used to separate the circuit analysis into two analyses.

Fig. 2-7(b) shows the circuit components excited only by the input voltage. There are two parallel resonances highlighted in the circuit. The inductor L_{f2} and capacitor C_{f2} form a parallel resonance. The equivalent capacitance of C_{M1} and C_{M2} is defined in (2-1) as C_M. Capacitors C_1, C_M, and C_2 work as an equivalent capacitance C_{p1} for the primary side. The inductor L_1 and capacitors C_{f1} and C_{p1} form the other resonance. The resonant frequency is defined as ω_0. Then, the relationship between the parameters is expressed as,

$$\begin{cases} L_{f2} = \dfrac{1}{\omega_0^2 \cdot C_{f2}} \\ C_{p1} = C_1 + \dfrac{C_M \cdot C_2}{C_M + C_2} \\ L_1 = \dfrac{1}{\omega_0^2 \cdot C_{p1}} + \dfrac{1}{\omega_0^2 \cdot C_{f1}} \end{cases} \tag{2-4}$$

When the resonant conditions are satisfied, L_{f2} and C_{f2} behave as open circuit for L_2, so there is no current flowing through L_2. Also, L_1, C_{f1}, and C_{p1} behave as open circuit, and there is no current flowing through L_{f1}, which means the input current is independent of the input voltage.

Fig. 2-7 (c) shows the circuit components excited only by the output voltage. There are also two parallel resonances. The inductor L_{f1} and capacitor C_{f1} form a parallel resonance. The capacitors C_1, C_M and C_2 work as an equivalent capacitance C_{p2} for the secondary side. Then, L_2, C_{f2} and C_{p2} form the other resonance. The relationship between the parameters is expressed as,

$$\begin{cases} L_{f1} = \dfrac{1}{\omega_0^2 \cdot C_{f1}} \\ C_{p2} = C_2 + \dfrac{C_M \cdot C_1}{C_M + C_1} \\ L_2 = \dfrac{1}{\omega_0^2 \cdot C_{p2}} + \dfrac{1}{\omega_0^2 \cdot C_{f2}} \end{cases} \tag{2-5}$$

Similar to Fig. 2-7(b), there is no current flowing through L_1 and L_{f2}, which means the output current is independent of the output voltage. It can be concluded that the double-sided LCLC-compensated CPT system behaves as a current source at both the input and output.

2.3.3. Output Power Calculation

In Fig. 2-7(b), since there is no current flowing through L_{f1}, the voltage on C_{f1} is equal to the input voltage V_1, and the voltage on C_1 is calculated as,

$$V_{C1} = -V_1 \cdot \frac{C_{f1}}{C_{p1}} \tag{2-6}$$

Also, since there is no current flowing through L_2, the voltage on C_{f2} is equal to the voltage on C_2, which is expressed as,

$$V_{Cf2} = V_{C2} = -V_1 \cdot \frac{C_{f1}}{C_{p1}} \cdot \frac{C_M}{C_M + C_2} \tag{2-7}$$

Therefore, the output current ($-I_2$) is expressed as,

$$-I_2 = -V_1 \cdot \frac{C_{f1}}{C_{p1}} \cdot \frac{C_M}{C_M + C_2} \cdot \frac{1}{j\omega_0 \cdot L_{f2}} \tag{2-8}$$

In Fig. 2-7(c), there is no current flowing through L_{f2}, and the voltage on C_{f2} is equal to the output voltage V_2. Then, the voltage on C_2 is expressed as,

$$V_{C2} = -V_2 \cdot \frac{C_{f2}}{C_{p2}} \tag{2-9}$$

There is no current flowing through L_1, and the voltage on C_{f1} is expressed as,

$$V_{Cf1} = V_{C1} = V_2 \cdot \frac{C_{f2}}{C_{p2}} \cdot \frac{C_M}{C_M + C_1} \tag{2-10}$$

Therefore, the input current I_1 is expressed as,

$$I_1 = V_2 \cdot \frac{C_{f2}}{C_{p2}} \cdot \frac{C_M}{C_M + C_1} \cdot \frac{1}{j\omega_0 \cdot L_{f1}} \tag{2-11}$$

Considering parameter relationships in (2-4) and (2-5), the currents are simplified as,

$$\begin{cases} I_1 = -j\omega_0 C_M \cdot \dfrac{C_{f1} \cdot C_{f2}}{C_1C_2 + C_1C_M + C_2C_M} \cdot V_2 \\ -I_2 = j\omega_0 C_M \cdot \dfrac{C_{f1} \cdot C_{f2}}{C_1C_2 + C_1C_M + C_2C_M} \cdot V_1 \end{cases} \tag{2-12}$$

It shows that the output current ($-I_2$) is leading the input voltage V_1 by 90°, and the input current is lagging the output voltage V_2 by 90°. Since an uncontrolled diode rectifier is used at the secondary side, the output voltage V_2 must be in phase with the output current ($-I_2$). Therefore, the input voltage V_1 is in phase with the input current I_1. Unity power factor is therefore achieved

at the input side and the reactive power injected into the resonant circuit is limited, which helps to reduce power losses.

Using the currents in (2-12), the system input and output power can be further expressed as,

$$P_{in} = P_{out} = \omega_0 C_M \cdot \frac{C_{f1} \cdot C_{f2}}{C_1 C_2 + C_1 C_M + C_2 C_M} \cdot |V_1| \cdot |V_2| \tag{2-13}$$

This shows that the input and output power are equal to each other, which is consistent with the previous assumption to neglect the power losses in the circuit components. This power equation is expressed by the capacitances and is similar to the power equation of double-sided LCC-compensation IPT system [18], in which inductances are used to calculate power.

In the compensation circuit, capacitors C_1 and C_2 are usually designed to be much larger than C_M, which means $C_1 >> C_M$ and $C_2 >> C_M$. Then, the output power is approximated to be,

$$P_{out} \approx \omega_0 C_M \cdot \frac{C_{f1} \cdot C_{f2}}{C_1 C_2} \cdot |V_1| \cdot |V_2| \tag{2-14}$$

This shows that the system power is approximately proportional to the coupling capacitance C_M, and so C_M should be maximized.

In the LCLC-compensated CPT system, the mutual capacitance is defined to be the coupling capacitance C_M of the capacitive coupler, the primary and secondary equivalent self-capacitances can be defined as C_{eq1} and C_{eq2}, and the capacitive coupling coefficient is defined as k_C. Also, the capacitance ratios between the compensation capacitances are defined as β_1 and β_2. Therefore, the parameters are expressed as,

$$\begin{cases} C_{eq1} = C_1 + C_M \\ C_{eq2} = C_2 + C_M \\ k_C = C_M / \sqrt{C_{eq1} C_{eq2}} \\ \beta_1 = C_{eq1} / C_{f1}, \beta_2 = C_{eq2} / C_{f2} \end{cases} \tag{2-15}$$

The system power equation in (2-13) can then be simplified as,

$$P_{out} = \frac{\omega_0 C_M}{(1 - k_C^2) \cdot \beta_1 \beta_2} \cdot |V_1| \cdot |V_2| \tag{2-16}$$

This shows that the system output power is inversely proportional to the product of the capacitance ratios β_1 and β_2, and so the system power can be set through design of the compensation capacitances even with very small value of C_M.

2.3.4. CLLC Compensation Circuit

In an LCLC-compensated CPT system, the inductors L_1 and L_2 are usually the largest circuit components in volume, especially when they have an air-core for high frequency applications. Inside the inductor, there are parasitic capacitances between the adjacent windings, which can change the impedances of the inductor at high frequencies. The parasitic capacitance can also cause self-resonance of the inductor at high frequency. Therefore, it is necessary to decrease the required inductances to reduce their size and shift the self-resonant frequency of the inductors far away from the switching frequency.

The CLLC compensation [16] circuit can help to reduce the inductors L_1 and L_2, and its circuit topology is shown in Fig. 2-8. Compared to the LCLC compensation circuit, the positions of L_{f1} and C_{f1} are exchanged at the primary side, and the position of L_{f2} and C_{f2} are exchanged at the secondary side. The other components positions remain the same.

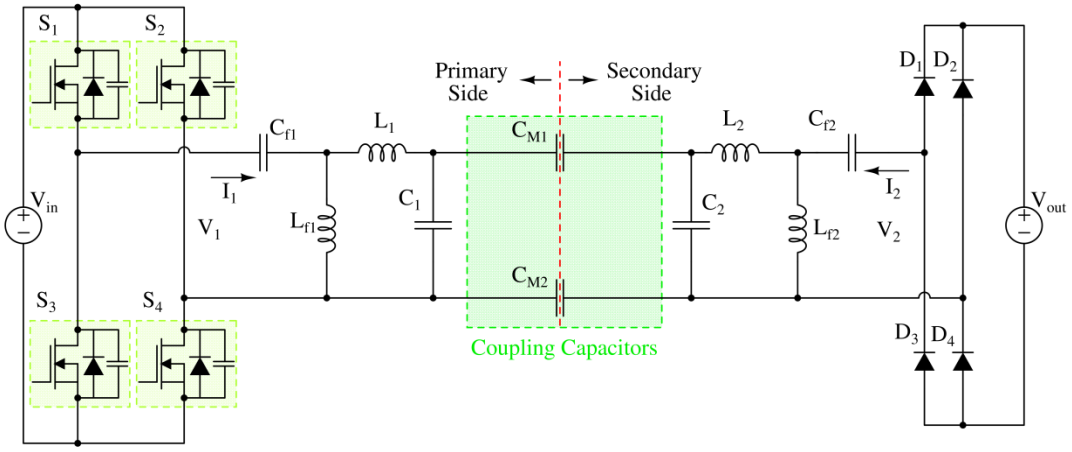

Fig. 2-8. Circuit topology of a double-sided CLLC-compensated CPT system

There are multiple resonances in the circuit and the FHA method and superposition theorem can also be used to analyze the circuit working principle. The analysis is similar to the LCLC compensation circuit in previous section; the only difference is the expressions of inductors L_1 and L_2, which can be shown to be,

$$\begin{cases} L_1 = \dfrac{1}{\omega_0^2 \cdot C_{p1}} - \dfrac{1}{\omega_0^2 \cdot C_{f1}} \\ L_2 = \dfrac{1}{\omega_0^2 \cdot C_{p2}} - \dfrac{1}{\omega_0^2 \cdot C_{f2}} \end{cases} \tag{2-17}$$

Compared to (2-4) and (2-5), the inductances L_1 and L_2 in the CLLC compensation circuit are smaller than those in the LCLC compensation circuit. Since the resonant relationships are not changed, further analysis of the system power shows that the power expressions of CLLC- and LCLC-compensated CPT systems are the same [16]. The circuit analysis shows that both the CLCL and LCLC compensation circuits are suitable to realize a high-power CPT system. In reference [16], a prototype is designed and implemented to validate the CLLC compensation, which shows that the prototype achieves 2.57 kW power transfer across an air-gap distance of 150 mm with a dc-dc efficiency of 89.3%.

2.4. Example Double-Sided LCLC-Compensated CPT System

2.4.1. Circuit Parameter Design

In this section, an example of double-sided LCLC-compensated CPT system is designed based on the horizontally-arranged capacitive coupler discussed in the previous section. Since the capacitive coupler structure is symmetric, the circuit parameters are also designed to be symmetric from the primary to secondary sides to simplify the parameter design process, resulting in C_1=C_2, C_{f1}=C_{f2}, L_1=L_2, and L_{f1}=L_{f2}.

In this example, the system input power is set to be 2.6 kW, the input dc voltage V_{in} is 265V, the output dc voltage V_{out} is 280V, and the switching frequency f_{sw} is set to be 1 MHz. It needs to be emphasized that, in practical applications, the input and output voltages and system power level can vary according to the requirements. Using the capacitance calculation equations in (2-1) and (2-2), the mutual coupling capacitance C_M is 18.35 pF. According to the system power equation (2-13), the capacitances can be calculated. Then, with the help of resonance relationships in (2-4) and (2-5), the resonant inductances can be further calculated. There are multiple parameter combinations that can satisfy the equations. Since the capacitive coupling coefficient k_C is an important specification to evaluate a CPT system [10], it is selected as the primary parameter that needs to be determined first. When k_C varies between 0.10 and 0.20, the other compensation parameters are shown in Fig. 2-9.

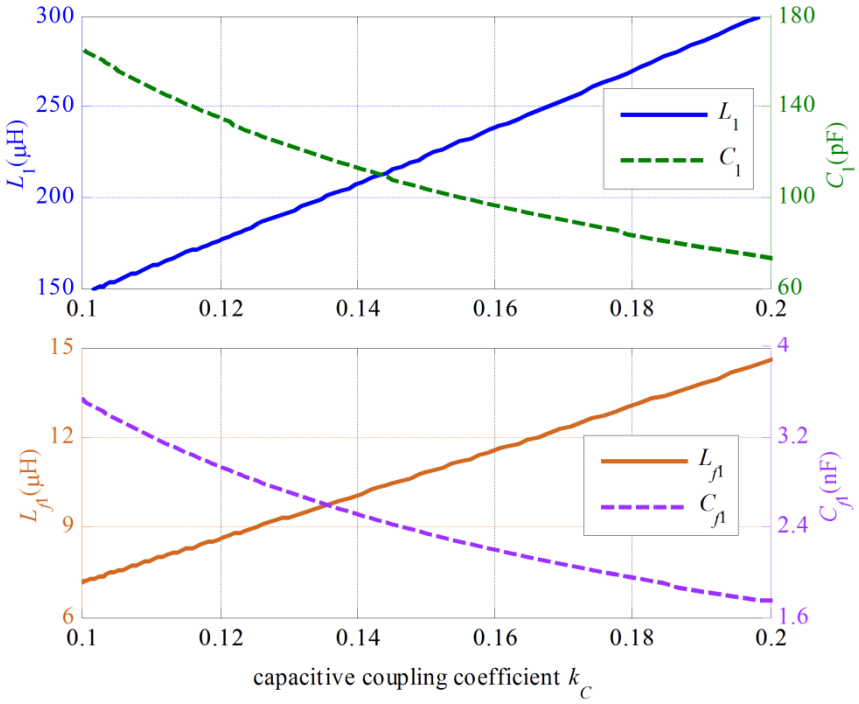

Fig. 2-9. Parameters of LCLC compensation circuit at different k_C

Fig. 2-9 shows that the capacitances C_1 and C_{f1} decrease with increasing k_C. Since the switching frequency is fixed at 1 MHz, smaller capacitances require larger compensation inductances to resonate with them. If capacitive coupling coefficient k_C varies from 0.10 to 0.20, the inductance L_1 increases from150 μH to 300 μH. Larger inductances means more turns are required to wind the inductor and the parasitic capacitance is therefore increased, which can reduce the self-resonant frequency of the inductor. In this design, k_C is selected to be 0.15 and the circuit parameters are calculated and shown in Table II-2.

Table II-2. System specifications and circuit parameters

Parameter	Value	Parameter	Value
V_{in}	265 V	V_{out}	280V
f_{sw}	1 MHz	k_C	0.15
L_{f1} (L_{f2})	11.6 μH	C_{f1} (C_{f2})	2.18 nF
L_1	231 μH	C_1 (C_2)	100 pF
L_2	242 μH	C_M	18.35 pF

2.4.2. Circuit Simulation

In Table II-2, the inductance L_2 is about 5% larger than L_1 in order to make the input current slightly lagging the input voltage and provide a soft-switching condition to the input MOSFETs. The other circuit parameters are symmetric as designed. Using the parameters in Table II-2, the circuit performance is simulated in LTspice. The power losses in circuit components are not considered to be consistent with the previous circuit analysis. The simulated input and output waveforms of the voltages and currents are shown in Fig. 2-10.

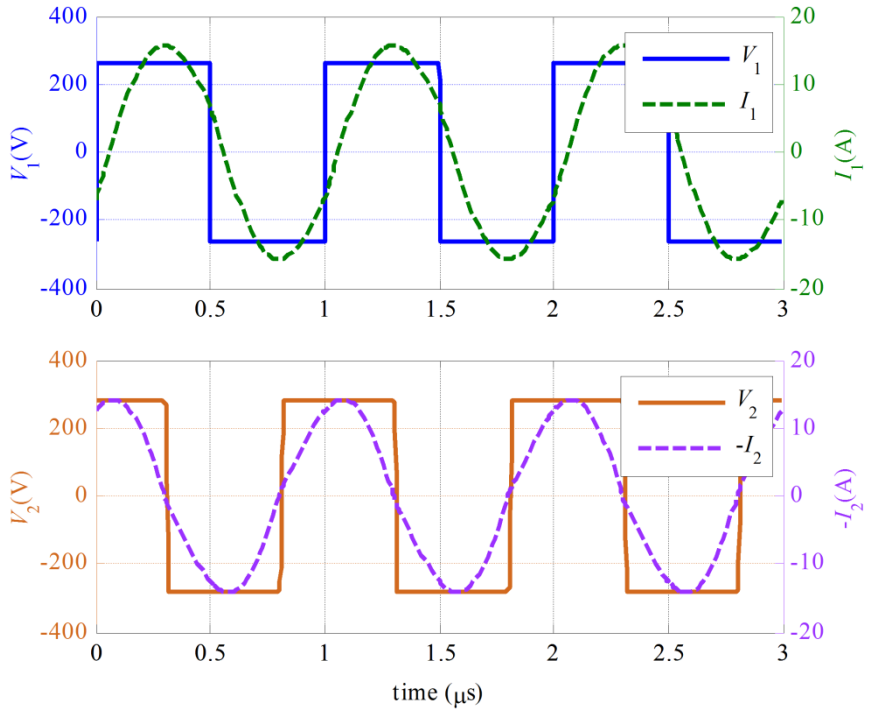

Fig. 2-10. LTspice-simulated input and output waveforms of and LCLC-compensated CPT system

Fig. 2-10 shows that, at the input side, the voltage V_1 is almost in phase with the input current I_1, and unity power factor is approximately achieved. At the output side, the voltage V_2 is in phase with the output current ($-I_2$). Therefore, the reactive power circulating in the circuit is reduced and the power losses are limited, so the system can achieve a relatively high efficiency. At the switching transient, the input cut-off current is about 3A to help the soft-switching of the input MOSFETs. The waveforms also show that there is distortion in the input and output currents, which are caused by the higher-order voltage harmonics.

2.5. Experimental Results of Double-Sided LCLC-Compensated CPT System

2.5.1. Experimental Setup

According to the designed capacitive coupler dimensions in Table II-1 and the circuit parameters in Table II-2, a prototype of double-sided LCLC-compensated CPT system was constructed and shown in Fig. 2-11.

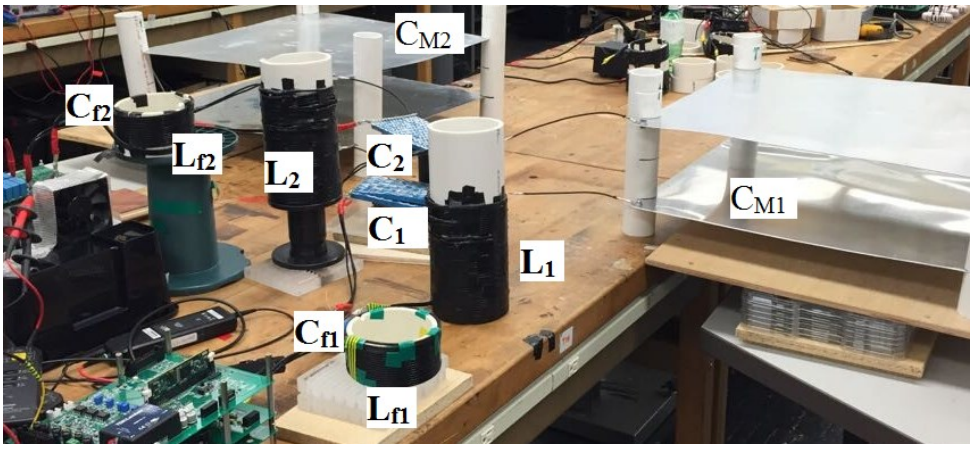

Fig. 2-11. Prototype of a double-sided LCLC-compensated CPT system

Two pairs of 610 mm×610 mm aluminum plates with a thickness of 2 mm are used as the capacitive coupler, forming two coupling capacitances C_{M1} and C_{M2}. The separation between the two pairs is 500 mm to reduce their coupling, and the air-gap distance is 150 mm. PVC tubes are used as the holders of plates. It is simple to adjust the position of the plates to test the misalignment performance.

Since the switching frequency is 1 MHz and the resulting skin depth of copper is as small as 65.2 μm, AWG 46 Litz-wire with a diameter of 40 μm is used to make the compensation inductors. The conduction losses in the inductors are therefore reduced. Meanwhile, all the inductors are wound on PVC tubes and so have an air core, and therefore magnetic losses are eliminated. In the setup, the inductors are placed far from one another to limit undesired magnetic couplings between them. The compensation capacitors C_1, C_2, C_{f1} and C_{f2} are made using high frequency film capacitors from KEMET to reduce the conduction losses. Multiple capacitors are connected in series and parallel to provide sufficient voltage and current ratings.

Since the switching frequency is 1 MHz, silicon carbide (SiC) MOSFETs (C2M0080120D from CREE) are used in the input inverter to provide high frequency switching ability. The gate driver voltage of the MOSFET is between 0V to +15V, which is the same as the conventional silicon devices. A digital micro-controller TMS320F28335 from Texas Instruments is used to generate the PWM control signal for the MOSFETs. In the digital controller, it is very convenient to adjust the frequency and dead-time for the full-bridge inverter. In this design, the dead-time is set to be 60ns. At the output side, SiC diodes IDW30G65C from Infineon are used in the rectifier to convert high-frequency ac current to dc form. An electronic dc load working in constant-voltage mode is used to emulate the batteries on an electric vehicle.

2.5.2. Experimental Results

A. Well-Aligned Case

In the experiments, the well-aligned case is studied first. At nominal input and output voltages, the experimental results are shown in Fig. 2-12.

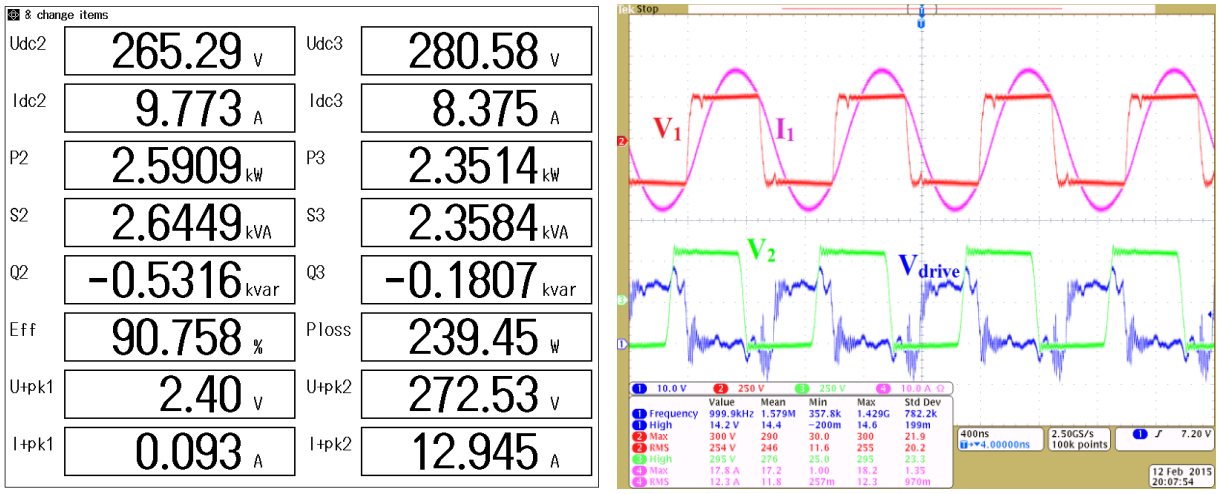

(a) power (b) waveforms

Fig. 2-12.Experimental results of the LCLC-compensated CPT system at well-aligned position

Fig. 2-12(a) shows that, in the well-aligned case, the maximum system input power is 2.59 kW and the output power is 2.35 kW. The system dc-dc efficiency from the dc source to the dc load is therefore 90.8%, including the losses in MOSFETs and diodes.

Fig. 2-12(b) shows the experimental waveforms of the voltages and current, which agree with the simulated waveforms in Fig. 2-10. At the switching transient, the input voltage changes smoothly with a small ripple, and the soft-switching of the MOSFETs is achieved. The switching losses in the devices can then be neglected. The input voltage V_1 and current I_1 are almost in phase, reducing the reactive power injected into the circuit. For the driver voltage, it needs to be emphasized that there is noise induced by the switching behavior of the MOSFETs. However, the amplitude does not exceed 3V, which is lower than the threshold voltage of the MOSFETs. Therefore, it is safe to use this voltage to drive the MOSFETs.

The power loss distribution is also analyzed in the full-power and well-aligned case, and is shown in Fig. 2-13. The power losses in the compensation inductors, capacitors, and semiconductor devices are calculated using their resistances in datasheets and measurements [17]. The remaining losses are assumed to be in the coupling plates.

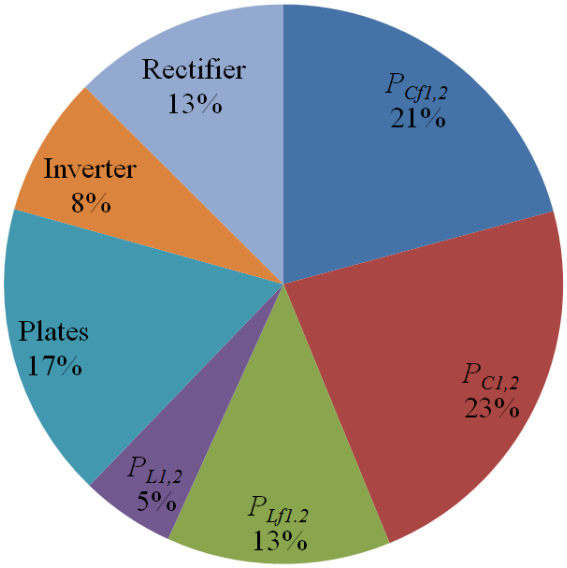

Fig. 2-13. Power losses distributions among circuit components in full-power and well-aligned case

Fig. 2-13 shows that the compensation capacitors C_1, C_2, C_{f1}, and C_{f2} dissipate 43% of the total losses. Therefore, better film capacitors with lower dissipation factor need to be used in future designs to improve the efficiency. Also, the metal plates dissipate 17% of the total losses. Since the plates also behave as good heatsink, there is no apparent temperature rise on the plates.

B. Misalignment Case

Since the misalignment between transmitter and receiver is very common in vehicle charging applications, the misalignment performance of the designed CPT system is also studied. When the receiver is moved in the *x* direction (as indicated in Fig. 2-1), the experimental output power and efficiencies are shown in Fig. 2-14.

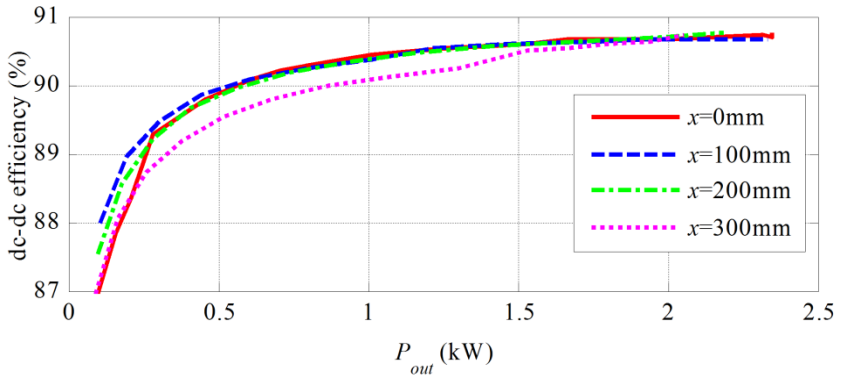

Fig. 2-14. Experimental results of LCLC-compensated CPT system at *x* misalignments

In the experiment, three different *x* misalignment positions, 100 mm, 200 mm, and 300 mm, are tested, and are compared with the well-aligned case. At each position, the input and output voltages increase from zero to the nominal values with 10V as a step, and the output power and efficiency are measured at each voltage step, as shown in Fig. 2-14. This indicates that the system efficiency increases with the output power, likely because the power electronics converters are more efficient at higher power.

Comparing different *x* misalignment cases, the system output power and efficiency decrease with increasing misalignment. When there is no misalignment, the maximum output power is 2.35 kW and the corresponding dc-dc efficiency is 90.8%, which are also the experimental results in Fig. 2-12. When the misalignment increases to 300 mm (half of the plate length l_1), the system output power decreases to 2.10 kW and the dc-dc efficiency does not change too much, which is about 90.7%. In an LCC-compensated IPT system with a 600 mm×800 mm inductive coupler [18], the system output power drops to 56% of the well-aligned value at 310 mm misalignment. Therefore, it can be concluded that the LCLC-compensation CPT system has better misalignment performance than the IPT system.

C. Air-Gap Variations

The air-gap distance variation also needs to be studied. In these experiments, the receiver is moved in the z direction (as indicated in Fig. 2-1), and the experimental output power and efficiency at different air gaps are shown in Fig. 2-15.

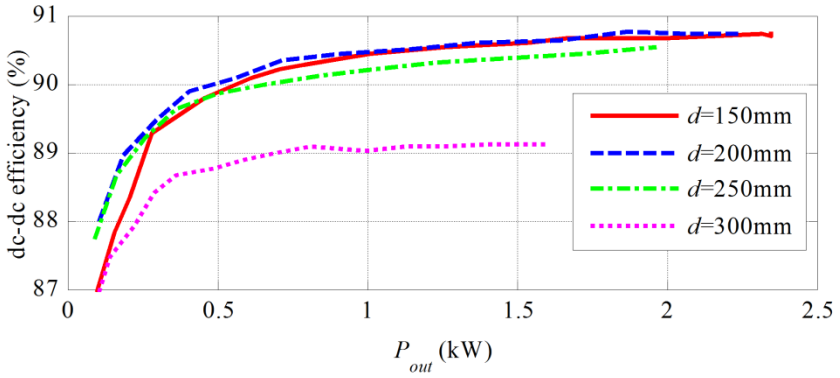

Fig. 2-15. Experimental results of LCLC-compensated CPT system at air-gap distance d variations

In practical applications, the ground clearance of vehicle chassis can vary, depending on the size the loading condition of the vehicle. For some heavy duty pick-up truck, it can increase to 300 mm. Therefore, including the original 150 mm air-gap, three other distances, 200 mm, 250 mm, and 300 mm, are also tested in the experiments. At each air-gap distance, the input and output voltages increase with 10V as a step to the nominal values, and the output power and efficiency are measured at each step. It can be seen that, similar as Fig. 2-14, the system efficiency here also increases with the output power.

When the air-gap distance increases, the mutual coupling capacitances between the transmitter and receiver decrease, which can cause reductions in system power and efficiency. Comparing different air-gap distance cases in Fig. 2-15, it validates that both the system output power and efficiency decrease with increasing air-gap. When the air-gap distance increase to 200mm, the output power is 2.3 kW and the dc-dc efficiency is 90.8%. When the air-gap distance increases to 300 mm, the system output power drops to 1.6 kW with a dc-dc efficiency of 89.1%, which means the system can achieve 67% of the nominal power. Compared to the conventional IPT system [18], in which the system power drops by more than half with doubled air-gap distance, it can be conclude that the CPT system has good robustness to air-gap variations.

2.6. Discussion: Comparison between LC and LCLC Compensation

The LC compensation network can also be used to realize a high-power and long-distance CPT system [10]. Then, the circuit topology of a double-side LC-compensated CPT system is shown in Fig. 2-16.

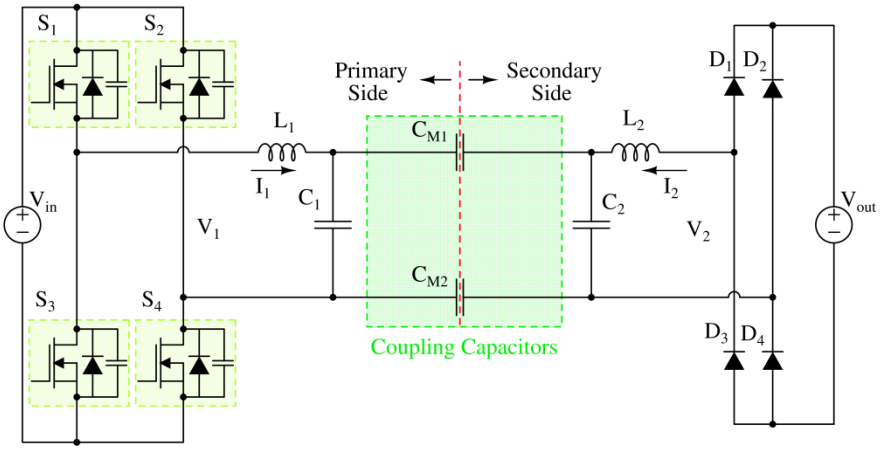

(a) Full-circuit topology

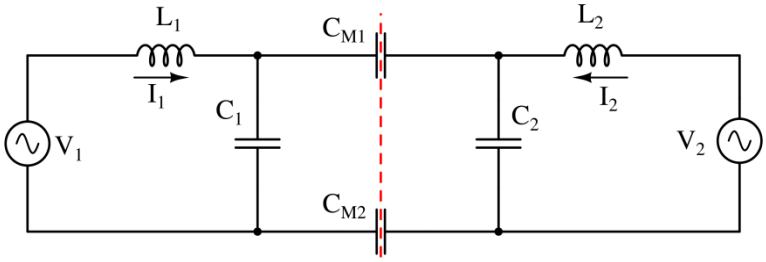

(b) Fundamental harmonics approximation

Fig. 2-16. Circuit topology of a double-sided LC-compensated CPT system

Compare to the LCLC compensation circuit, Fig. 2-16 shows that the LC circuit can reduce the number of compensation components to reduce the complexity of the system. It can also help to reduce the system size and cost. Using the fundamental harmonics approximation method in section 2.3.2, the full-circuit model in Fig. 2-16(a) can be simplified as Fig. 2-16(b), which is used to analyze the circuit working principle, including the resonance relationship and output power [10]. With these analyses, the circuit performance of an LC-compensated CPT system will be compared with that of an LCLC-compensated system from two aspects: output power and system efficiency.

A. Output Power Property

Analysis of Fig. 2-16(b) shows that there are multiple resonances in the circuit, and it can work in either constant voltage or constant current mode [10]. Considering the battery charging application, the constant current mode is used in the comparison. Neglecting the power loss in components, the output power of the LC- and LCLC-compensated CPT systems is expressed as,

$$\begin{cases} P_{LC} = \omega_0 \cdot \dfrac{C_1 C_2 - C_M^2}{C_M} \cdot |V_1| \cdot |V_2| \\ P_{LCLC} = \omega_0 C_M \cdot \dfrac{C_{f1} \cdot C_{f2}}{C_1 C_2 + C_1 C_M + C_2 C_M} \cdot |V_1| \cdot |V_2| \end{cases} \tag{2-18}$$

Usually, there are $C_1 >> C_M$ and $C_2 >> C_M$. Then, it can be further simplified as,

$$\begin{cases} P_{LC} = \omega_0 \cdot \dfrac{C_1 C_2}{C_M} \cdot |V_1| \cdot |V_2| \\ P_{LCLC} = \omega_0 C_M \cdot \dfrac{C_{f1} \cdot C_{f2}}{C_1 C_2} \cdot |V_1| \cdot |V_2| \end{cases} \tag{2-19}$$

In an LC-compensated CPT system, when the capacitive coupler has been designed, the mutual capacitance C_M is determined. Then, the system power can be regulated through adjusting the external compensation capacitors C_1 and C_2. To achieve higher power means higher C_1 and C_2. However, according to (2-15), the coupling coefficient k_C is then decreased. Further study shows that lower k_C can reduce the system efficiency, as will be shown in the sequel.

In an LCLC-compensated CPT system, there is more flexibility to design the circuit parameters. After C_M is determined, the system power can be regulated through adjust the capacitance ratio β_1 and β_2, as defined in (2-15). To increase the system power, the capacitance C_1 and C_2 can stay unchanged, and β_1 and β_2 needs to be reduced, which means increasing the compensation capacitors C_{f1} and C_{f2}. In this way, the coupling coefficient k_C is not reduced, and the influence to system efficiency is minimized.

It shows that the output power of an LC-compensated CPT system is inversely proportional to the mutual capacitance C_M. While, the output power of an LCLC-compensated CPT system is proportional to C_M. If there is misalignment in a CPT system, the LC compensation can lead to an increase of system power, which may exceed the voltage and current ratings of circuit

components, which might cause danger. It needs to be pointed out that, with decreasing C_M, the output power first increase, and then decrease if C_M is too small. In that case, the parasitic resistances of the circuit components will have significant influence to system performance, and it will be investigated in future research.

B. System Efficiency

In Fig. 2-16(a), the output side voltage source V_2 can be represented by an equivalent load resistance R_L to analyze its efficiency. Considering the power loss in components, the efficiency of an LC-compensated network (i.e. not including inverter and rectifier losses) is expressed as,

$$\eta_{LC} = \frac{I_{RL}^2 \cdot R_L}{I_{RL}^2 \cdot R_L + I_{L2}^2 \cdot R_{L2} + I_{C2}^2 \cdot R_{C2} + I_{C1}^2 \cdot R_{C1} + I_{L1}^2 \cdot R_{L1}} \tag{2-20}$$

where, R_{L2}, R_{C2}, R_{C1}, and R_{L1} are the parasitic resistances of the passive components, and I_{RL}, I_{L2}, I_{C2}, I_{C1}, and I_{L1} are the currents flowing through these components. The magnitude of current can be calculated using the fundamental harmonic approximation method in section 2.3.2. According to [10], (2-20) is further simplfied to get the the maximum efficiency as,

$$\eta_{LC,\max} = \frac{1}{1 + \frac{2}{k_C^2 Q^2} + \frac{2}{k_C Q}\sqrt{1 + \frac{1}{k_C Q}}} \tag{2-21}$$

where, Q is the quality factor of the primaryand secondary circuit.

In Fig. 2-7(a), the output side voltage source V_2 can also be represented by R_L to analyze its efficiency. Similarly, considering the power loss in components, the efficiency of an LCLC-compensated netwok (i.e. not including inverter and rectifier losses) is expressed as,

$$\eta = \frac{I_{RL}^2 \cdot R_L}{I_{RL}^2 \cdot R_L + I_{Lf2}^2 \cdot R_{Lf2} + I_{Cf2}^2 \cdot R_{Cf2} + I_{L2}^2 \cdot R_{L2} + I_{C2}^2 \cdot R_{C2} + I_{C1}^2 \cdot R_{C1} + I_{L1}^2 \cdot R_{L1} + I_{Cf1}^2 \cdot R_{Cf1} + I_{Lf1}^2 \cdot R_{Lf1}} \tag{2-22}$$

According to [10], (2-22) is further simplified to get the maximum efficiency as,

$$\eta_{LCLC,\max} = \frac{1}{1 + \frac{2}{k_C Q} \cdot \left(1 + \frac{k_C^2}{\beta}\right)} \tag{2-23}$$

where, Q is the quality factor of the primaryand secondary circuit, and β is the capacitance ratio. Here, it is assumed that $\beta=\beta_1=\beta_2$.

According to (2-21) and (2-23), the maximum achievable efficiency of the LC- and LCLC-compensated CPT networks is shown in Fig. 2-17.

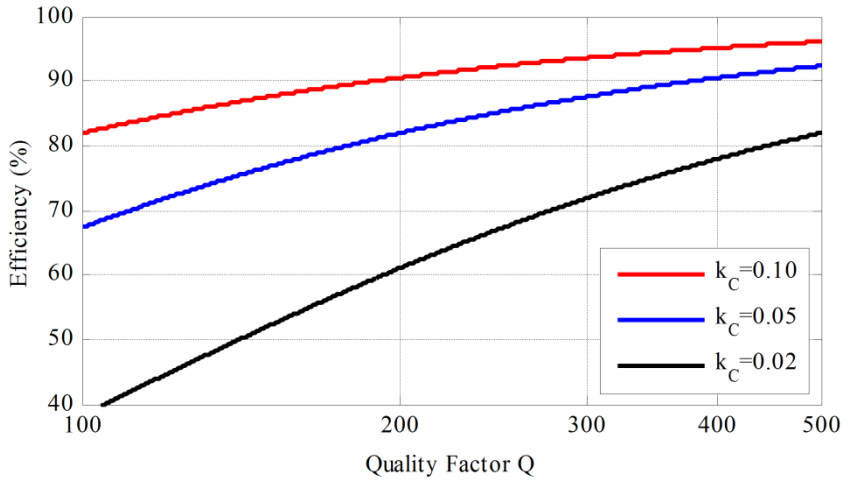

(a) LC compensation

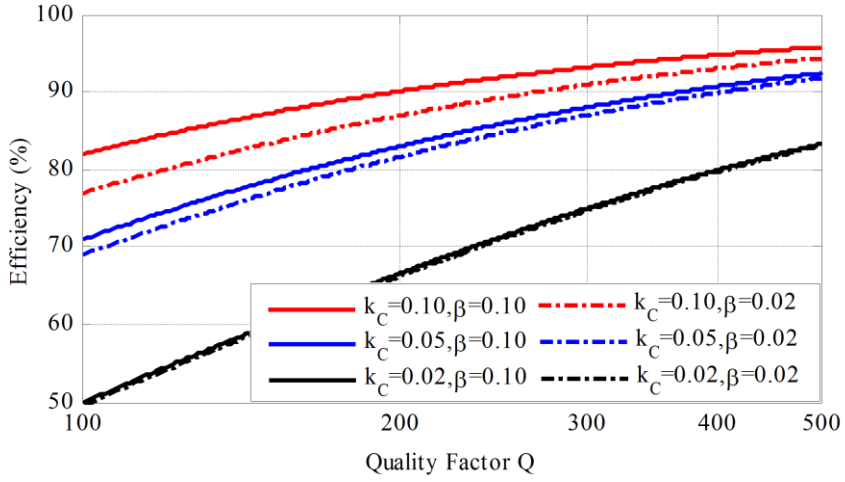

(b) LCLC compensation

Fig. 2-17. Theoretical Maximum achievable efficiency of LC- and LCLC-compensated CPT networks

Fig. 2-17 shows that, in both LC- and LCLC-compensated networks, increasing the capacitive coupling coefficient k_C and the quality factor Q contributes to increase the system efficiency. For example, in an LC-compensated CPT system, as long as the quality factor exceeds 200, the maximum efficiency can reach 90%. In an LCLC-compensated CPT system, the capacitance ratio β also relates to the efficiency. According to (2-16), smaller β helps to increase the system power, but the system efficiency is then reduced.

It is informative to compare the efficiencies of the LC- and LCLC-compensated CPT networks with the same capacitive coupler and the same power level. In the comparison, the coupling coefficients of the LC-compensated and LC-compensated networks are defined as k_{LC} and k_{LCLC}, respectively. According to the power equations in (14), the value of k_{LC} must be set equal to the value of β in the LCLC system to achieve equal power. Therefore, based on (2-21) and (2-23), the optimum efficiency of the LC-compensated system is less than that of the LCLC-compensated system (i.e. $\eta_{LC,max} < \eta_{LLCC,max}$) when,

$$k_{LCLC}^2 - \left(\frac{1}{k_{LC} Q} + \sqrt{1 + \frac{1}{k_{LC} Q}} \right) \cdot k_{LCLC} + k_{LC} < 0 \tag{2-24}$$

Based on (2-24), the efficiencies of the compensation networks are compared in Fig. 2-18.

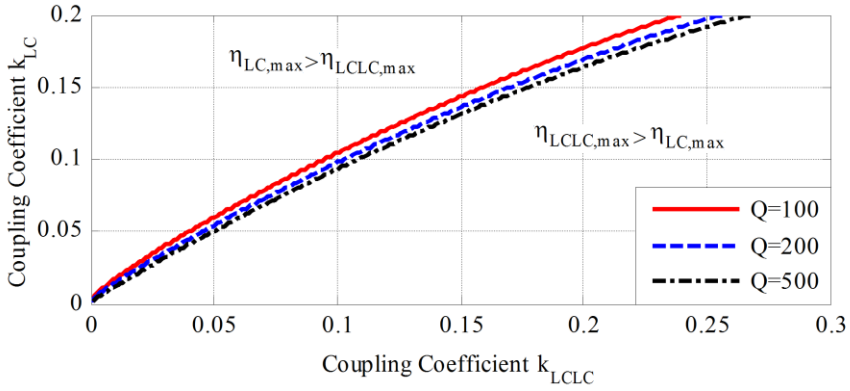

Fig. 2-18. Comparison of efficiencies of LC- and LCLC-compensation networks

The area between the curves and the x-axis is the region where the LCLC-compensated system has higher efficiency, and the area between the curves and the y-axis is the region where the LC-compensated system has higher efficiency.

Fig. 2-18 shows that the coupling coefficient dominates the comparison of efficiency between two different compensations, and influence of quality factor Q is relatively minor. When the two systems have the same coupling coefficient, the LC compensation can provide higher frequency because of fewer components. However, in a practical design, the LCLC compensation has the flexibility to adjust β to regulate system power, and the coupling coefficient can be maintained at relatively higher value. Therefore, the LCLC compensation can provide high efficiency than the LC compensation.

2.7. Conclusion

In this chapter, a double-sided LCLC compensation circuit topology has been proposed to achieve high-power and long-distance capacitive power transfer. The circuit working principle is analyzed using fundamental harmonics approximation method and superposition theorem. The analytical expressions of the resonance relationships and system output power are provided. A prototype is constructed to validate the proposed LCLC compensation circuit. The experiment results show that the CPT system can achieve 2.4 kW power transfer through an air-gap distance of 150 mm with a dc-dc efficiency of 90.8%. It also shows good misalignment performance and robustness to air-gap distance variations.

The LCLC compensation circuit is also compared in detail with the LC compensation, and the LCLC compensation has two advantages. First, the output power of an LCLC-compensated system is proportional with the mutual coupling capacitance, which is more convenient to design circuit parameters. Second, the LCLC compensation provides the flexibility to design circuit parameters, which can realize relatively higher coupling coefficient. Therefore, the LCLC compensation can achieve a higher efficiency than the LC compensation.

2.8. References

[1] A. Sepahvand, A. Kumar, K. Afridi, D. Maksimovic, "High Power Transfer Density and High Efficiency 100 MHz Capacitive Wireless Power Transfer System," *Proc. IEEE Workshop on Con. and Mod. Power Electron.* (*COMPEL*), pp. 1-4, Jul. 2015.

[2] D.C. Ludois, J.K. Reed, K. Hanson, "Capacitive Power Transfer for Rotor Field Current in Synchronous Machines," *IEEE Trans. Power Electron.*, vol. 27, no. 11, pp. 4638-4645, Nov. 2012.

[3] D. Rozario, N. Azeez, S. Williamson, "Comprehensive Review and Comparative Analysis of Compensation Networks for Capacitive Power Transfer Systems," *Proc. of IEEE Intern. Symp. on Ind. Electron.* (*ISIE*), 823-829, Jun. 2016.

[4] A. Kumar, S. Pervaiz, C. Chang, S. Korhummel, Z. Popvic, K. Afridi, "Investigation of Power Transfer Density Enhancement in Large Air-Gap Capacitive Wireless Power Transfer Systems," *Proc. IEEE Wireless Power Trans. Conf.* (*WPTC*), pp. 1-4, May. 2015.

[5] M.P. Theodoridis, "Effective Capacitive Power Transfer," *IEEE Trans. Power Electron.*, vol. 27, no. 12, pp. 4906-4913, Dec. 2012.

[6] L. Huang, A.P. Hu, A. Swain, Y. Su, "Z-Impedance Compensation for Wireless Power Transfer Based on

Electric Field," *IEEE Trans. Power Electron.*, vol. 31, no. 11, pp. 7556-7563, Nov. 2016.

[7] M. Kusunoki, D. Obara, M. Masuda, "Wireless Power Transfer via Electric Field Resonance Coupling," *Proc. Asia-Pacific Micro. Conf.* (*APMC*), pp. 1360-1362, Nov. 2014.

[8] I. Ramos, K. Afridi, J. Estrada, Z. Popvic, "Near-field Capacitive Wireless Power Transfer Array with External Field Cancellation," *Proc. IEEE Wireless Power Trans. Conf.* (*WPTC*), pp. 1-4, May. 2016.

[9] H. Zhang, F. Lu, H. Hofmann, C. Mi, "A Loosely Coupled Capacitive Power Transfer System with LC Compensation Circuit Topology," *Proc. IEEE Energy Convers. Congr. Expo. (ECCE)*, pp. 1-5, Sept. 2016.

[10] F. Lu, H. Zhang, H. Hofmann, C. Mi, "A Double-Sided LC-Compensation Circuit for Loosely Coupled Capacitive Power Transfer," *IEEE Trans. Power Electron.*, 2017, doi: 10.1109/TPEL.2017.2674688.

[11] F. Lu, H. Zhang, H. Hofmann, C. Mi, "A Double-sided LCLC-Compensated Capacitive Power Transfer System for Electric Vehicle Charging," *IEEE Trans. Power Electron.*, vol. 30, no. 11, pp. 6011-6014, Nov. 2015.

[12] S. Li, Z. Liu, H. Zhao, Li. Zhu, Z. Chen, "Wireless Power Transfer by Electric Field Resonance and Its Application in Dynamic Charging," *IEEE Trans. Ind. Electron.*, vol. 63, no. 10, pp. 6602- 6612, Oct. 2016.

[13] H. Nishiyama, M. Nakamura, "Form and Capacitance of Parallel-Plate Capacitor", *IEEE Trans. Compen. Packag. Munufact. Tech.–Part A*, vol 17, pp. 477-484, 1994.

[14] J. Deng, F. Lu, S. Li, T. Nguyen, C. Mi, "Development of a High Efficiency Primary Side Controlled 7 kW Wireless Power Charger," *Proc. of IEEE Intern. Electric Veh. Conf.*, (*IEVC*), pp. 1-6, Dec. 2014.

[15] C. Liu, A.P. Hu, N.C. Nair, G.A. Covic, "2-D Alignment Analysis of Capacitively Coupled Contactless Power Transfer Systems," *Proc. IEEE Energy Convers. Congr. Expo. (ECCE)*, pp. 652-657, Sept. 2010.

[16] F. Lu, H. Zhang, H. Hofmann, C. Mi, "A CLLC-Compensated High Power and Large Air-Gap Capacitive Power Transfer System for Electric Vehicle Charging Applications," *Proc. IEEE Appl. Power Electr. Conf. (APEC)*, pp. 1721-1725, 2016.

[17] F. Lu, H. Zhang, H. Hofmann, C. Mi, "A High Efficiency 3.3kW Loosely-Coupled Wireless Power Transfer System without Magnetic Material," *Proc. IEEE Energy Convers. Congr. Expo. (ECCE)*, pp. 2282-2286, 2015.

[18] S. Li, W. Li, J. Deng, T.D. Nguyen, C.C. Mi, "A Double Sided LCC Compensation Network and Its Tuning Method for Wireless Power Transfer," *IEEE Trans. Veh. Techn.*, vol. 64, no. 6, pp. 2261-2273, Jun. 2015.

CHAPTER III

IPT AND CPT COMBINED SYSTEM

3.1. Introduction

Inductive power transfer (IPT) [1] and capacitive power transfer (CPT) [2] technologies can both be used in electric vehicle charging applications, in which the IPT system utilizes magnetic fields and the CPT system adopts electric fields.

The IPT technology has been well studied in previous research and is ready to be widely applied in practical systems [3]. Typically, an IPT system consists of a pair of loosely-coupled planar coils as a power transmitter and a receiver. In vehicle charging applications, the air-gap distance is large, usually resulting in an inductive coupling coefficient lower than 0.30. Therefore, compensation circuits are required to resonate with the coils and provide high voltages and currents to transfer high power. With different compensation topologies, such as series-series (SS) [4], [5] and LCC circuits [6], [7], the IPT system can achieve a dc-dc efficiency of 96% at several kW output power. In the market place, there are currently commercial products available for electric vehicle manufacturers.

Compared to IPT technology, the CPT counterpart has not been well studied and exploited. Usually, metal plates are used to make the capacitive coupler [8], forming capacitors for power flow. In vehicle charging applications with a large air-gap distance, the coupling capacitances are extremely small, which introduces difficulties to realizing high-power transfer. To overcome the limitations, an LCLC compensation circuit [9] was first attempted to realize a high-power and long-distance CPT system. However, the efficiency of the proposed CPT system is only 90.8%, which is lower than the efficiency of existing IPT systems [10]. This is because the small

coupling capacitance in a CPT system usually means a small capacitive coupling coefficient, which reduces the system efficiency [11], [12].

Considering the compensation circuits of IPT and CPT systems, it is interesting to combine the IPT and CPT systems together to achieve inductive and capacitive power transfer simultaneously [13]. The coils in an IPT system can work as compensation inductors for a CPT system, and the plates in a CPT system can work as compensation capacitors for an IPT system. Since there are two couplers in a single system, the output power is therefore increased. With the help of IPT technology, the application of CPT technology can be promoted.

In this chapter, an inductive and capacitive combined system is designed for electric vehicle charging applications. Two coils without magnetic materials are used as an inductive coupler, and four vertical-arranged metal plates are used a capacitive coupler. Circuit models of the couplers are provided to analyze the circuit working principle, in which the two couplers resonate with each other. Considering the LCC circuit in an IPT system and the LCLC circuit in a CPT system, an LC compensation circuit is proposed in the IPT and CPT combined system, in which the compensation parameters provides the flexibility to regulate the system power.

A prototype of an IPT and CPT combined system is implemented to verify the proposed design. The power flows of the inductive and capacitive couplers are balanced that the capacitive coupler contributes about one third of the total power. In experiments, the combined system realizes 2.84 kW power transfer with an efficiency of 94.5% across an air-gap distance of 150mm, and it also shows good misalignment performance.

3.2. Inductive and Capacitive Coupler Design

3.2.1 Inductive Coupler Design

A. Coil Structure

The switching frequency f_{sw} needs to be specified at the beginning of the inductive coupler design. In reference [14], magnetic materials are used in an LCC-compensated IPT system, and the switching frequency is 96 kHz. In reference [15], magnetic materials are eliminated to

mitigate the magnetic losses, and the switching frequency is 1 MHz. Although there are high-frequency magnetic materials that operate up to the MHz level, their magnetic losses are usually not acceptable in high-power applications. Considering the coupling capacitance in a long-distance CPT system is in the tens of pF range, the switching frequency of our CPT system is chosen to be 1 MHz [9]. Since the IPT and CPT systems are combined together into a single system, they will share the same switching frequency.

The structure and dimensions of an inductive coupler are shown in Fig. 3-1. It only contains two coils. Magnetic materials and aluminum shielding plates are not considered in this design in order to achieve high frequency operation.

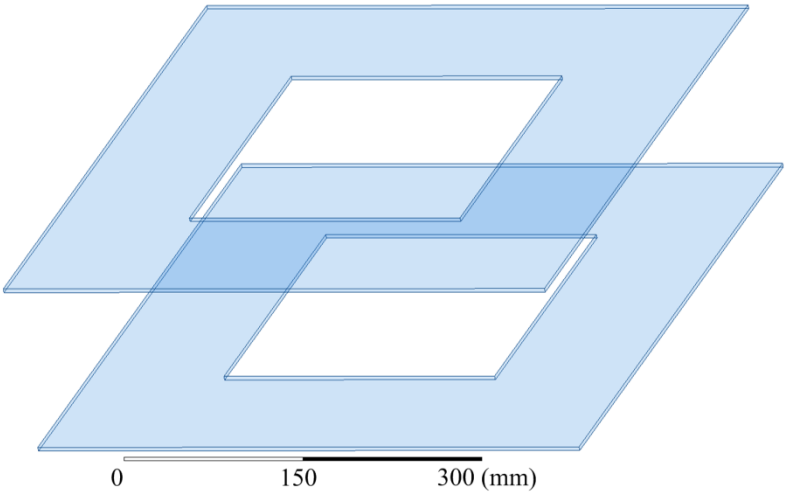

(a) 3-D view

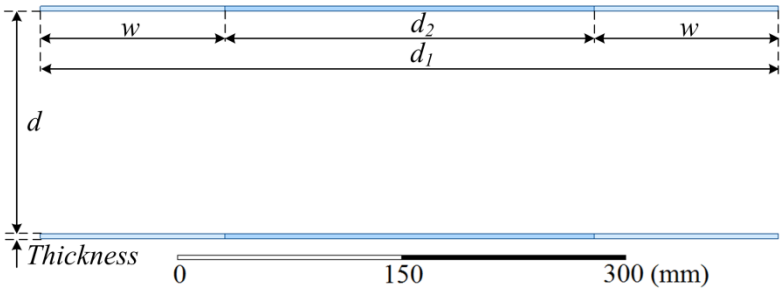

(b) Front view

Fig. 3-1. Structure and dimensions of an inductive coupler

Fig. 3-1(a) shows the 3D view of an inductive coupler, where the coil shape is designed to be square to simplify the design process. Fig. 3-1(b) shows the front view of the coils, where d_1

is the outer length of the coil, d_2 is the inner length, w is the coil width, and d is the air-gap distance. The air-gap d is set to be 150mm for vehicle charging application. The coil width ratio is further defined as $r_w=w/d_1$. The coil thickness has little effect on the inductive coupling coefficient and is defined by the Litz-wire diameter. In this design, considering the available Litz-wire, the coil thickness is set to be 3.2 mm.

B. Coil dimensions Design

As shown in Fig. 3-1, the coil structure is symmetric from the primary to the secondary. As a result, there are only two independent parameters to be determined in this design: the outer length d_1, and the coil width ratio r_w. The circuit model of coils is similar to a conventional transformer, including the self-inductance L_s and the inductive coupling coefficient k. Maxwell is used to simulate these two parameters for different dimensions. When the outer length d_1 and the coil width ratio r_w vary, the simulated k and L_s are shown in Fig. 3-2 (a) and (b), respectively.

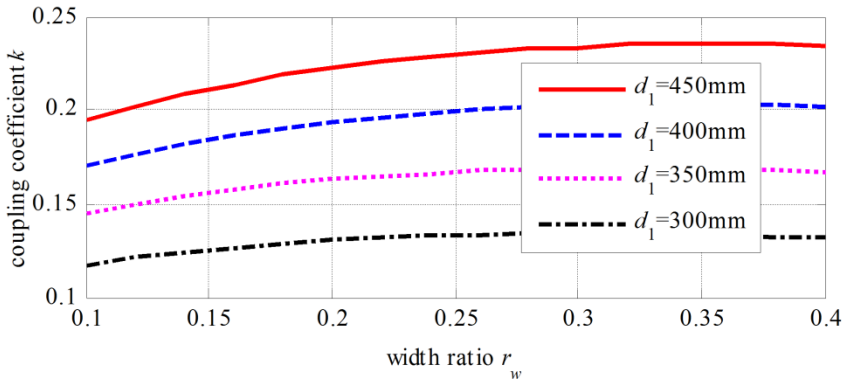

(a) Inductive coupling coefficient k

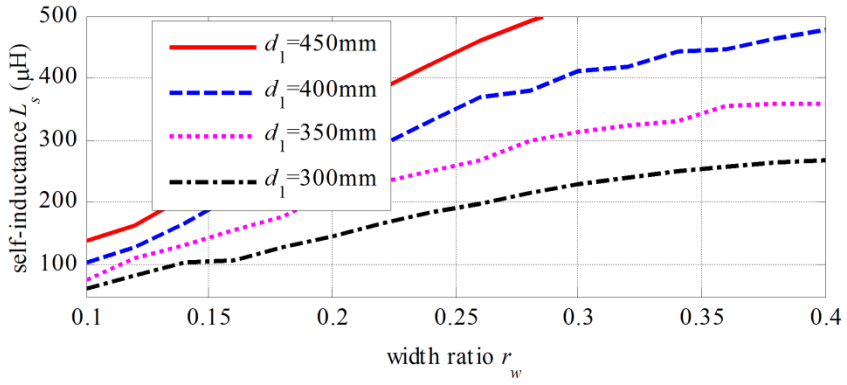

(b) Self-inductance L_s

Fig. 3-2. Maxwell-simulated equivalent parameters of an inductive coupler at different dimensions

Fig. 3-2(a) shows that the inductive coupling coefficient k is mainly determined by the outer length d_1. The width ratio r_w only has slight influence on k. Fig. 3-2(b) shows that the self-inductance L_s increases with increasing d_1 and r_w. In a practical inductive coupler, Litz-wires is used to wind the coils, and there is parasitic capacitance between adjacent turns. Larger inductance means more turns are used and the corresponding parasitic capacitance is also larger. The self-resonant frequency of the coils can then be close to the switching frequency, causing undesired inductance variation. Therefore, in this design, the self-inductance of the coil should be limited. The inductive coupler is expected to resonate with the capacitive coupler, and the finalization of their dimensions should be considered together.

3.2.2 Capacitive Coupler Design

A. Coupler Structure

Four pieces of metal plates are used to form coupling capacitors and generate electric fields to transfer power. The structure and dimensions of the capacitive coupler are shown in Fig. 3-3. Different than the previous horizontal plates in Chapter II, the four plates are vertically arranged to save space [16]. Since the plate structure is more compact, all the capacitive couplings between plates should be considered in the coupler. The four plates are separated by the air gap into two pairs. At each side, the two plates have different sizes to maintain the coupling between the primary and secondary. The larger plates are placed at the outer side, and the smaller plates are placed at the inner side. The air gap distance is therefore between the two inner plates.

Fig. 3-3(a) shows the 3D view of the vertically arranged capacitive coupler. The plates P_1 and P_2 are on the primary side to form the transmitter, and the plates P_3 and P_4 are on the secondary side to form the receiver. Fig. 3-3(b) shows the front view of the capacitive coupler, where l_1 is the length of the outer plate, l_2 is the length of the inner plate, d_c is the distance between the inner and output plate, and d is the air-gap distance. Each plate is designed to be square and the plates are symmetric from the primary to secondary side to simplify the dimension design. The air-gap distance is the same with the inductive coupler, which is 150 mm. The thickness of the plates is 2 mm.

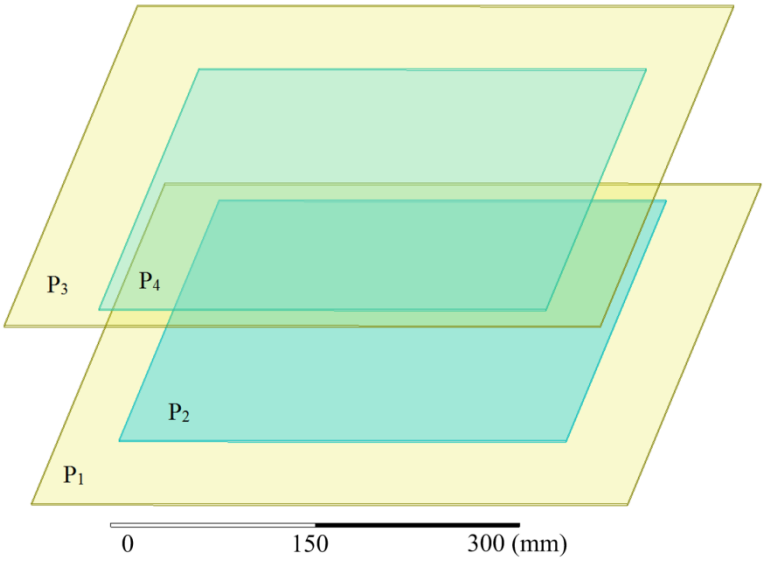

(a) 3-D view

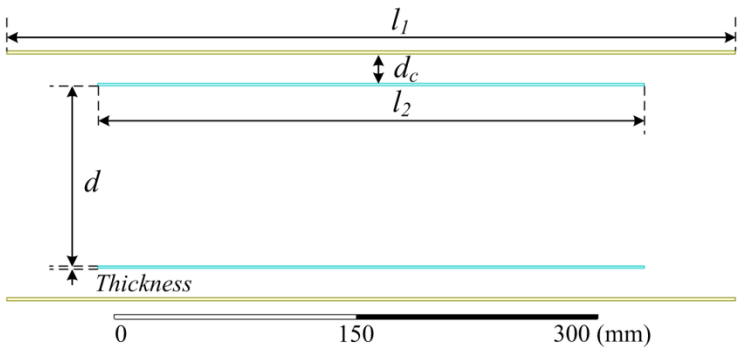

(b) Front view

Fig. 3-3. Structure and dimensions of a vertically arranged capacitive coupler

B. Circuit Model

There exists coupling capacitance between every two plates in the coupler, resulting in six mutual capacitances C_{12}, C_{13}, C_{14}, C_{23}, C_{24}, and C_{34}, as shown in Fig. 3-4(a). Because of the fringing effect of electric fields, the cross-coupling capacitances C_{14} and C_{23} are significant and should not be neglected, especially in misalignment cases. However, the capacitances C_{14} and C_{23} increase the complexity of the circuit model and induce difficulties when analyzing the behavior of the capacitive coupler. Therefore, it is helpful to further simplify the original six-capacitance model to a four-capacitance equivalent model, as shown in Fig. 3-4(b). The simplified four-capacitance model can be directly used in the circuit analysis of a CPT system.

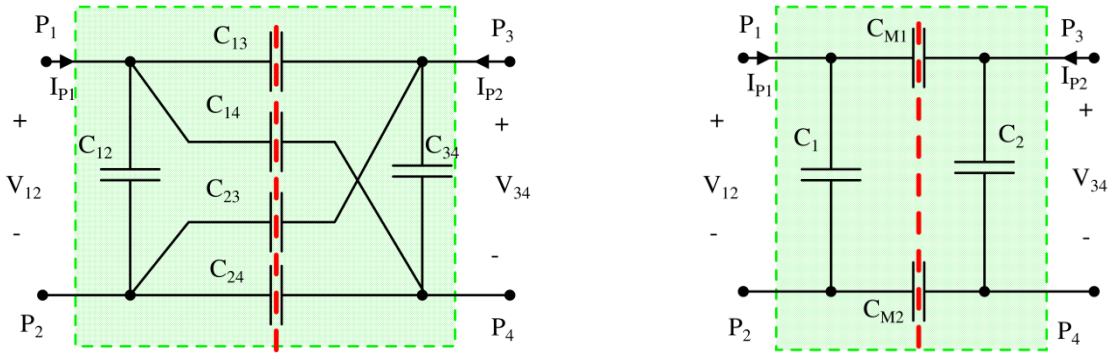

(a) Six-capacitance model (b) Four-capacitance model

Fig. 3-4. Circuit model of a vertically arranged capacitive coupler

It is necessary to derive the relationship between parameters in the six- and four-capacitance models. When the coupler is connected in a circuit, capacitances C_{M1} and C_{M2} are in series. Their equivalent capacitance is defined as C_M, which is expressed as

$$C_M = \frac{C_{M1}C_{M2}}{C_{M1}+C_{M2}} \tag{3-1}$$

In Fig. 3-4(a), the input and output voltages of the coupler are defined as V_{12} and V_{34}, and the input and output currents are defined as I_{P1} and I_{P2}. If the capacitive coupler is considered as a two-port network, the input-output relationships are expressed as follows.

$$\begin{cases} I_{P1} = j\omega_s[C_{12} + \dfrac{(C_{13}+C_{14})(C_{23}+C_{24})}{C_{13}+C_{14}+C_{23}+C_{24}}]\cdot V_{12} - j\omega_s \dfrac{C_{13}C_{24}-C_{14}C_{23}}{C_{13}+C_{14}+C_{23}+C_{24}}\cdot V_{34} \\ I_{P2} = -j\omega_s \dfrac{C_{13}C_{24}-C_{14}C_{23}}{C_{13}+C_{14}+C_{23}+C_{24}}\cdot V_{12} + j\omega_s[C_{34} + \dfrac{(C_{13}+C_{23})(C_{14}+C_{24})}{C_{13}+C_{14}+C_{23}+C_{24}}]\cdot V_{34} \end{cases} \tag{3-2}$$

In Fig.3-4(b), with the same input and output voltages and currents, the input-output relationships are expressed as

$$\begin{cases} I_{P1} = j\omega_s(C_1+C_M)\cdot V_{12} - j\omega_s C_M \cdot V_{34} \\ I_{P2} = -j\omega_s C_M \cdot V_{12} + j\omega_s(C_2+C_M)\cdot V_{34} \end{cases} \tag{3-3}$$

The six- and four-capacitance models are equivalent to each other. Therefore, comparing (3-2) and (3-3), the equivalent parameters are derived to be,

$$\begin{cases} C_M = \dfrac{C_{13}C_{24}-C_{14}C_{23}}{C_{13}+C_{14}+C_{23}+C_{24}} \\ C_1 = C_{12} + \dfrac{C_{13}C_{23}+2C_{14}C_{23}+C_{14}C_{24}}{C_{13}+C_{14}+C_{23}+C_{24}} \\ C_2 = C_{34} + \dfrac{C_{13}C_{14}+2C_{14}C_{23}+C_{23}C_{24}}{C_{13}+C_{14}+C_{23}+C_{24}} \end{cases} \tag{3-4}$$

C. *Dimension Design*

In the capacitive coupler, since the primary and secondary sides are symmetric, there are three parameters that need to be designed: outer plate length l_1, inner plate length l_2, and same side plate distance d_c. Also, the capacitances satisfy C_{12}=C_{34}, C_{14}=C_{23}, and C_1=C_2, even in misaligned cases. Due to the space limitations, l_1 is set to be 610 mm (24 in) in this design. The plate ratio is defined as r_p, which is expressed as r_p=l_2/l_1. When d_c and r_p vary, Maxwell is used to determine the capacitance through simulation. The equivalent capacitances C_M and C_1 are shown in Fig. 3-5(a) and 3-5(b), respectively.

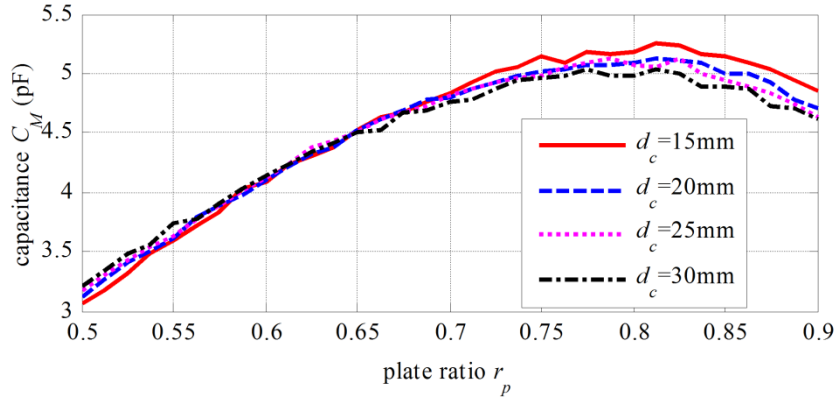

(a) Capacitance C_M

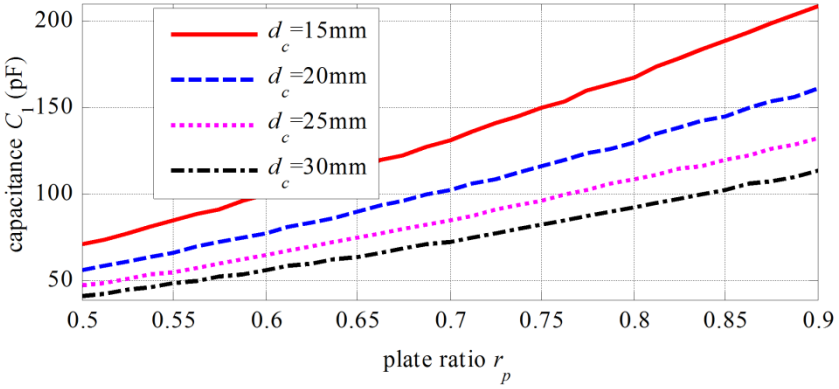

(b) Capacitance C_1

Fig. 3-5. Maxwell-simulated equivalent capacitances of a capacitive coupler at different dimensions

Fig. 3-5(a) shows that the capacitance C_M is mainly determined by the plate ratio r_p, and the plate distance d_c has little effect on C_M. Fig. 3-5(b) shows that the capacitance C_1 increases with increasing d_c and r_p. The capacitance C_M is maximized when the plate ratio r_p is in the range of

[0.75, 0.85]. In this design, r_p is selected to be 0.75 to reduce the size of the plate and hence the usage of aluminum material. Then, the plate distance d_c is the only parameter that needs to be determined. It will be considered together with the dimensions of the inductive coupler, so that the appropriate resonance between them can be achieved.

3.3. LC-Compensated IPT and CPT Combined System

3.3.1 Circuit Topology

Using the designed inductive and capacitive coupler, the circuit topology of a double-sided LC-compensated IPT and CPT combined system is shown in Fig. 3-6, which is derived from an LCC-compensated IPT system and an LCLC-compensated CPT system. The two inductors L_1 and L_2 are inductively coupled and generate magnetic fields to transfer power. The mutual inductance between them is defined as M_{12}, expressed by the self-inductances L_1, L_2, and inductive coupling coefficient k as follows:

$$M_{12} = k\sqrt{L_1 L_2} \tag{3-5}$$

The two pairs of metal plates are capacitively coupled and generate electric fields to transfer power. The four-capacitance equivalent circuit model will be used in circuit analysis. Considering the LCLC-compensation in chapter II, at each side, an inductor and a capacitor are connected with the couplers to provide a resonance, forming the LC compensation circuit.

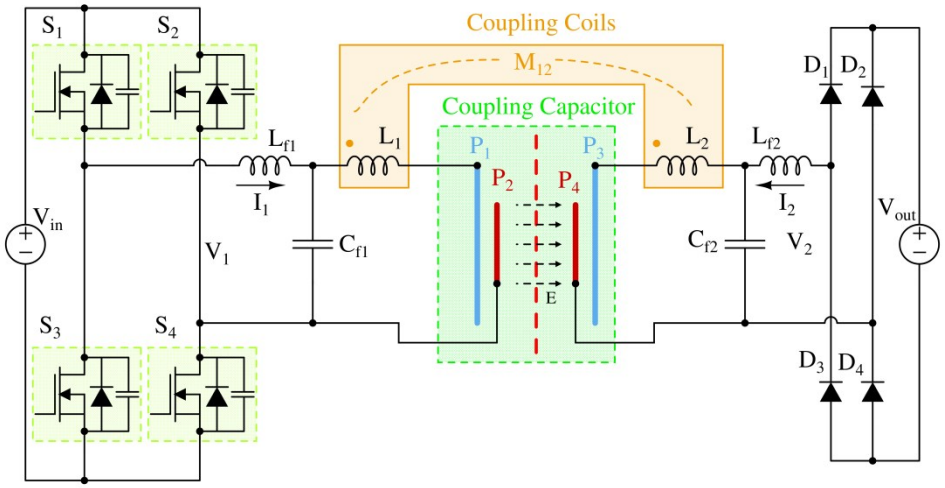

Fig. 3-6. Circuit topology of a double-sided LC-compensated IPT and CPT combined system

Similar to previous CPT systems, a full-bridge inverter is used at the front end to provide an ac excitation voltage V_1, and a full-bridge diode rectifier is used at the output side to provide dc current to the battery load.

It is important to pay attention to the coupling polarity of the inductors L_1 and L_2. The connection in Fig. 3-6 will result in both the inductive and capacitive couplings contributing to increase the system output power. If the coupling polarity of inductors is reversed, the inductive and capacitive power transfer will have opposite contributions, and the system output power could be significantly reduced. When the capacitive coupler is represented by a four-capacitor circuit model, the equivalent circuit topology of the combined system is shown in Fig. 3-7, which is used to analyze the circuit's working principle.

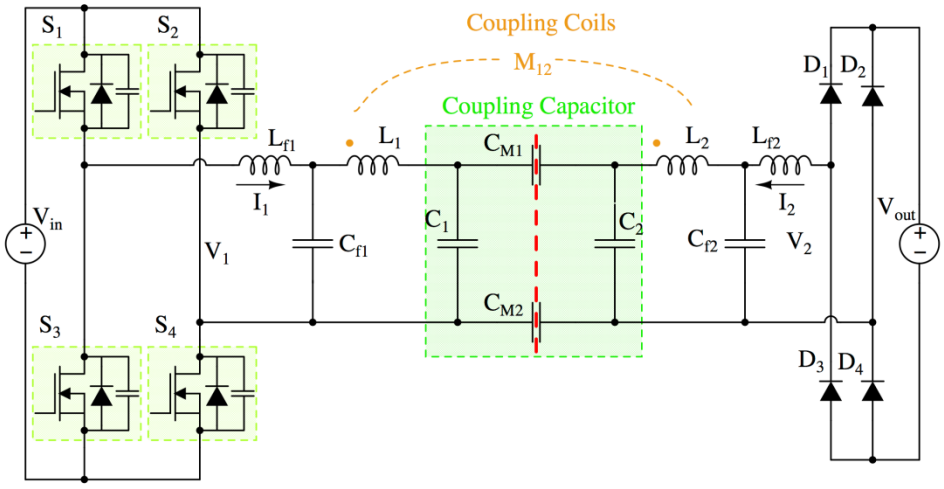

Fig. 3-7. Equivalent circuit of a double-sided LC-compensated IPT and CPT combined system

3.3.2 Circuit Working Principle

In Fig. 3-7, the input inverter generates a square wave voltage excitation V_1 at the input side, and the diode rectifier also causes a square wave voltage V_2 at the output side. The LC compensation circuits L_{f1}-C_{f1} and L_{f2}-C_{f2} behave as low-pass filters, and so the higher-order harmonics components in V_1 and V_2 can be neglected. Therefore, the fundamental harmonics approximation (FHA) method and the superposition theorem can be used to analyze the circuit working principle, as shown in Fig. 3-8.

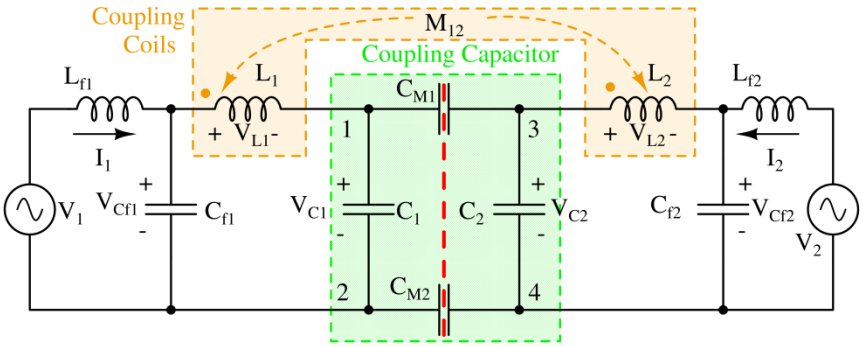

(a) Simplified resonant circuit

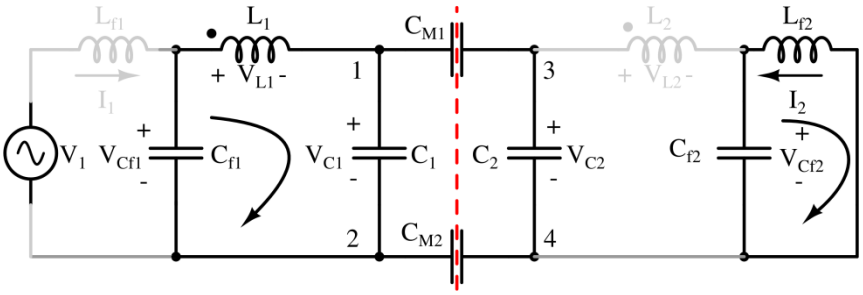

(b) Components excited by input source

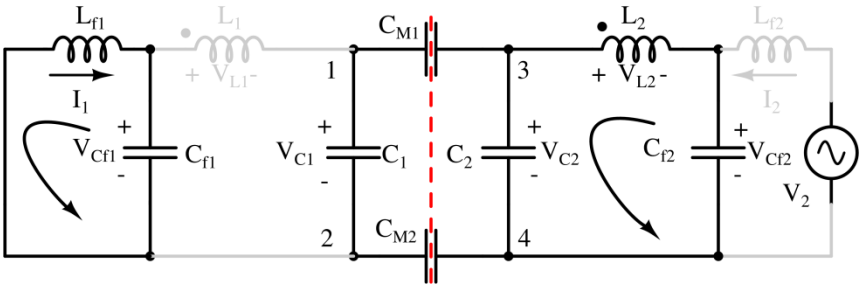

(c) Components excited by output source

Fig. 3-8. Fundamental harmonics approximation of an LC-compensated IPT and CPT combined system

Fig. 3-8(a) shows the simplified resonant circuit topology of Fig. 3-7. The input and output voltages are replaced by two sinusoidal sources. The power losses in circuit components are neglected to simplify the analysis process.

Fig. 3-8(b) shows the components excited only by the input source V_1. The parameters are designed to achieve two parallel resonances, as highlighted in the circuit. One resonance includes L_{f2} and C_{f2}, and the other resonance consists of L_1, C_{f1}, C_1, C_{M1}, C_{M2}, and C_2. If the switching frequency is equal to the resonant frequency (ω_s=ω_0) and the relationships between parameters

are the same with equation (2-4) in Chapter II of an LCLC-compensated CPT system, due to their similarity. Also, since the impedance of a parallel resonance is infinite, there is no current flowing through L_2 and L_{f1}. Therefore, the input current is independent of the input voltage

In Fig. 3-8(b), although there is no current flowing in L_2, there is voltage across it due to the inductive coupling with L_1. This voltage can help to increase the output current I_2. Meanwhile, the capacitive coupling can induce a voltage on C_2 that also contributes to the output current. The polarities of V_{L2} and V_{C2} must be considered to maximize the output power. This is the main difference between an IPT-CPT combined system with a pure IPT or CPT system.

Fig. 3-8(c) shows the components excited only by the output voltage V_2. The parameters are designed to achieve two parallel resonances as highlighted. One resonance includes L_{f1} and C_{f1}, and the other resonance contains L_2, C_{f2}, C_2, C_{M1}, C_{M2}, and C_1. The parameters also satisfy equation (2-5) at the frequency ω_0. Because of the infinite impedances of parallel resonances, there is no current in L_1 and L_{f2}, and so the output current does not depend on the output voltage at the resonant frequency. Therefore, the designed resonant circuit behaves as a current source for both the input and output.

In Fig. 3-8(c), the inductive coupling induces a voltage on L_1, and the capacitive coupling generates a voltage on C_1. The voltages V_{L1} and V_{C1} both contribute to the input current I_1, and so realizes inductive and capacitive power transfer simultaneously.

3.3.3 System Power Calculation

In Fig. 3-8(b), the voltage on C_{f1} is the input voltage, which means $V_{Cf1}=V_1$. The current on L_1 is therefore expressed as,

$$I_{L1} = -j\omega_0 C_{f1} V_1 \tag{3-6}$$

Considering the mutual inductance M_{12} in (3-5), the induced voltage on L_2 is expressed as,

$$V_{L2} = j\omega_0 M_{12} I_{L1} = \omega_0^2 M_{12} C_{f1} V_1 \tag{3-7}$$

Similar to the LCLC-compensated CPT system, the voltage on C_2 is calculated as,

$$V_{C2} = -\frac{C_M \cdot C_{f1}}{C_1 C_2 + C_1 C_M + C_2 C_M} \cdot V_1 \tag{3-8}$$

Then, the voltage on C_{f2} is expressed as,

$$V_{Cf2} = V_{C2} - V_{L2} = -\frac{C_M \cdot C_{f1}}{C_1C_2 + C_1C_M + C_2C_M} \cdot V_1 - \omega_0^2 M_{12} C_{f1} V_1 \tag{3-9}$$

The output current ($-I_2$) is further determined to be,

$$-I_2 = -j\omega_0 C_{f2} V_{Cf2} = \frac{j\omega_0 C_M \cdot C_{f1} C_{f2}}{C_1C_2 + C_1C_M + C_2C_M} \cdot V_1 + j\omega_0^3 M_{12} C_{f1} C_{f2} V_1 \tag{3-10}$$

In Fig. 3-8(c), the voltage on C_{f2} is equal to V_2, which means $V_{Cf2}=V_2$. Then, the current in L_2 is expressed as,

$$I_{L2} = j\omega_0 C_{f2} V_2 \tag{3-11}$$

The voltage on L_1 induced by the inductive coupling is therefore expressed as,

$$V_{L1} = j\omega_0 M_{12} I_{L2} = -\omega_0^2 M_{12} C_{f2} V_2 \tag{3-12}$$

The voltage on C_1 is calculated according to the capacitive coupling, which is expressed as,

$$V_{C1} = -\frac{C_M C_{f2}}{C_1C_2 + C_1C_M + C_2C_M} \cdot V_2 \tag{3-13}$$

Then, the voltage on C_{f1} is expressed as,

$$V_{Cf1} = V_{C1} + V_{L1} = -\frac{C_M \cdot C_{f2}}{C_1C_2 + C_1C_M + C_2C_M} \cdot V_2 - \omega_0^2 M_{12} C_{f2} V_2 \tag{3-14}$$

The input current I_1 is calculated as,

$$I_1 = j\omega_0 V_{Cf1} = -\frac{j\omega_0 C_M \cdot C_{f1} C_{f2}}{C_1C_2 + C_1C_M + C_2C_M} \cdot V_2 - j\omega_0^3 M_{12} C_{f1} C_{f2} V_2 \tag{3-15}$$

Considering the parallel resonances of L_{f1}-C_{f1} and L_{f2}-C_{f2} in the circuit, the input and output currents are simplified as follows:

$$\begin{cases} I_1 = -\dfrac{j\omega_0 C_M \cdot C_{f1} C_{f2}}{C_1C_2 + C_1C_M + C_2C_M} \cdot V_2 - j\dfrac{M_{12}}{\omega_0 L_{f1} L_{f2}} V_2 \\ -I_2 = \dfrac{j\omega_0 C_M \cdot C_{f1} C_{f2}}{C_1C_2 + C_1C_M + C_2C_M} \cdot V_1 + j\dfrac{M_{12}}{\omega_0 L_{f1} L_{f2}} V_1 \end{cases} \tag{3-16}$$

Since an uncontrolled diode rectifier is used at the output side, the output current ($-I_2$) must be in phase with the output voltage V_2 when the output current is continuous. According to the phase angle in (3-16), it can be determined that the input voltage V_1 is also in phase with the input current I_1, which means unity power factor is achieved at the input side. The system power is then given by,

$$P_{in} = P_{out} = \frac{\omega_0 C_M \cdot C_{f1} C_{f2}}{C_1 C_2 + C_1 C_M + C_2 C_M} \cdot |V_1| \cdot |V_2| + \frac{M_{12}}{\omega_0 L_{f1} L_{f2}} \cdot |V_1| \cdot |V_2| \tag{3-17}$$

This shows that the input and output power are equal to each other, which is consistent with the previous assumption of neglecting component losses. The output power of the IPT-CPT combined system is therefore equal to the sum of output powers in an LCC-compensated IPT system and an LCLC-compensated CPT system. The inductive power P_{IPT} and capacitive power P_{CPT} are further given as,

$$\begin{cases} P_{IPT} = \dfrac{M_{12}}{\omega_0 L_{f1} L_{f2}} \cdot |V_1| \cdot |V_2| \\ P_{CPT} = \dfrac{\omega_0 C_M \cdot C_{f1} C_{f2}}{C_1 C_2 + C_1 C_M + C_2 C_M} \cdot |V_1| \cdot |V_2| \end{cases} \tag{3-18}$$

3.4. Design Example of an LC-Compensated IPT and CPT Combined System

3.4.1 Power Ratio of IPT and CPT Systems

This combined system utilizes both inductive and capacitive couplings to transfer power. In a practical design, it is important to determine the power ratio between the two couplings, which is the percentage of their contributions. In the coupler structure design, since the inductive and capacitive couplers have similar physical size, they can be designed to transfer comparable power to the load. The power ratio is defined as $r_{I\text{-}C}$, which is expressed as,

$$r_{I-C} = \frac{P_{IPT}}{P_{CPT}} = \frac{M_{12}}{\omega_0 L_{f1} L_{f2}} \cdot \frac{C_1 C_2 + C_1 C_M + C_2 C_M}{\omega_0 C_M \cdot C_{f1} C_{f2}} \tag{3-19}$$

Considering the resonances between parameters, the power ratio is simplified as,

$$r_{I-C} = \frac{P_{IPT}}{P_{CPT}} = \frac{\omega_0^2 k \sqrt{L_1 L_2} \cdot (C_1 C_2 + C_1 C_M + C_2 C_M)}{C_M} \tag{3-20}$$

If the capacitive coupling coefficient k_C is defined as,

$$k_C = \frac{C_M}{\sqrt{(C_1 + C_M) \cdot (C_2 + C_M)}} \tag{3-21}$$

The power ratio $r_{I\text{-}C}$ is further simplified as,

$$r_{I-C} = k \cdot \frac{\sqrt{(C_1 + C_M)(C_2 + C_M)}}{C_M} \cdot \omega_0^2 \sqrt{L_1 L_2} \cdot \frac{C_1 C_2 + C_1 C_M + C_2 C_M}{\sqrt{(C_1 + C_M)(C_2 + C_M)}} \tag{3-22}$$

Referring to the resonances in (2-4) and (2-5), it is further simplified as,

$$r_{I-C} = \frac{k}{k_C} \cdot \sqrt{1 + \frac{C_1 + C_M}{C_{f1}}(1 - k_C^2)} \cdot \sqrt{1 + \frac{C_2 + C_M}{C_{f2}}(1 - k_C^2)} \tag{3-23}$$

In a CPT system, it is typical that C_{f1}>>C_1, C_1>>C_M, C_{f2}>>C_2, and C_2>>C_M. Therefore, the power ratio is approximated to be

$$r_{I-C} = \frac{P_{IPT}}{P_{CPT}} \approx \frac{k}{k_C} \tag{3-24}$$

This shows that the power ratio of inductive and capacitive power is approximately the ratio of the inductive and capacitive coupling coefficients k and k_C. In the previous inductive coupler dimensions design, Fig. 3-2 shows that the inductive coupling coefficient k varies between 0.12 and 0.23. In the capacitive coupler dimension design, Fig. 3-5 shows that the varying range of capacitive coupling coefficient is about from 0.04 to 0.10. Therefore, using the designed couplers, the IPT system contributes more to the output power than the CPT system. In the system parameter design, the capacitive power should be significant compared to the inductive power..

3.4.2. System Parameters Design

The dimensions of the inductive and capacitive couplers need to be determined first. In the inductive coupler, the coil outer length d_1 is selected to be 300 mm for this design, and the corresponding inductive coupling coefficient k is about 0.130. In the capacitive coupler, the mutual capacitance C_M is about 5.0 pF, and the varying of plate distance d_c can change the capacitance C_1 and the corresponding k_C.

As an example, the system input power is designed to be 3.0 kW, the switching frequency is 1 MHz, the input dc voltage is 310V, and the output dc voltage is 320V. Since the structures of inductive and capacitive couplers are symmetric from the primary to secondary sides, the circuit parameters are also designed to be symmetric to simplify design, which means L_{f1}=L_{f2} and C_{f1}=C_{f2}. According to the power equation (3-17) and the power ratio in (3-23), the relationship between the capacitance C_1 and the power ratio is shown in Fig. 3-9(a). Meanwhile, according to the resonance expressions of (2-4) and (2-5) in chapter II, the corresponding self-inductance L_1 of the coupling coil is shown in Fig. 3-9(b).

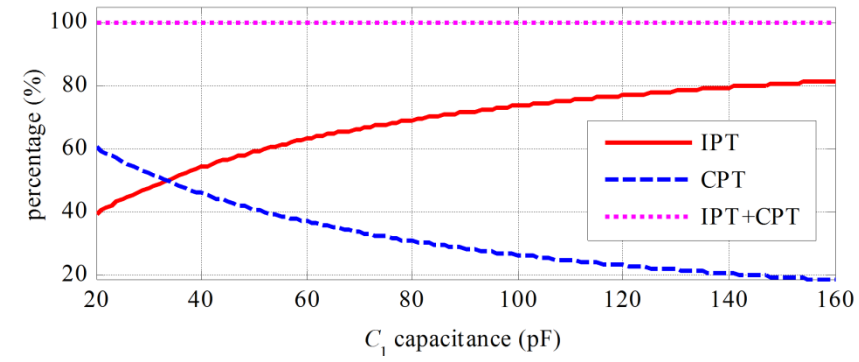

(a) IPT and CPT power contribution

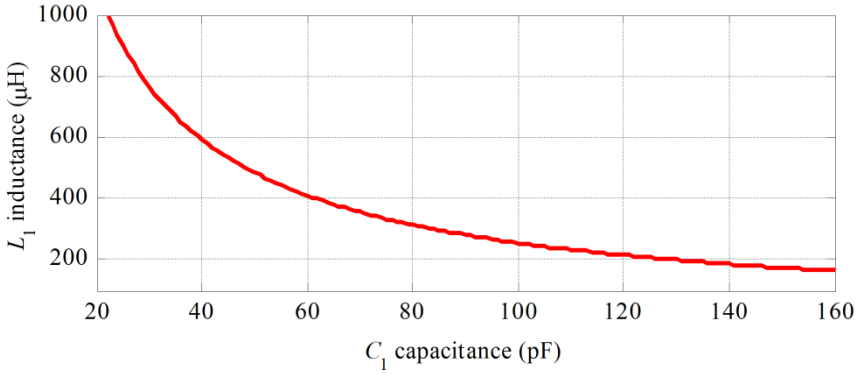

(b) Inductance L_1

Fig. 3-9. Relationship of circuit parameters in an IPT and CPT combined system

In Fig. 3-9(a), the total power of the IPT and CPT systems is fixed at 3.0 kW. When the capacitance C_1 varies, the power distribution between the two systems also changes. The calculation shows that the contribution of the CPT system decreases with increasing C_1. Fig. 3-9(b) shows that the self-inductance L_1 also decreases with an increasing C_1.

In this design, the same-side plate distance d_c is selected to be 25 mm. Fig. 3-5(b) shows that the capacitance C_1 is 96.1 pF and the capacitive coupling coefficient k_C is 0.052. Then, Fig. 3-9(a) indicates that the IPT system provides 72% (2160 W) of the total power and the CPT system provide the remaining 28% (840 W), resulting in a power ratio $r_{I\text{-}C}$ of 2.57. In Fig. 3-9(b), the self-inductance L_1 is calculated to be 264.1 μH. From Fig. 3-2, the coil width ratio r_w=0.35, the coil width is 105mm, and the inner coil length d_2 is 90 mm. The resulting system design specifications and circuit parameters are shown in Table III-1. Most of the parameters are symmetric, except that the inductor L_1 is about 7% smaller than L_2 to provide soft-switching conditions to the MOSFETs of the input inverter.

Table III-1. System parameters of a 3.0kW IPT and CPT combined system

Parameter	Design Value	Parameter	Design Value
V_{in}	310 V	V_{out}	320 V
P_{IPT}	2160W (72%)	P_{CPT}	840W (28%)
d_1	300 mm	l_1	610 mm
d_2	90 mm	l_2	457 mm
D	150 mm	d_c	25 mm
W	105 mm	f_{sw}	1 MHz
r_w	0.35	r_p	0.75
K	0.130	k_c	0.052
$L_{f1}(L_{f2})$	14.2 μH	C_M	5.0 pF
L_1	256.2 μH	C_{f1} (C_{f2})	1.78 nF
L_2	264.1 μH	C_1 (C_2)	96.1 pF

3.4.3. System Simulation

With the dimensions in Table III-1, FEA analysis of the inductive and capacitive couplers is conducted at different misalignment conditions. The normalized values of mutual capacitance C_M and inductive coupling coefficient k at different misalignments are shown in Fig. 3-10.

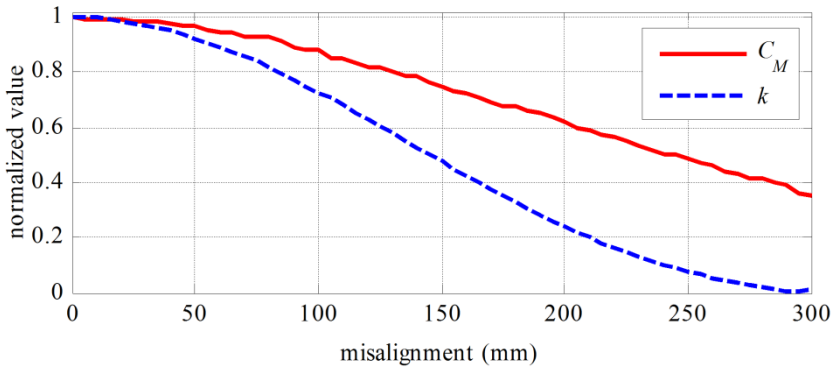

Fig. 3-10. Maxwell-simulated normalized C_M and k at different misalignments

In the capacitive coupler, Maxwell simulation shows that the variations of the large capacitances C_1 and C_2 are within 3% of their well-aligned values, when there is 300 mm

misalignment. Then, only the variation of the relatively small mutual capacitance C_M needs to be considered. Fig. 3-10 shows that C_M reduces to 62.1% of the well-aligned value with 200 mm misalignment, and 38.5% of the well-aligned value with 300 mm misalignment.

In the inductive coupler, the variations of the large self-inductance L_1 and L_2 are within 2% of their well-aligned values, when there is 300 mm misalignment. Only the inductive coupling coefficient k needs to be considered. Fig. 3-10 shows that k reduces to 25.2% of the well-aligned value with 200mm misalignment, and almost zero with 300 mm misalignment, which shows that the capacitive coupler has better misalignment performance than the inductive coupler.

Using the circuit parameters in Table III-1, the circuit performance is simulated by LTspice. The input and output waveforms of the voltages and currents are shown in Fig. 3-11.

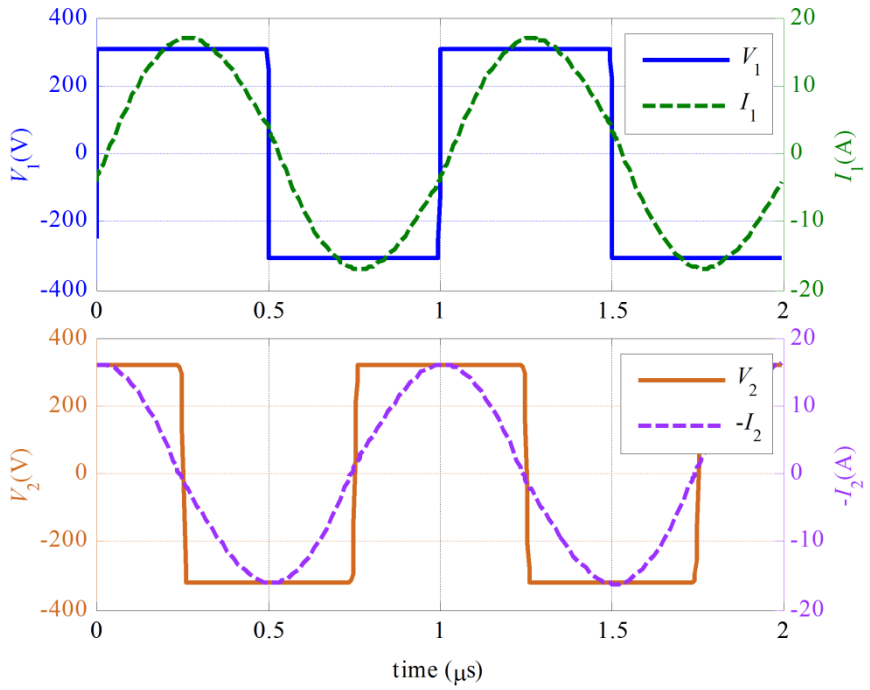

Fig. 3-11. LTspice-simulated waveforms of an LC-compensated IPT and CPT combined system

Fig. 3-11 shows that the voltages and currents are almost in phase with each other at both the input and output sides, which is consistent with the circuit analysis. Also, the cut-off current of the switching transient is about 3A, resulting in soft-switching behaviors.

3.5. Experimental Results

3.5.1. Experimental setup

Using the parameters in Table III-1, a prototype of an LC-compensated IPT and CPT combined system is constructed as shown in Fig. 3-12. There are two couplers in the system, an inductive coupler and a capacitive coupler.

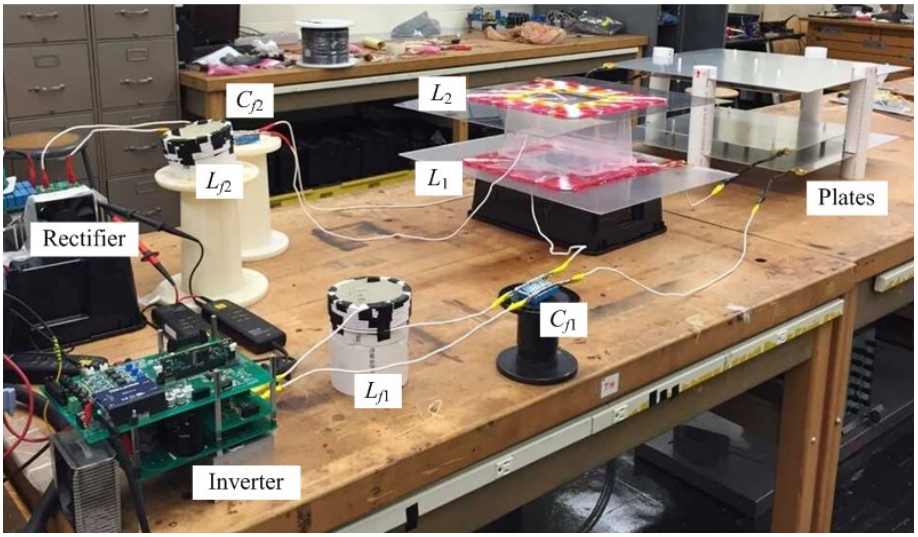

Fig. 3-12. Experimental prototype of an IPT and CPT combined system

The inductive coupler consists of two coils made by 3000 strands of AWG 46 Litz-wire to eliminate skin effect losses. The compensation inductors L_{f1} and L_{f2} are also made from the same Litz-wire. The inductors are wound on PVC tubes and there is no magnetic material used in either the inductive coupler or the inductors, in order to mitigate the magnetic losses.

The capacitive coupler contains four vertically arranged aluminum plates. Ceramic spacers are used between the adjacent plates as insulation. The plates are directly connected to the coils, and the polarity of connection follows Fig. 3-6. For simplicity, the connection is at the edge of the plates. High frequency film capacitors are used in the setup for the compensation capacitors.

In the prototype, the distance between the inductive and capacitive coupler is 300 mm in order to reduce the influence between them. If the two couplers are placed close to each other, it can induce some drawbacks. First, the short distance can induce capacitive couplings between the plates and coils, and the equivalent capacitances in the capacitive coupler are changed by the proximity of coils. As a result, the resonance in the circuit is disturbed. Second, the magnetic

fields of the coils can generate eddy current losses in the metal plates, which can reduce the coil inductance and the system efficiency. However, significant distance between the two couplers can decrease the power density of the combined system. In future research, the two couplers can be integrated as a single coupler to increase the system power density [17].

Since the switching frequency is as high as 1 MHz, SiC carbide MOSFETs (C2M0080120D) and diodes (IDW30G65C5) are used in the inverter and rectifier to provide high-frequency switching capability.

3.5.2. Well-Aligned Experiment

Experiments are conducted with the designed prototype. The input dc source voltage is 310V, and the electronic dc load is tuned to a constant 320V in order to emulate a battery pack. The experimental power and waveforms of the well-aligned case are shown in Fig. 3-13.

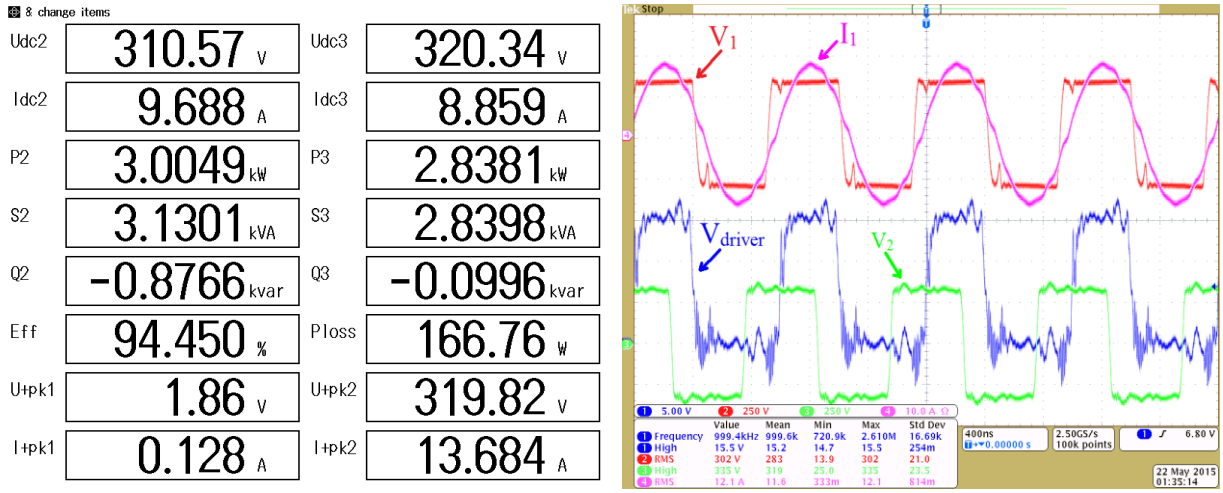

(a) power (b) waveforms

Fig. 3-13. Experimental results of an IPT and CPT combined system at well-aligned position

At well-aligned and the nominal input and output voltage condition, Fig. 3-13(a) shows that the system input power is 3.0 kW, output power reaches 2.84 kW, the total power loss is 166.7 W, and the dc-dc efficiency is 94.45%.

Fig. 3-13(b) shows the input and output waveforms of the voltages and currents. It shows that the input voltage and current are almost in phase. The current I_1 is slightly lagging the

voltage V_1 to enable soft-switching of the MOSFETs. At the switching transient, V_1 smoothly increases or decreases with a small spike, which corresponds to some switching losses. Since the spike voltage is within 50V, the induced switching losses are acceptable in this system.

3.5.2. Misalignment Experiment

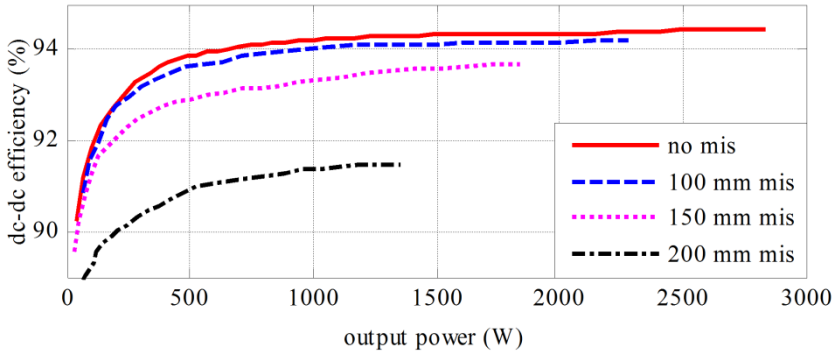

(a) IPT+CPT system

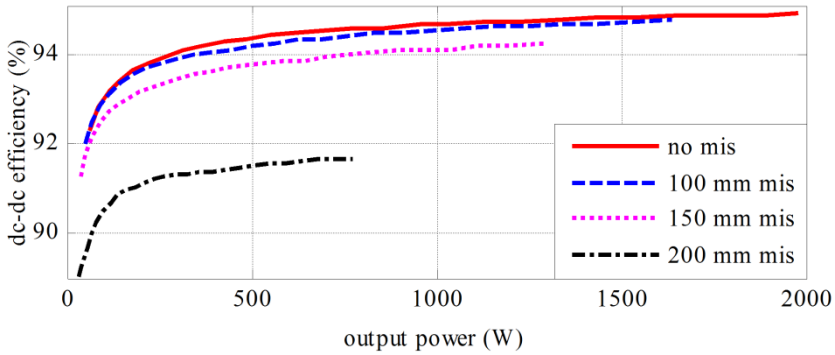

(b) Only IPT system

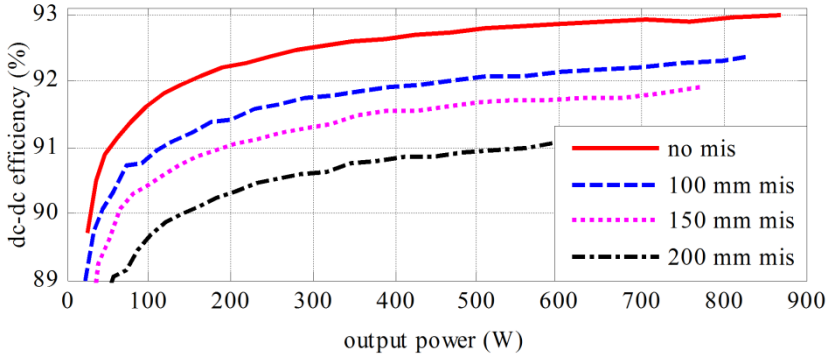

(c) Only CPT system

Fig. 3-14. Output power and efficiency of an IPT and CPT combined system

Fig. 3-14(a) shows the relationship between the output power and efficiency of an IPT-CPT

combined system. In experiments, the input and output voltages are increased by 10V as a step to their nominal values, and both the resulting power and efficiency are measured at each step. It shows that the efficiency increases with the output power. In the well-aligned case, the output power reaches 2.84 kW with an efficiency of 94.45%, as shown in Fig. 3-13(a). When there is misalignment between the transmitter and receiver, the output power and efficiency both decrease. When both the inductive and capacitive couplers have 200mm misalignment, the output power drops to 1.35 kW with a dc-dc efficiency of 91.5%.

Fig. 3-14(b) shows the output power and efficiency of the IPT system. In this case, the two pairs of plates are separated to eliminate their capacitive coupling. In this way, there is no capacitive power transferred in this system, and only the coils are used to transfer power. When the coils are well-aligned, the maximum output power is 1.95 kW with a dc-dc efficiency of 94.89%. When there is 200mm misalignment between coils, the output power drops to 0.75 kW with a dc-dc efficiency of 91.68%.

Fig. 3-14(c) shows the output power and efficiency of the CPT system. In this case, the two coils are separated to eliminate the inductive coupling. In this way, there is no inductive power transferred in this system, and only the metal plates are used to transfer power. When the plates are well-aligned, the maximum output power is 0.86 kW with a dc-dc efficiency of 93.04%. When the plates have 200mm misalignment, the output power drops to 0.69 kW with a dc-dc efficiency of 91.18%.

The output power in Fig. 3-14(a) is the sum of the power in Fig. 3-14(b) and (c), which shows that both the inductive and capacitive coupler contribute to transfer power in a combined system. It also shows that the capacitive coupler has better misalignment performance than the inductive coupler. When the misalignment increases to 200mm, the capacitive coupler can maintain 80.2% of the well-aligned power, and the inductive coupler can only realize 38.5% of its well-aligned power. Therefore, the introduction of a capacitive coupler into an IPT system can improve its misalignment performance.

3.5.3. Comparison of Modeled and Experimental Results

The experimental performance of the IPT and CPT combined system is compared to the modeled and simulated system in section 3.4. The comparisons include the waveforms of input voltage and current, the misalignment performance, and the power distribution between the IPT and CPT parts in the system.

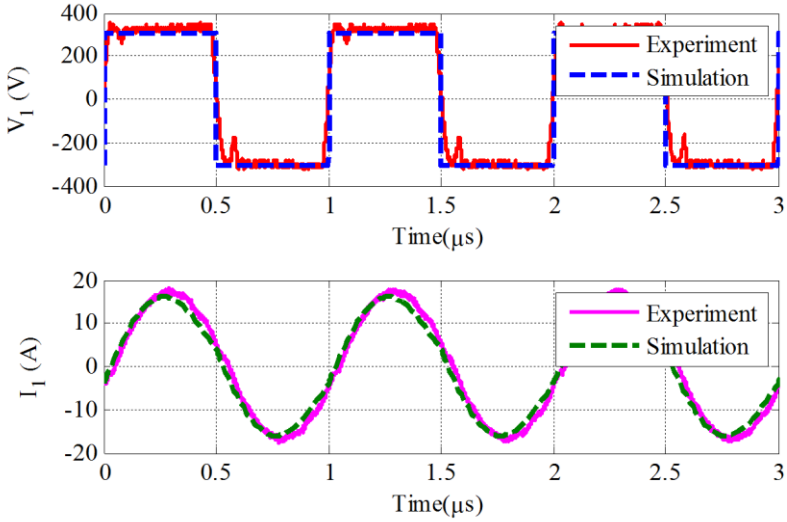

Fig. 3-15. Comparison of waveforms in simulated and experimental results

Fig. 3-15 shows the comparison of the input voltage and current waveforms between the simulated and experimental results. All the waveforms agree well with each other from the aspects of magnitude and phase angle.

The dashed blue curve is the input voltage in simulation, which is a perfect square-wave voltage source to accelerate calculation speed. The solid red curve is the experimental input voltage, which has a spike at the switching transient. This is because there is voltage stress on the MOSFETs at the turn-on transient, which can induce some switching losses. However, the magnitude of the pulse is lower than 50 V, so the induced power loss can be neglected. The dashed green curve is the simulated input current, and the solid pink curve is the experimental input current. Compared to the experimental voltage waveform, the experimental current has no noise. It shows that the simulated and experimental current waveforms match well. Their phase angles are almost the same, and the cut-off currents at switching transient are also the same.

When there is misalignment, C_s and k decrease as shown in Fig. 3-10. The FEA analysis

shows that the variations of $L_{1,2}$ and $C_{1,2}$ can be neglected. Therefore, the power equation (3-18) and the parameters in Table III-1 are used to calculate the system power at different misalignment conditions. The comparisons of the calculation and experiment results of the system total power and power ratio are shown in Fig. 3-16.

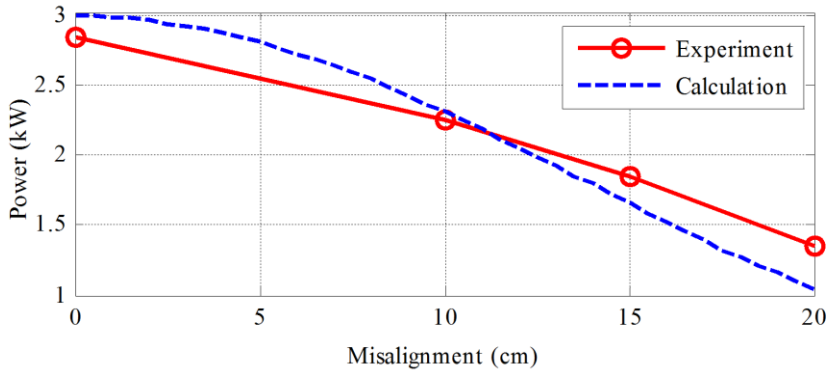

(a) Output power of IPT and CPT combined system

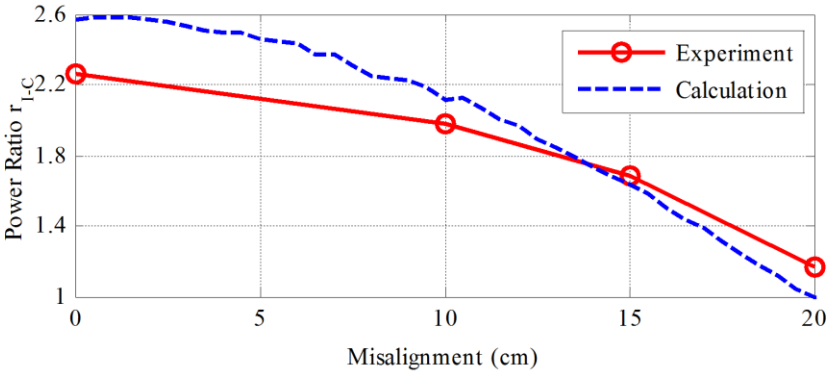

(b) Power ratio between IPT and CPT system

Fig. 3-16. Comparison of experimental and calculated power

Fig. 3-16 (a) shows that the calculated and experimental results of the system total power are close at different misalignment conditions. The maximum power difference is within 250 W. When the misalignment is small, the calculation is larger than the experiment result. This is because the calculation does not consider the power losses in the circuit components. When the misalignment increases, the calculation decreases to be lower than the experiment result. This is because the calculation is based on fundamental harmonics approximation (FHA), and all the high-order harmonics currents are neglected. However, with the increase of misalignment, the

high-order currents are becoming relatively larger when compared to the fundamental current, so the experiment result is larger than the calculation. It also needs to be emphasized that the difference of power between the calculated and experiment results also increase with misalignment. For example, Fig. 3-10 shows that, at 20 cm misalignment, the IPT power drops to 25.2%, and the CPT power drops to 62.1%. However, Fig. 3-16 shows that, in experiments, the IPT power drops to 38.5%, and the CPT power drops to 80.2%. This difference also comes from the approximation of FHA approach. However, the absolute value of the power difference is still in an acceptable range. In future research, the calculation expressions will be modified to consider all the high-order components.

Fig. 3-16 (b) shows the calculated and experimental power ratios between the IPT and CPT system. The maximum ratio difference is within 0.30. When the misalignment increases, both the inductive and capacitive power decreases. The power ratio is also decreasing, which means the capacitive power becomes comparable to the inductive power.

3.6. Conclusion

This chapter has proposed to combine IPT and CPT systems together into a single WPT system. The inductive and capacitive couplers also work as compensation components that resonate with each other to realize power transfer. An LC compensation circuit is also proposed, and the circuit working principle of the IPT and CPT combined system is presented, which shows a similarity with LCC-compensated IPT system and LCLC-compensated CPT system.

A prototype has been designed and implemented as an example to verify the proposed IPT-CPT combined system. The IPT system contributes 72% of the total power, and the CPT system is responsible for the remaining 28%. In experiments, the combined system achieves 2.84 kW output power through an air-gap distance of 150 mm with a dc-dc efficiency of 94.45%. The experimental results are also compared with the simulations, which show good agreements between each other and validate our design. The experimental results also prove that the CPT coupler has better misalignment performance than the IPT coupler. Therefore, the combined

system has the advantage of improved misalignment performance over an IPT system. In future work, the inductive and capacitive coupler will be integrated together to further improve the system power density.

3.7. References

[1] F. Musavi, W. Eberle, "Overview of Wireless Power Transfer Technology for Electric Vehicle Battery Charging," *IET Power Electron.*, vol. 7, no. 1, pp. 60-66, Jan. 2014.

[2] J. Dai, D. Ludios, "Capacitive Power Transfer Through a Conformal Bumper for Electric Vehicle Charging," *IEEE J. Emerg. Sel. Top. Power Electron.,* vol. 4, no. 3, pp. 1015-1025, Mar. 2016.

[3] C. Mi, G. Buja, S. Choi, C. Rim, "Modern Advances in Wireless Power Transfer Systems for Roadway Powered Electric Vehicles," *IEEE Trans. Ind. Electron.*, vol. 63, no. 10, pp. 6533- 6545, Oct. 2016.

[4] J. Yin, D. Lin, T. Parisini, S.Y. Hui, "Front-End Monitoring of Mutual Inductance and Load Resistance in a Series-Series Compensated Wireless Power Transfer System," *IEEE Trans. Power Electron.*, vol. 31, no. 10, pp. 7339-7352, Oct. 2016.

[5] W. Zhang, C. Mi, "Compensation Topologies of High-Power Wireless Power Transfer Systems," *IEEE Trans. Veh. Techn.*, vol. 66, no. 6, pp. 4768-4778, Jun. 2016.

[6] T. Kan, T.D. Nguyen, J.C. White, R. Malhan, C. Mi, "A New Integration Method for an Electric Vehicle Wireless Charging System Using LCC Compensation Topology: Analysis and Design," *IEEE Trans. Power Electron.*, vol. 32, no. 2, pp. 1638-1650, Feb. 2017.

[7] S. Li, W. Li, J. Deng, T.D. Nguyen, C.C. Mi, "A Double Sided LCC Compensation Network and Its Tuning Method for Wireless Power Transfer," *IEEE Trans. Veh. Techn.*, vol. 64, no. 6, pp. 2261-2273, Jun. 2015.

[8] Y. Su, S. Xie, A.P. Hu, C. Tang, W. Zhou, L. Huang, "A Capacitive Power Transfer System with a Mix-resonant Topology for Constant-current Multiple-Pickup Applications," *IEEE Trans. Power Electron.*, doi: 10.1109/TPEL.2016.2640314.

[9] F. Lu, H. Zhang, H. Hofmann, C. Mi, "A Double-sided LCLC-Compensated Capacitive Power Transfer System for Electric Vehicle Charging," *IEEE Trans. Power Electron.*, vol. 30, no. 11, pp. 6011-6014, Nov. 2015.

[10] J. Deng, F. Lu, S. Li, T. Nguyen, C. Mi, "Development of a High Efficiency Primary Side Controlled 7 kW Wireless Power Charger," *Proc. of IEEE Intern. Electric Veh. Conf.*, (*IEVC*), pp. 1-6, Dec. 2014.

[11] S. Li, C. Mi, "Wireless Power Transfer for Electric Vehicle Applications," *IEEE J. Emerg. Sel. Top. Power Electron.,* vol. 3, no. 1, pp. 4-17, Jan. 2015.

[12] F. Lu, H. Zhang, H. Hofmann, C. Mi, "A Double-Sided LC-Compensation Circuit for Loosely Coupled Capacitive Power Transfer," *IEEE Trans. Power Electron.*, 2017, doi: 10.1109/TPEL.2017.2674688.

[13] F. Lu, H. Zhang, H. Hofmann, C. Mi, "An Inductive and Capacitive Combined Wireless Power Transfer System with LC-Compensated Topology," *IEEE Trans. Power Electron.*, vol. 31, no. 12, pp. 8471-8482, Dec. 2016.

[14] W. Li, H. Zhao, S. Li, J. Deng, T. Kan, C. Mi, "Integrated LCC Compensation Topology for Wireless Charger in Electric and Plug-in Electric Vehicles," *IEEE Trans. Ind. Electron.*, vol. 62, no. 7, pp. 4215-

4225, July. 2015.

[15] F. Lu, H. Zhang, H. Hofmann, C. Mi, “A High Efficiency 3.3kW Loosely-Coupled Wireless Power Transfer System without Magnetic Material,” *Proc. IEEE Energy Convers. Congr. Expo. (ECCE)*, pp. 2282-2286, 2015.

[16] H. Zhang, F. Lu, H. Hofmann, W. Liu, C. Mi, “A Four-Plate Compact Capacitive Coupler Design and LCL-Compensated Topology for Capacitive Power Transfer in Electric Vehicle Charging Application,” *IEEE Trans. Power Electron.*, vol. 31, no. 12, pp. 8541-8551, Dec. 2016.

[17] F. Lu, H. Zhang, H. Hofmann, C. Mi, “An Inductive and Capacitive Integrated Coupler and Its LCL Compensation Circuit Design for Wireless Power Transfer,” *Proc. IEEE Energy Convers. Congr. Expo. (ECCE)*, pp. 1-5, Sept. 2016.

CHAPTER IV

DYNAMIC CAPACITIVE POWER TRANSFER

4.1. Introduction

Most of current wireless power transfer systems focus on stationary charging scenarios [1]. An electric vehicle should be parked over a charging pad, and the vehicle side receiver should be well-aligned with the transmitter to maximize the system power and efficiency. If there is a large misalignment between the receiver and transmitter, the system power and efficiency are usually significantly affected.

The concept of dynamic charging is proposed to overcome the limitations of stationary charging [2]. When the vehicle is moving on the roadway, it can be continuously powered. In this way, the driving range of an electric vehicle can be extended, and smaller amounts of batteries are required on the vehicle side [3]. The cost and weight of the vehicle is significantly reduced, and the overall transportation efficiency is improved. It has been proven that the driving range of an electric vehicle can be extended by at least 80% when 20% of the roads possess dynamic charging systems [4]. Therefore, dynamic charging technology is promising and can help to promote the use of electric vehicles.

Current dynamic charging systems can be classified according to the length of the transmitters; i.e., either long-track transmitters [5]-[7] or short-individual transmitters [8]. The system structure of dynamic charging systems is shown in Fig. 4-1. The primary side components, consisting of the power supply, power electronics, compensation circuits, and transmitters, are embedded on the ground side. The secondary side components, including the rectifier, compensation circuits, and a receiver, are installed on the vehicle side to pick up power

when the vehicle is moving. In a dynamic charging system, the transmitter and receiver can be either inductively or capacitively coupled, resulting in an IPT [9] or CPT [10] dynamic system.

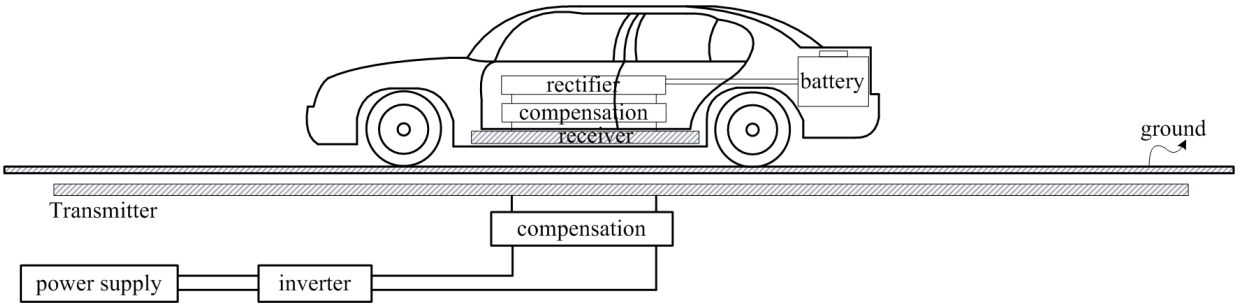

(a) Long-track transmitter

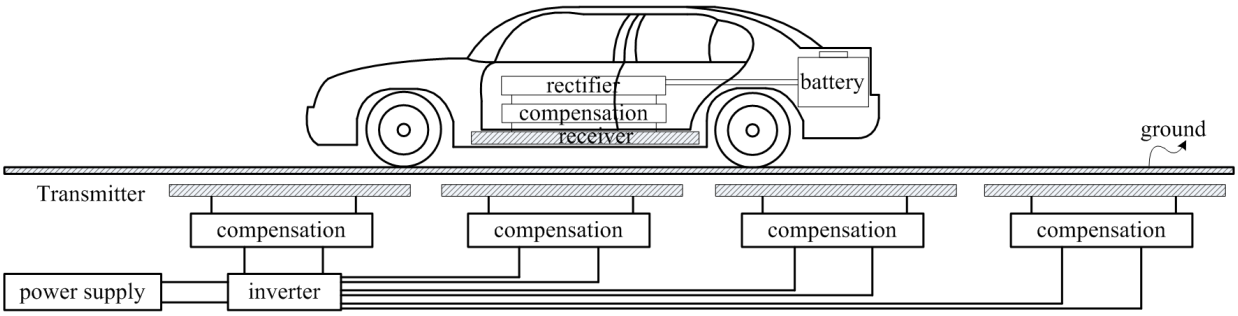

(b) Short-individual transmitter

Fig. 4-1. Structure of dynamic charging system with different transmitter lengths

The long-track transmitter is usually between tens to hundreds of meters long, which is much longer than the vehicle length [11]-[14]. A single transmitter can support multiple receivers simultaneously. It has a minimal number of circuit components and can reduce power pulsations due to vehicle movement. A dynamic IPT system is commercially available now, the so-called on-line electric vehicle (OLEV) for buses and trains, and its maximum charging power can reach hundreds of kW [15]-[17].

The short-individual transmitter has a smaller size, and multiple transmitters are arranged in a line to replace the previous long track [18], [19]. Each transmitter has its own compensation network, and it is easier to adjust the total length of the powered roadway. Also, the transmitters can be excited according to receiver position to save power [20].

When the long-track transmitter is applied in an IPT system, the advantage is its simplicity and less compensation components. However, the inner resistance of the coil is relatively large

and there is a large current circulating in the coil [21]. Therefore, the system efficiency is relatively poor. The magnetic field emission from a long transmitter is another important concern [22], [23]. The short-individual transmitter can help improve efficiency, but the system requires much more components and there can be significant power reduction in the position between two transmitters [20].

In this chapter, CPT technology is used to realize a long-track dynamic charging system, which can reduce the received power pulsations and overcome the low-efficiency property of a long-track IPT system [10]. In a CPT system, the voltages on the plates establish electric fields to transfer power, and so the circulating current can be reduced or even eliminated. As a result, the dynamic CPT system efficiency can be improved.

4.2. Dynamic Capacitive Coupler Design

4.2.1 Coupler Structure

The structure and dimensions of a dynamic capacitive coupler is shown in Fig. 4-2.

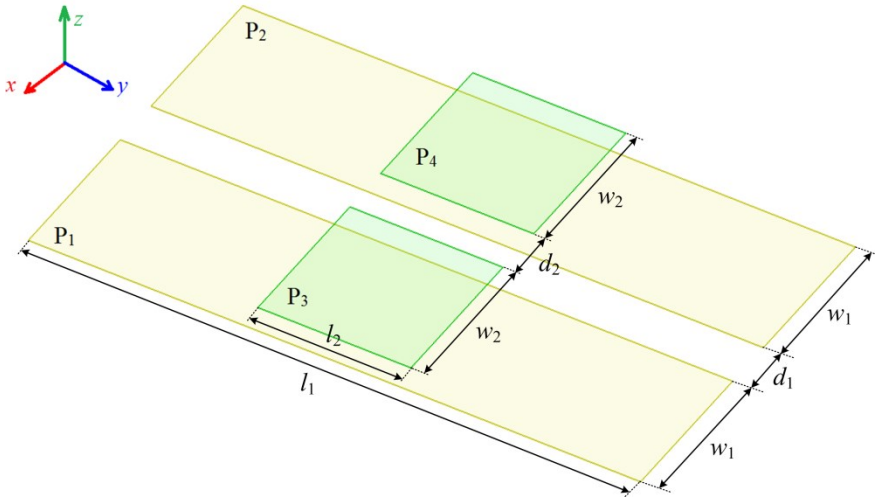

(a) 3-D view

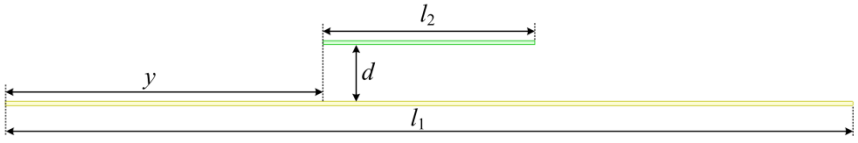

(b) Front view

Fig. 4-2. Structure and dimensions of a capacitive coupler for dynamic charging

Fig. 4-2(a) shows the 3D view of a dynamic capacitive coupler. The primary plates P_1 and P_2 form a long track as a power transmitter, and the secondary plates P_3 and P_4 can move freely along the track while receiving continuous power. The total length of each track plate is defined as l_1, and its width is defined as w_1. The receiver length is defined as l_2, and its width is defined as w_2. The separation distance between primary plates is defined as d_1, and the separation distance between secondary plates is d_2. The *x*-*y*-*z* direction is also indicated in Fig. 4-2(a) to show the relative position between transmitter and receiver plates.

Fig. 4-2(b) shows the front view of the capacitive coupler, which indicates an air-gap distance d between the transmitter and receiver. The receiver can move along the y-direction over the track, and its relative position with respect to the transmitter is defined as y. The position where the left edge of the receiver is well-aligned with the left edge of the transmitter is defined as the zero position.

This coupler is used to validate a dynamic CPT system, and its power and size are downscaled for easy demonstration. Considering the aluminum sheets available in the lab, the length l_1 of transmitter track is set to be 1200 mm, and its width w_1 is set to be 300 mm. The receiver is designed to be square with l_2 and w_2 both at 300 mm. In this design, the transmitter is much longer than the receiver to allow a significant distance for the receiver to move. The thickness of the plates has little effect on capacitive coupling, which is set to be 2 mm. The air-gap d is 50 mm in this demonstration, and can be increased to 150 mm in future high-power systems. To summarize, the descriptions and values of the designed coupler dimensions are provided in Table IV-1.

Table IV-1. Dimensions of a capacitive coupler for dynamic power transfer

Parameter	Description	Value	Parameter	Description	Value
l_1	transmitter length	1200mm	l_2	receiver length	300mm
w_1	transmitter width	300mm	w_2	receiver width	300mm
d_1	transmitter distance	100mm	d_2	receiver distance	100mm
y	receiver position	varies	d	air-gap distance	50mm

4.2.2 Circuit Model

In this coupler, since the same-side plates are close together, the capacitive couplings P_1-P_2 and P_3-P_4 cannot be neglected. Due to the possible misalignment between the transmitter and receiver plates in practical applications, the cross couplings P_1-P_4 and P_2-P_3 should also be considered. Therefore, there are six significant capacitive coupling capacitances in this dynamic coupler, which is similar to the six-capacitance model of Fig. 3-4(a) in Chapter III. Different from the four-capacitance equivalent model in Fig. 3-4(b), a more general model is proposed to simplify the six-capacitance model, as shown in Fig. 4-3.

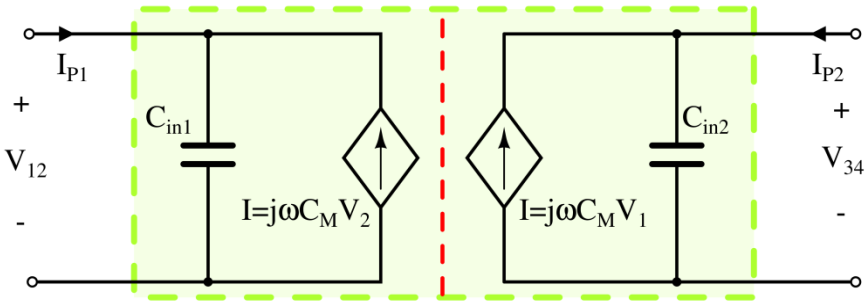

Fig. 4-3. Behavior source model of the capacitive coupler

In Fig. 4-3, two voltage-controlled current sources are used to represent the capacitive couplings between the primary and secondary side. This is known as a behavior source model. It is similar to the circuit model of a conventional transformer. Then, the primary and secondary capacitance is defined as C_{in1} and C_{in2}, and the mutual capacitance is defined as C_M. The input and output relationship in Fig. 4-3 can be expressed as,

$$\begin{cases} I_{P1} = j\omega_s C_{in1} \cdot V_{12} - j\omega_s C_M \cdot V_{34} \\ I_{P2} = -j\omega_s C_M \cdot V_{12} + j\omega_s C_{in2} \cdot V_{34} \end{cases} \tag{4-1}$$

Compared with the six-capacitor description in equation (3-2), the equivalent parameters are expressed as,

$$\begin{cases} C_M = \dfrac{C_{13}C_{24} - C_{14}C_{23}}{C_{13} + C_{14} + C_{23} + C_{24}} \\ C_{in1} = \dfrac{(C_{13} + C_{14}) \cdot (C_{23} + C_{24})}{C_{13} + C_{14} + C_{23} + C_{24}} + C_{12} \\ C_{in2} = \dfrac{(C_{13} + C_{23}) \cdot (C_{14} + C_{24})}{C_{13} + C_{14} + C_{23} + C_{24}} + C_{34} \end{cases} \tag{4-2}$$

4.2.3 Maxwell Simulation

Finite element analysis (FEA) by Maxwell is used to simulate the coupling capacitances in the designed dynamic capacitive coupler. It can directly provide the six coupling capacitances between every two plates, which can be used to calculate the equivalent capacitances using (4-2). The dimensions of the capacitive coupler have been provided in Table IV-1.

When the receiver is well-aligned with the transmitter and located at the middle position of the long track, its relative position is y=450mm. The resulting Maxwell-simulated coupling capacitances are provided in Table IV-2. The equivalent capacitances C_{in1}, C_{in2}, and C_M in Fig. 4-3 are also calculated. The Maxwell simulation result shows that the cross-coupling capacitances C_{14} and C_{23} are much smaller than C_{13} and C_{24}, which means C_{13} and C_{24} dominate the mutual capacitance C_M as expressed in (1). The self-capacitances (C_{in1} and C_{in2}) are relatively small, so external capacitances will be required to be connected in parallel with the plates to increase the total equivalent capacitances.

Table IV-2. Maxwell-simulated capacitances at the middle position when y=450mm

	P_1	P_2	P_3	P_4
P_1		C_{12}=11.07 pF	C_{13}=24.42 pF	C_{14}=0.99 pF
P_2	C_{12}=16.49pF		C_{23}=0.99 pF	C_{24}=24.42 pF
P_3	C_{13}=24.42 pF	C_{23}=0.99 pF		C_{34}=1.11 pF
P_4	C_{14}=0.99 pF	C_{24}=24.42 pF	C_{34}=1.11 pF	
	C_{in1}=23.80 pF, C_{in2}=13.84 pF, C_M=11.73 pF			

The coupling capacitances between plates are then simulated, as the receiver moves along the transmitter track, and the equivalent capacitances C_{in1}, C_{in2}, and C_M are calculated as shown in Fig. 4-4. The varying range of the position y is [-200 mm, 1200 mm], in which negative position means the receiver extends beyond of the left edge of the transmitter. Also, considering the lengths of transmitter and receiver plates, a position y larger than 900 mm means that the receiver extends beyond the right edge of the transmitter. In these simulations, misalignment is neglected.

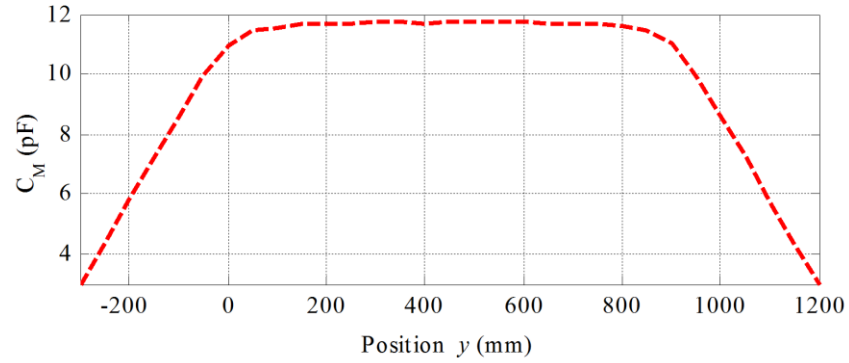

(a) Mutual capacitance C_M

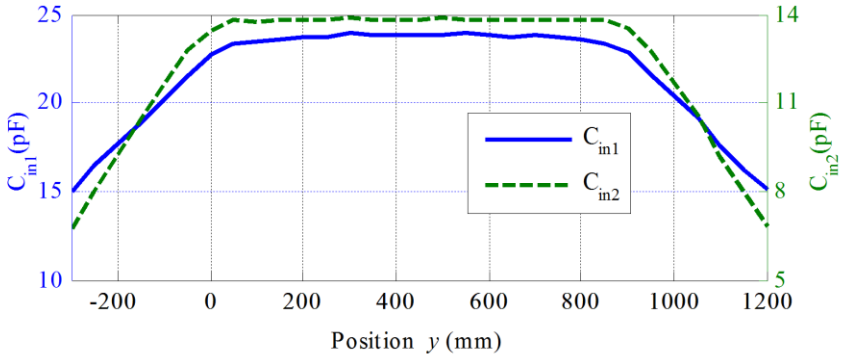

(b) Self-capacitance C_{in1} and C_{in2}

Fig. 4-4. Maxwell-simulated equivalent capacitances at different receiver position y

When the position y is in the range of [-300 mm, 0 mm], the receiver starts to move towards the transmitter and the capacitances are increasing. When the position y is in the range of [0 mm, 900 mm], the receiver overlaps the transmitter and the capacitances are essentially constant. When the position y is in the range of [900 mm, 1200 mm], the receiver moves away from the transmitter, and the capacitances are decreasing. Since the transmitter plates are larger than the receiver plates, C_{in1} is larger than C_{in2}.

In practical applications, there is unavoidable misalignment between the transmitter and receiver when the receiver is moving. The relationship between the equivalent capacitances and x direction misalignment is shown in Fig. 4-5. The misalignment performance is symmetric from left to right. At 200 mm x misalignment, the mutual capacitance C_M decreases from 11.8 pF to 5.1 pF, C_{in1} decreases from 23.8 pF to 21.0 pF, and C_{in2} decreases from 13.8 pF to 11.5 pF. Compared to the mutual capacitance C_M, self-capacitances C_{in1} and C_{in2} are less sensitive to x direction misalignment.

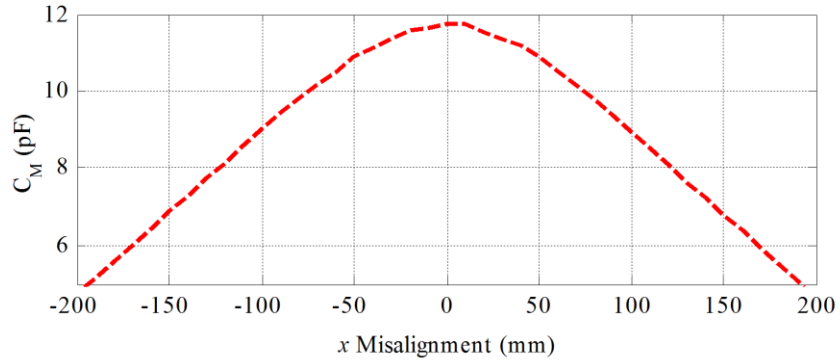

(a) Mutual capacitance C_M

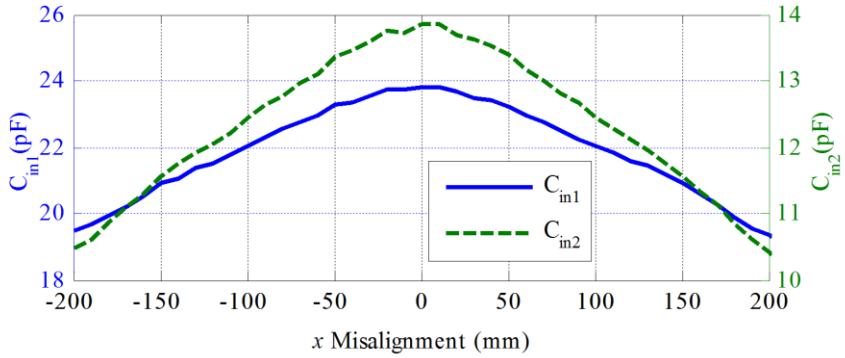

(b) Self-capacitance C_{in1} and C_{in2}

Fig. 4-5. Maxwell-simulated equivalent capacitances at different x misalignment

4.3 An Example of LCLC-Compensated Dynamic CPT System

4.3.1 Circuit Topology

A double-sided LCLC compensation circuit [24] is used to realize a dynamic CPT system with the designed capacitive coupler. The circuit topology is shown in Fig. 4-6.

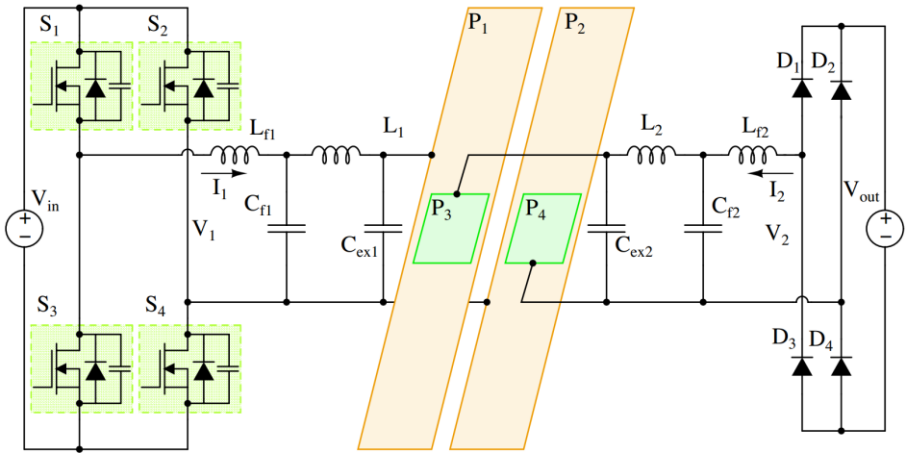

Fig. 4-6. Circuit topology of a double-sided LCLC-compensated dynamic CPT system

Two external capacitors, C_{ex1} and C_{ex2}, are connected in parallel with the plates to increase the equivalent self-capacitances and reduce the required resonant inductances. Using the behavior source model to substitute the capacitive coupler, the equivalent circuit of the dynamic CPT system is shown in Fig. 4-7.

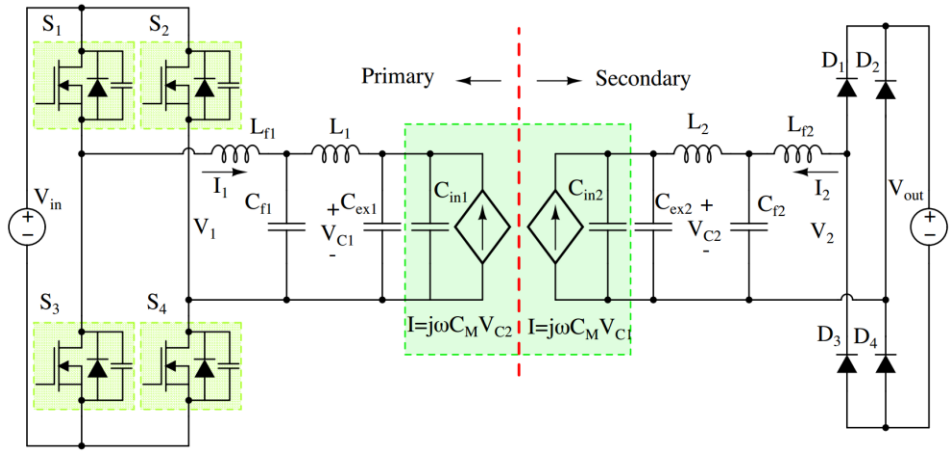

Fig. 4-7. Equivalent circuit of a double-sided LCLC-compensated dynamic CPT system

The internal and external capacitances can be considered together, resulting in equivalent self-capacitances expressed as,

$$\begin{cases} C_{eq1} = C_{in1} + C_{ex1} \\ C_{eq2} = C_{in2} + C_{ex2} \end{cases} \tag{4-3}$$

The capacitive coupling coefficient is defined as k_C, which is expressed as,

$$k_C = \frac{C_M}{\sqrt{C_{eq1} C_{eq2}}} \tag{4-4}$$

According to Chapter II, when the switching frequency is ω_0, the resonance relationship between the parameters are expressed as,

$$\begin{cases} L_{f1} = \dfrac{1}{\omega_0^2 C_{f1}} \\ L_{f2} = \dfrac{1}{\omega_0^2 C_{f2}} \\ L_1 = \dfrac{1}{\omega_0^2 C_{eq1} \cdot (1 - k_C^2)} + L_{f1} \\ L_2 = \dfrac{1}{\omega_0^2 C_{eq2} \cdot (1 - k_C^2)} + L_{f2} \end{cases} \tag{4-5}$$

The system output power is calculated as,

$$P_{out} = \frac{\omega_0 C_M \cdot C_{f1} C_{f2}}{C_{eq1} C_{eq2} \cdot (1 - k_C^2)} \cdot |V_1| \cdot |V_2| \tag{4-6}$$

4.3.2 Circuit Parameters Design

Using the long-track capacitive coupler and double-sided LCLC compensation circuit, a 150W dynamic CPT system is designed. The system specifications and circuit parameters are shown in Table IV-3.

Table IV-3. System specifications and circuit parameter values

Parameter	Design Value	Parameter	Design Value
V_{in}	60 V	V_{out}	60 V
L_{f1}	3.76 μH	L_{f2}	3.76 μH
C_{f1}	2.99 nF	C_{f2}	2.99 nF
C_{in1}	23.80 pF	C_{in2}	13.84 pF
C_{ex1}	100 pF	C_{ex2}	120 pF
L_1	87.1 μH	L_2	87.4 μH
C_M	11.73 pF	k_C	9.11%

In this low power system, the input and output dc voltages are set to 60V, and the switching frequency is set to 1.5 MHz. All other parameters are calculated based on the resonant relationship in (4-5) and the power equation (4-6). For simplicity, the primary and secondary parameters are symmetric. Since the internal capacitance C_{in1} is larger than C_{in2}, the external capacitance C_{ex1} is smaller than C_{ex2}. Considering the capacitors available in the lab, C_{ex1} is set to be 100 pF, and C_{ex2} is set to be 120 pF.

4.3.3 Circuit Simulation

After the circuit parameters are determined, LTspice is further used to simulate the circuit performance of the dynamic CPT system. The input and output waveforms are shown in Fig. 4-8. The power losses in circuit components are neglected to simplify the simulation process.

The waveforms of this dynamic CPT system are similar to the LCLC-compensated stationary CPT system in Chapter II. Since an uncontrolled diode rectifier is used at the secondary side, the output voltage V_2 is in phase with the output current ($-I_2$). The simulation also shows that the input voltage V_1 is also in phase with the input current I_1, which limits the reactive

power circulating in the circuit and improves the system efficiency. Also, V_2 is leading V_1 by 90°. At the switching transient, the input current magnitude is about 1.0 A, which can help the soft-switching of MOSFETs in the input inverter.

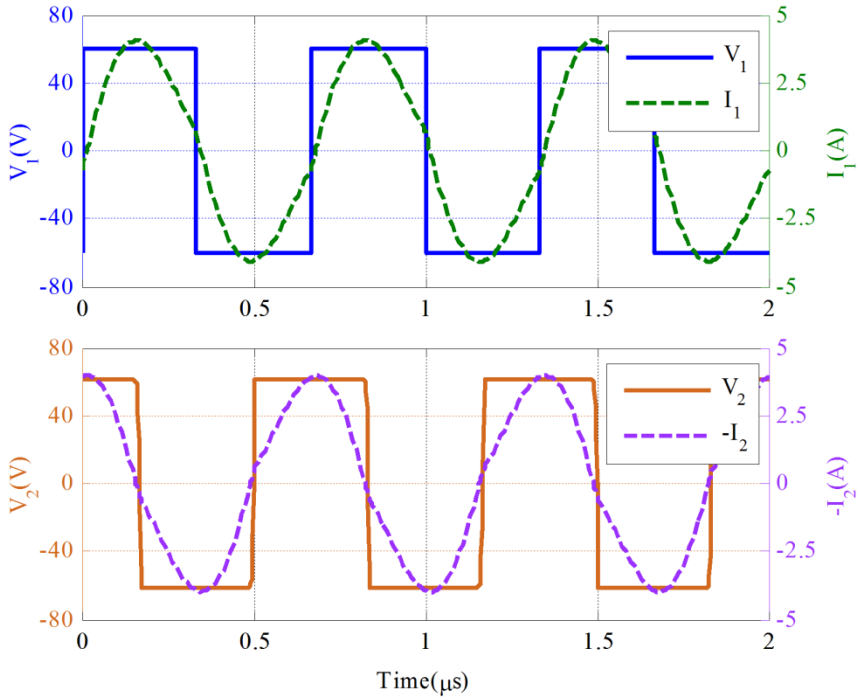

Fig. 4-8. LTspice-simulated input and output waveforms of a dynamic CPT system

4.4 Experimental Results

4.4.1. Experimental Setup

A prototype of the dynamic CPT system was implemented, according to the coupler dimensions in Table IV-1 and circuit parameters in Table IV-3, as shown in Fig. 4-9. Aluminum plates were used to build the capacitive coupler. The transmitter plates are much longer than the receiver plates, and the receiver can move along the transmitter track to test the dynamic power transfer capability. The transmitter plates are fixed on wooden boards, and the receiver plates are mounted on plastic. The usage of wood and plastic is minimized in order to reduce their influence on the coupling capacitances. Plastic tubes are used to adjust the air-gap distance between the transmitter and receiver plates. In this setup, the distance is set to be 50 mm.

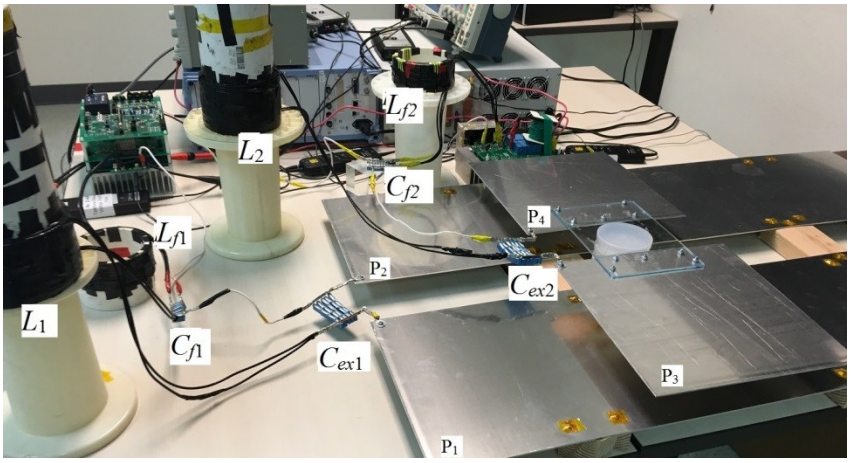

Fig. 4-9. Prototype of a double-sided LCLC-compensated dynamic CPT system

Since the switching frequency is 1.5 MHz, 2175-strand AWG 46 Litz-wire is used to wind the resonant inductors to mitigate the skin effect losses. The inductors have an air-core to mitigate the magnetic losses. The inductors are arranged far from each other to reduce the magnetic coupling between them. High-frequency film capacitors from KEMET are used to build all the compensation capacitances. The same SiC inverter as in Chapter II and III is used to provide high-frequency ac excitation. Also, the same rectifier is used at the output side to supply power to an electronic load.

4.4.2. Stationary Experiments

When the receiver is located at y=450 mm position and well-aligned with the transmitter plates, the experimental results, including waveforms and power, are shown in Fig. 4-10(a) and (b), respectively. When the input and output voltages increase to 60V, the system input power reaches 181.1 W, and the output power is 154.7 W, resulting in a dc-dc efficiency of 85.4% and a power loss of 26.4 W. The experimental waveforms in Fig. 4-10(b) are similar to the simulation results in Fig. 4-8. The input current I_1 is slightly lagging V_1 to maintain the soft-switching of MOSFETs in the input inverter. The output voltage V_2 is 90° leading the input voltage V_1, which is consistent with the simulation waveforms. There is noise on the input and output current waveforms. In future setups, if better probes are used, it is expected that the measured noise can be significantly reduced.

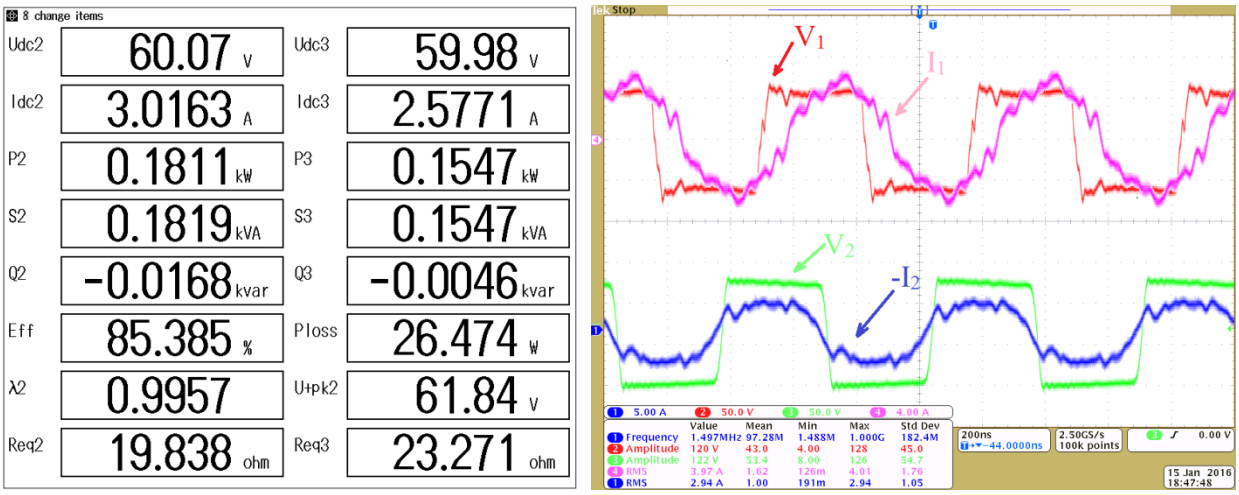

(a) power (b) waveforms

Fig. 4-10. Experimental results of the dynamic CPT system at well-aligned position when y=450mm

The experimental results in Fig. 4-10(a) show that the dc-dc efficiency of this dynamic CPT system is relatively lower than the efficiency of a conventional CPT or IPT system. The power loss breakdown [25] among the circuit components is estimated and shown in Fig. 4-11.

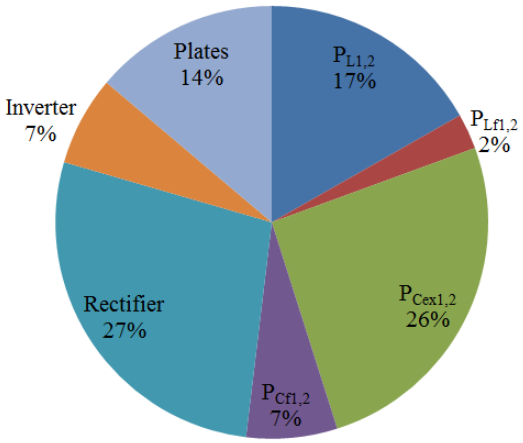

Fig. 4-11. Estimated power loss distribution in the dynamic CPT system

The parasitic resistances of the MOSFETs, compensation inductors and capacitors can be estimated from their datasheets and measurements. The forward voltage o the diodes in the rectifier can also be obtained from the datasheet. Using the simulated currents flowing through the components, their power loss is therefore estimated. Since the soft-switching of MOSFETs is realized, the switching loss can be neglected. The experimental total loss is 26.4 W in Fig. 4-10(b), and so it is assumed that the remaining power losses is in the plates. In this low-power

system, it is seen that the diodes in the rectifier dissipate most of the power loss, which is 27% of the total loss. The compensation inductors and capacitors also dissipate significant power. In future designs, when the system power further increases, the relative power loss dissipated by the diodes will be reduced, and so the system efficiency will be improved. Also, the power loss in the inductors can be reduced by using more strands of Litz-wire, and the power loss in the capacitors can be reduced by using better capacitors with lower dissipation factor. In this way, the system efficiency is expected to reach at least 90%.

The system dc-dc efficiency was also measured at different voltages and power levels, as shown in Fig. 4-12. This indicates that the system efficiency increases with output power, and it saturates when the output power is high. After the output power reaches 70W, the system efficiency maintains higher than 84%. According to reference [26], the system efficiency is determined by the coupling coefficient k_C and the quality factor of circuit components. In this system, the coupling coefficient k_C is only 9.11%, and so the system efficiency is relatively low. In future designs, both the coupling coefficeint k_C and the quality factor will be improved to obtain higher system efficiency.

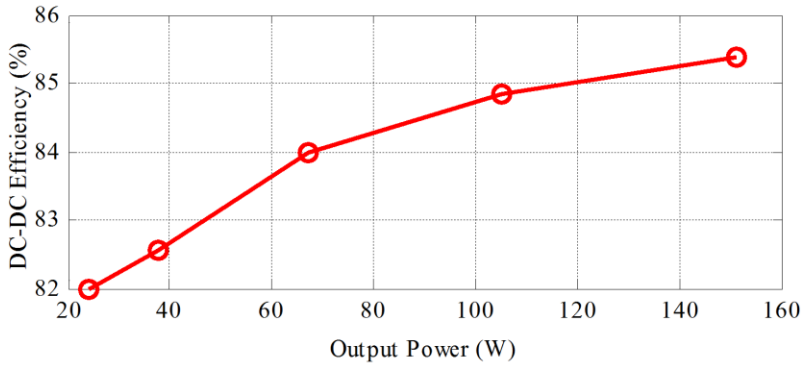

Fig. 4-12. Experimental dc-dc efficiency at different output power

4.4.3. Dynamic Experiments

The system power was measured at different receiver positions in the y-direction, and compared with the simulation result, as shown in Fig. 4-13. Maxwell was used to simulation the coupling capacitances. The simulated capacitances are then used in LTspice to calculate the system power.

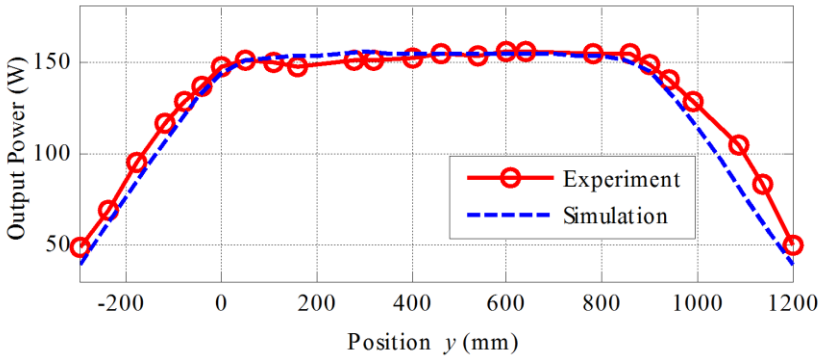

Fig. 4-13. Experimental and simulated output power at different position *y*

Fig. 4-13 shows that the experimental output power is consistent with the simulated power. When the receiver is entering the transmitter (*y*=[-300mm, 0mm]), the received power keeps increasing. As long as the receiver overlaps the transmitter track (*y*=[0mm, 900mm]), the received power is almost constant, and the power variation along the track is within ±4.0% of the nominal power. When the receiver is leaving the transmitter (*y*=[900mm, 1200mm]), the received power starts to decrease. Therefore, the experimental results show that the proposed dynamic CPT system can effectively reduce output power pulsations while moving.

The *x*-direction (as indicated in Fig. 4-2) misalignment performance of the dynamic CPT system is also studied, as shown in Fig. 4-14. The experimental results are also compared with the simulation results acquired from Maxwell and LTspice.

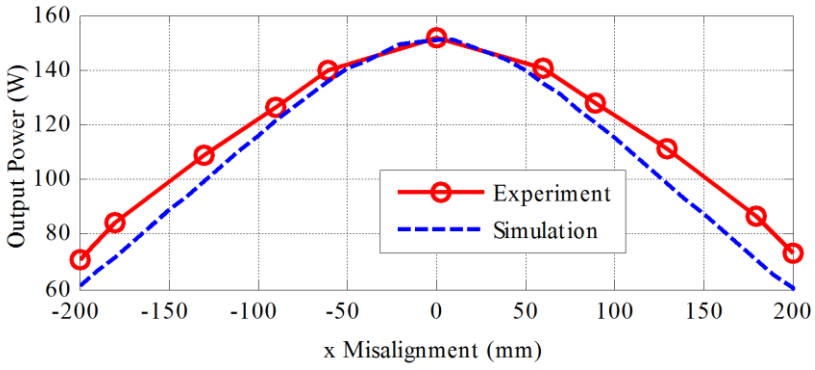

Fig. 4-14. Experimental and simulated output power at different *x* misalignment

Fig. 4-14 shows that the system power reduces with misalignment. When the *x* misalignment increases to 200 mm, the output power decreases to 72.3W, which is about 46.7% of the well-aligned value. The experimental power is consistent with the simulated result, except that

the experimental result is slightly larger. The difference is likely caused by high-order harmonic currents in the experimental system, which are neglected in the simulation. In this dynamic CPT system, the width of the transmitter and receiver plates is only 300 mm, and the misalignment is as large as 200 mm. Therefore, the experimental results show that this system has good misalignment performance.

4.4.4. Discussion: Challenges in Dynamic CPT System

In practical applications, there are three major challenges in a long-track dynamic CPT system. First, the self-inductance of the transmitter plate affects the power transfer process at different positions. Second, electric field emissions to the surrounding environment can cause safety issues, and so should be reduced. Third, at very high frequencies, the radiated loss from the transmitter plate to free space can be significantly increased, which affects the system efficiency and safety.

It is possible to have a transmitter length up to several tens of meters in highway and railway applications [14]-[17]. Then, the connection position of the primary compensation circuit affects the current flow path on the transmitter plate. Since the transmitter plate is very long, it is better to connect the compensation circuit in the middle of the plate to shorten the current path. Also, in a dynamic system, there could be multiple receivers moving along the transmitter track. Two typical positions of the receiver are used to illustrate the influence of transmitter plate inductance as shown in Fig. 4-15.

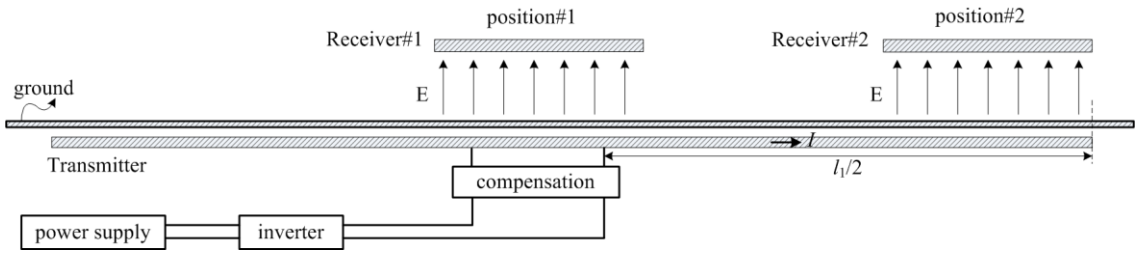

Fig. 4-15. A long-track CPT system with multiple receivers at different positions

In Fig. 4-15, receiver #1 is placed in the middle of the transmitter plate, just on top of the connection of compensation circuit. Receiver #2 is placed at the edge of the transmitter plate,

and so the current needs to travel half of the plate length to arrive the receiver. Since the transmitter plate can be tens of meters long, some preliminary Maxwell simulations show that it can induce tens of μH self-inductance, which can affect the resonance in the circuit and reduce the transferred power. When the switching frequency increases, for example 6.78 MHz frequency, the required resonant inductance is reduced, and so the influence of the plate self-inductance can be much more significant. Cutting the long track into pieces and connecting them with cables of twisted-pair can mitigate the self-inductance, but it still need further investigation to evaluate how much it can help. Therefore, it is meaningful to study the self-inductance of the transmitter plate, either reducing its effect or making full use of this inductance in the circuit.

Electric field emissions of the long track transmitter are another critical concern. For example, the Maxwell-simulated electric field emissions of the designed dynamic CPT system in this chapter are shown in Fig. 4-16.

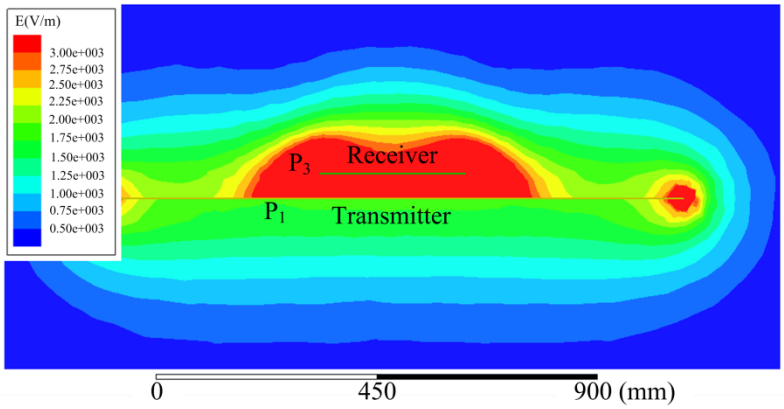

Fig. 4-16. Maxwell-simulated electric field emission of the designed dynamic CPT system

It can be seen that the electric fields concentrate in the air-gap between the transmitter and receiver plates. However, there are also large amount of electric fields external to the air-gap, which is a safety issue.

The field emission problem also exists in dynamic CPT systems, where the magnetic field emissions can be reduced by coil structure design [22] and active field cancellation [27]. Considering these two methods, a six-plate capacitive coupler structure is proposed to reduce electric field emissions in a CPT system [28]. Active electric field cancellation [29] is another

option to solve the field emission problem. In future research, both the coupler structure optimization and active field cancellation method will be studied for practical applications.

According to the resonance relationship in (4-5), increasing f_{sw} helps to reduce the size of the passive components, especially the inductors. Also, (4-6) shows that increasing f_{sw} contributes to transferring more power. Therefore, f_{sw} should be higher to improve the system performance. With the development of modern wide-band-gap semiconductor material, the switching frequency of a high-power device is expected to reach as high as 100 MHz.

When the switching frequency f_{sw} increases, the wavelength λ of the generated electromagnetic waves is reduced. According to the relationship $c=\lambda \cdot f_{sw}$, where c is the light speed, the quarter wavelength λ/4 of the electromagnetic wave is shown in Fig. 4-17.

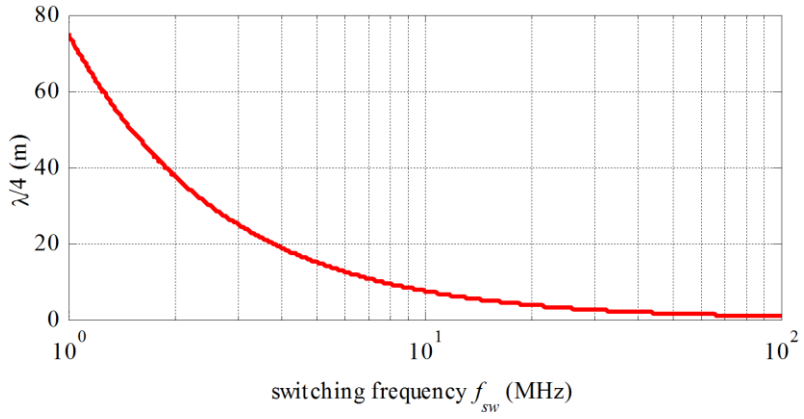

Fig. 4-17. Relationship between switching frequency f_{sw} and quarter wavelength λ/4

Fig. 4-17 shows that when the switching frequency is 1 MHz， λ/4=75 m. When the switching frequency is 100 MHz, λ/4=0.75 m. However, if the transmitter plate length is close or large than λ/4, it will act as an antenna to radiate a significant amount of the system power to space. Therefore, the power transfer efficiency can be significantly reduced, and the radiated high power electromagnetic fields can cause severe safety issues.

The self-inductance, electric field emission, and antenna effect of the transmitter plates are three important aspects that limit the application of dynamic CPT technology. In future research, they are very good areas for further investigation.

4.5. Conclusion

In this chapter, a long-track transmitter plate structure is used to realize a dynamic CPT system. It helps to reduce the power pulsation of the received power while moving, and can be applied in highway or railway applications. A low power dynamic CPT system is designed and implemented using double-sided LCLC compensation to validate the proposed idea.

The transmitter plate length is 1200 mm, and the receiver plate length is 300mm. The experimental results show that the prototype achieves 154.7W power transfer across an air-gap distance of 50mm with a dc-dc efficiency of 85.4%. When the receiver moves along the transmitter track, the received power pulsation is within ±4.0% of the nominal power. Moreover, the system has good misalignment performance, and can maintain about half of the well-aligned power when the misalignment is 200 mm.

In further discussion, three major challenges in the application of dynamic CPT technology are proposed: the self-inductance, electric field emissions, and radiation effects of the long-track transmitter plate. In future research, these three aspects will be studied to improve the practical application of dynamic CPT technology.

4.6. References

[1] G. A. Covic, J.T. Boys, "Modern Trends in Inductive Power Transfer for Transportation Application," *IEEE Jour. of Emerg. and Selec. Top. on Power Electr*., vol. 1, pp. 28-40, 2013.

[2] C. Mi, G. Buja, S.Y. Choi, C. Rim, "Modern Advances in Wireless Power Transfer Systems for Roadway Powered Electric Vehicles," *IEEE Trans. Ind. Electron.*, vol. 63, no. 10, pp. 6533-6545, 2016.

[3] S.Y. Choi, B.W. Gu, S.Y. Jeong, C.T. Rim, "Advances in Wireless Power Transfer Systems for Roadway-Powered Electric Vehicles," *IEEE Jour. of Emerg. and Selec. Top. on Power Electr*., vol. 3, pp. 18-36, 2015.

[4] S. Jeong, Y.J. Jang, D. Kum, "Economic Analysis of the Dynamic Charging Electric Vehicle," *IEEE Trans. Pow. Electron.*, vol. 30, pp. 6368-6377, 2015.

[5] J. Shin, S. Shin, Y. Kim, S. Ahn, S. Lee, G. Jung, S. Jeon, D. Cho, "Design and Implementation of Shaped Magnetic-Resonance-Based Wireless Power Transfer System for Roadway-Powered Moving Electric Vehicle," *IEEE Trans. Ind. Electron.*, vol. 61, pp. 1179-1192, 2014.

[6] V. Prasanth, P. Bauer, "Distributed IPT Systems for Dynamic Powering Misalignment Analysis," *IEEE Trans. Ind. Electron.*, vol. 61, pp. 6013-6021, 2014.

[7] F. Pijl, M. Castilla, P. Bauer, “Adaptive Slide-Mode Control for a Multiple-User Inductive Power Transfer System without Need for Communication,” *IEEE Trans. Ind. Electron.*, vol. 60, pp. 271-279, 2013.

[8] J.M. Miller, O.C. Onar, C.P. White, S. Campbell, “Demonstrating Dynamic Wireless Charging of an Electric Vehicle: The Benefit of Electrochemical Capacitor Smoothing,” *IEEE Pow. Electron. Maga.*, vol. 1, pp. 12-24, 2014.

[9] F. Lu, H. Zhang, H. Hofmann, C. Mi, “A Dynamic Charging System with Reduced Output Power Pulsation for Electric Vehicles,” *IEEE Trans. Ind. Electron.*, vol. 63, no. 10, pp. 6580-6590, 2016.

[10] F. Lu, H. Zhang, H. Hofmann, Y. Mei, C. Mi, “A Dynamic Capacitive Power Transfer System with Reduced Power Pulsation,” *Proc. IEEE Workshop Emerg. Tech. Wireless Power Trans.* (WoW), pp. 60-64, 2016.

[11] G.A. Covic, J.T. Boys, M. Kissin, H.G. Lu, “A Three-Phase Inductive Power Transfer System for Roadway-Powered Vehicles,” *IEEE Trans. Ind. Electron.*, vol. 54, pp. 3370-3378, 2007.

[12] M. Kissin, J.T. Boys, G.A. Covic, “Interphase Mutual Inductance in Polyphase Inductive Power Transfer Systems,” *IEEE Trans. Ind. Electron.*, vol. 56, pp. 2393-2400, 2009.

[13] W.Y. Lee, J. Huh, S.Y. Choi, X. Thai, J. Kim, E. Al-Ammar, A. El-Kady, C.T. Rim, “Finite-Width Magnetic Mirror Models of Mono and Dual Coils for Wireless Electric Vehicles,” *IEEE Trans. Pow. Electron.*, vol. 28, pp. 1413-1428, 2013.

[14] G.A. Elliott, S. Raabe, G.A. Covic, J.T. Boys, “Multiphase Pickups for Large lateral Tolerance Contactless Power-Transfer Systems,” *IEEE Trans. Ind. Electron.*, vol. 57, pp. 1590-1598, 2010.

[15] Y.D. Ko, Y.J. Jang, “The Optimal System Design of the Online Electric Vehicle Utilizing Wireless Power Transmission Technology,” *IEEE Trans. Intel. Transp. Syst*. Vol 3, pp. 1255-1265, 2013.

[16] Y.J. Jang, E.S. Suh, J.W. Kim, “System Architecture and Mathematical Models of Electric Transit Bus System Utilizing Wireless Power Transfer Technology,” *IEEE Syst. Jour.*, vol. PP. pp. 1-12, 2015, DOI: 10.1109/JSYST.2014.2369485.

[17] S. Choi, J. Huh, W.Y. Lee, S.W. Lee, C.T. Rim, “New Cross-Segmented Power Supply Rails for Roadway-Powered Electric Vehicle,” *IEEE Trans. Pow. Electron.*, vol. 28, pp. 5832-5841, 2013.

[18] S. Zhou, C. Mi, “Multi-Paralleled LCC Reactive Power Compensation Networks and Their Tuning Method for Electric Vehicle Dynamic Wireless Charging,” *IEEE Trans. Ind. Electron.*, vol. 63, no. 10, pp. 6546-6556, 2016.

[19] J.M. Miller, P.T. Jones, J. Li, O.C. Onar, “ORNL Experience and Challenges Facing Dynamic Wireless Power Charging of EV’s,” *IEEE Cir. and Syst. Maga.*, vol. 15, pp. 40-53, 2015.

[20] K. Lee, Z. Pantic, S.M. Lukic, “Reflexive Field Containment in Dynamic Inductive Power Transfer Systems,” *IEEE Trans. Pow. Electron.*, vol. 29, pp.4592-4602, 2014.

[21] S. Raabe, G.A. Covic, “Practical Design Considerations for Contactless Power Transfer Quadrature Pick-Ups,” *IEEE Trans. Ind. Electron.*, vol. 60, pp. 400-409, 2013.

[22] J. Huh, S.W. Lee, W.Y. Lee, G.H. Cho, C.T. Rim, “Narrow-Width Inductive Power Transfer System for Online Electric Vehicle,” *IEEE Trans. Pow. Electron.*, vol. 26, pp. 3666-3679, 2011.

[23] S.Y. Choi, J. Huh, W.Y. Lee, C.T. Rim, “Asymmetric Coil Set for Wireless Stationary EV Chargers with Lateral Tolerance by Dominant Field Analysis,” *IEEE Trans. Pow. Electron.*, vol. 29, pp. 6406-6420, 2014.

[24] F. Lu, H. Zhang, H. Hofmann, C. Mi, “A Double-Sided LCLC-Compensated Capacitive Power Transfer System for Electric Vehicle Charging,” *IEEE Trans. Power Electron.*, vol. 30, no. 11, pp. 6011-6014, 2015.

[25] F. Lu, H. Zhang, H. Hofmann, C. Mi, “A High Efficiency 3.3kW Loosely-Coupled Wireless Power Transfer

System without Magnetic Material," *Proc. IEEE Energy Convers. Congr. Expo. (ECCE)*, pp. 2282-2286, 2015.

[26] S. Choi, B. Gu, S.W. Lee, W.Y. Lee, J. Huh, C.T. Rim, "Generalized Active EMF Cancel Methods for Wireless Electric Vehicles," *IEEE Trans. Pow. Electron.*, vol. 29, pp. 5770-5783, 2014.

[27] H. Zhang, F. Lu, H. Hofmann, W. Liu, C. Mi, "A Six-Plate Capacitive Coupler to Reduce Electric Field Emission in Large Air-gap Capacitive Power Transfer," *IEEE Trans. Power Electron.*, 2017, doi: 10.1109/TPEL.2017.2662583.

[28] I. Ramos, K. Afridi, J. Estrada, Z. Popovic, "Near-field Capacitive Wireless Power Transfer Array with External Field Cancellation," *Proc. IEEE Wireless Power Transfer Conf.* (*WPTC*), pp. 1-4, 2016.

CHAPTER V

SAFETY ISSUE AND FOREIGN OBJECT IMPACT

5.1. Introduction

Safety is an important concern in wireless power transfer technology. It exists in both IPT and CPT systems, and is becoming a major constraint in the practical applications [1], [2]. Although it has been proven that a large amount of power can be efficiently transferred through a considerable distance, the process must be safe enough to be used in real life.

In a CPT system, there are four major safety concerns: voltage stress, electric field emissions, foreign object influence on the CPT system, and CPT system influence on a foreign object. These four aspects should be studied and resolved before CPT technology can be used in the electric vehicle charging application.

First, a CPT system usually has high voltage stresses between the metal plates [3], [4]. The CPT technology typically uses high-frequency electric fields to transfer power, and the fields must be strong enough to realize sufficient power transfer. Therefore, the voltage stresses between the metal plates are significantly increased. The high voltages can cause potential electric shock which is dangerous. Also, the voltages might exceed the breakdown limit of the dielectric material and cause arcing. Therefore, it is important to investigate the voltage stresses and provide reliable insulations.

Second, there are electric field emissions around a CPT system [5]. The electric fields in a CPT system are not constrained between the transmitter and receiver plates. There are also leakage electric fields emitted to the surrounding environment due to the fringing effect. Especially in high power and large air-gap applications, the electric field emissions are much

more severe. There are several international regulations considering human safety that limit electric field strength along a wide frequency range, such as the ICNIRP 2010 [6] and. IEEE C95.1 [7]. Since ICNIRP 2010 is more conservative, IEEE C95.1 is used more often. Although electric field emissions are unavoidable, the safe region surrounding the CPT system should be provided as the guideline for users.

Third, foreign objects, including metallic and dielectric materials, can influence the operation of a CPT system. In practical applications, the foreign object can change the coupling capacitances between the plates and affect the resonances of the circuit. The transferred power can therefore be affected. The voltages and currents on the circuit components can be dramatically increased, and might exceed the rating of the components. Therefore, the influence of foreign objects needs to be studied.

Fourth, the electric field in a CPT system could induce power loss in a foreign object, which could cause high temperatures and a potential fire hazard. Furthermore, the electric field can induce a voltage on a metallic foreign object, which can be a shock hazard. Therefore, it is meaningful to study foreign objects in a CPT system.

5.2. Voltage Stresses between Metal Plates

5.2.1. General Mathematical Model of CPT System Power

A CPT system usually contains four metal plates as a capacitive coupler. They can be horizontally arranged as in Fig. 2-1 or vertically arranged as in Fig. 3-3, and there are six coupling capacitances between every two plates. The capacitive coupler works as a two-port network connecting the transmitter and receiver sides. The fundamental working principle of a CPT system is to generate a high voltage on the transmitter plate P_1 and P_2 which can induce high voltage on the receiver plates P_3 and P_4. To realize high voltages, compensation circuits are usually required to establish resonances at both sides. The behavior source model in Fig. 4-3 is a good example to represent the capacitive coupler and illustrate the power transfer process, resulting in a general circuit topology of a CPT system as shown in Fig. 5-1.

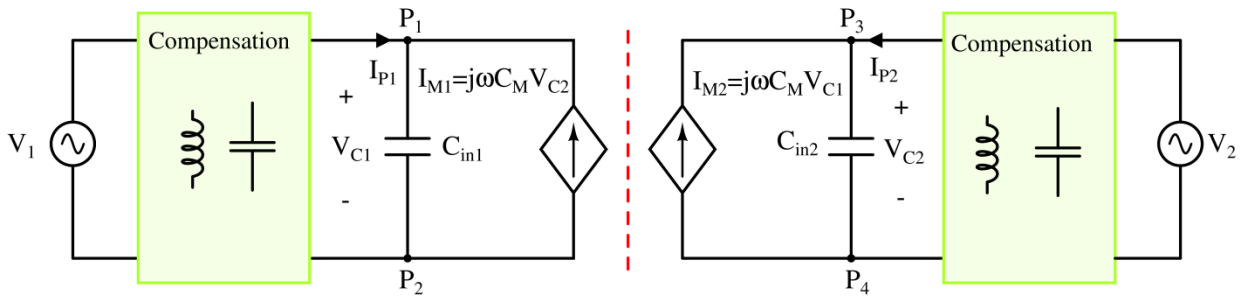

Fig. 5-1. A general circuit topology of a CPT system with behavior source model

In Fig. 5-1, the link between the two behavior sources I_{M1} and I_{M2} represent the capacitive couplings between the primary and secondary sides, in which I_{M1} is used to transfer power and I_{M2} is used to receive power. The apparent power S_{M1} absorbed by the primary current source I_{M1} is expressed as,

$$S_{M1} = V_{C1} \cdot (-I_{M1})^* = V_{C1} \cdot (-j\omega C_M V_{C2})^* \tag{5-1}$$

The real and imaginary part of S_{M1} is defined as P_{M1} and Q_{M1}, respectively. The voltage V_{C1} is chosen as the reference phasor, and the phase difference of V_{C2} is defined as θ, resulting in

$$V_{C2} = |V_{C2}| \cdot (\cos\theta + j\sin\theta) \tag{5-2}$$

Then, the apparent power S_{M1} is further expressed as,

$$S_{M1} = P_{M1} + jQ_{M1} = \omega C_M \cdot |V_{C1}| \cdot |V_{C2}| \cdot \sin\theta + j\omega C_M \cdot |V_{C1}| \cdot |V_{C2}| \cdot \cos\theta \tag{5-3}$$

Therefore, the active and reactive power absorbed by the current source I_{M1} is expressed as,

$$\begin{cases} P_{M1} = \omega C_M \cdot |V_{C1}| \cdot |V_{C2}| \cdot \sin\theta \\ Q_{M1} = \omega C_M \cdot |V_{C1}| \cdot |V_{C2}| \cdot \cos\theta \end{cases} \tag{5-4}$$

At the receiver side, the apparent power S_{M2} provided by the secondary current source I_{M2} is expressed as,

$$S_{M2} = V_{C2} \cdot I_{M2}^* = V_{C2} \cdot (j\omega C_M V_{C1})^* \tag{5-5}$$

Similarly, the real and imaginary part of S_{M2} is defined as P_{M2} and Q_{M2}, respectively. Then, the apparent power S_{M2} is further expressed as,

$$S_{M2} = P_{M2} + jQ_{M2} = \omega C_M \cdot |V_{C1}| \cdot |V_{C2}| \cdot \sin\theta - j\omega C_M \cdot |V_{C1}| \cdot |V_{C2}| \cdot \cos\theta \tag{5-6}$$

Therefore, the active and reactive power provided by the current source I_{M2} is expressed as,

$$\begin{cases} P_{M2} = \omega C_M \cdot |V_{C1}| \cdot |V_{C2}| \cdot \sin\theta \\ Q_{M2} = -\omega C_M \cdot |V_{C1}| \cdot |V_{C2}| \cdot \cos\theta \end{cases} \tag{5-7}$$

Comparing (5-1) and (5-5), the magnitude of apparent power can be expressed as,

$|S_M|=|S_{M2}|=|S_{M1}|$. Comparing (5-4) and (5-7), it can be seen that the active power absorbed by I_{M1} is equal to the active power provided by I_{M2}, which is consistent with energy conservation. Then, the active power is further defined as $P_M=P_{M1}=P_{M2}$. It also needs to be emphasized that the reactive power Q_{M1} absorbed by I_{M1} is not equal to the reactive power provided by Q_{M2}, but they are opposite to each other. Then, the reactive power is further defined as $Q_M=Q_{M1}=-Q_{M2}$. To summarize, the apparent power S_M can be illustrated in Fig. 5-2, where the x axis is the reactive power and y axis is the active power.

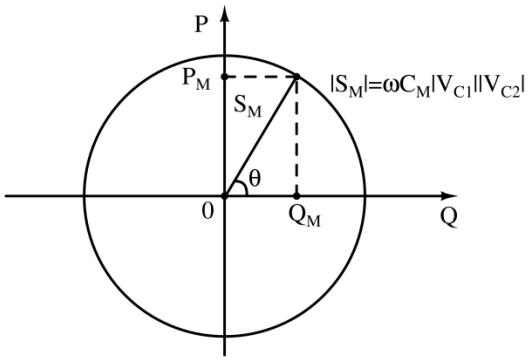

Fig. 5-2. The apparent power S_M transferred to the secondary side

Fig. 5-2 shows that when θ is in the range of (0°, 180°), $P_{M1}>0$, which means active power is transferred from the primary to secondary side. When θ is in the range of (-180°, 0°), $P_{M1}<0$ and the power transfer direction is reversed. In a CPT system design process, the active power P_M is usually fixed to satisfy the power requirement. Then, the reactive power Q_M is expressed as,

$$Q_M = P_M \cdot \cot\theta \tag{5-8}$$

The relationship between Q_M and P_M is shown in Fig. 5-3.

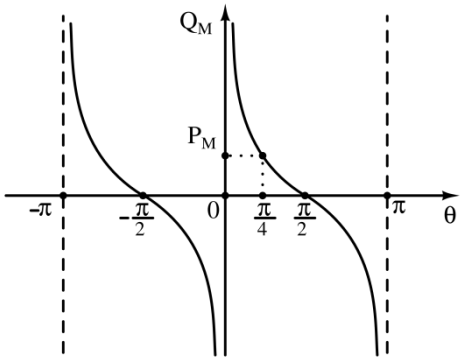

Fig. 5-3. The relationship between reactive power Q_M and active power P_M

Fig. 5-3 shows that the reactive power Q_M depends upon the phase angle θ between V_{C1} and

V_{C2}. For example, when θ=90°, Q_M=0, which means there is no reactive power transferred to the secondary side. When θ=45°, Q_M=P_M, which means the transferred reactive power is equal to the active power. When θ approaches 0°, the reactive power Q_M is dramatically increased to be much larger than the active power P_M.

According to (5-4), when the active power P_M is fixed, increasing sin(θ) can help to reduce the voltages $|V_{C1}|$ and $|V_{C2}|$. Therefore, in a practical design, θ is usually designed to be close to 90°. In this way, the reactive power circulating in the circuit is reduced to almost zero, and the corresponding conduction loss is also minimized. It needs to be clarified that the phase angle θ can be adjusted through compensation circuit design.

5.2.2. General Mathematical Model of Plate Voltages

In Fig. 5-1, voltages V_{C1} and V_{C2} are determined by the compensation circuits and the input and output voltages V_1 and V_2. To further calculate the voltages between the other plates, the six-capacitance model should be used as shown in Fig. 5-4.

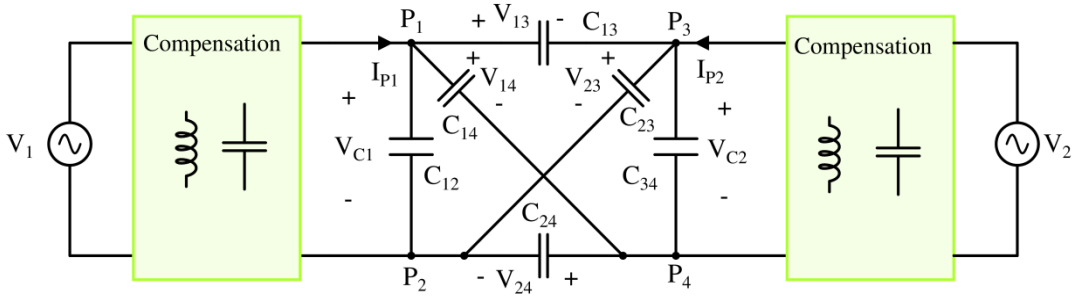

Fig. 5-4. A general circuit topology of a CPT system with six-capacitor model

The voltages between plates V_{13}, V_{24}, V_{14}, and V_{23} are expressed as,

$$\begin{cases} V_{13} = \dfrac{(C_{23}+C_{24})\cdot V_{C1} - (C_{14}+C_{24})\cdot V_{C2}}{C_{13}+C_{14}+C_{23}+C_{24}} \\ V_{24} = \dfrac{(C_{13}+C_{14})\cdot V_{C1} - (C_{13}+C_{23})\cdot V_{C2}}{C_{13}+C_{14}+C_{23}+C_{24}} \\ V_{14} = \dfrac{(C_{23}+C_{24})\cdot V_{C1} + (C_{13}+C_{23})\cdot V_{C2}}{C_{13}+C_{14}+C_{23}+C_{24}} \\ V_{23} = \dfrac{(C_{13}+C_{14})\cdot V_{C1} + (C_{14}+C_{24})\cdot V_{C2}}{C_{13}+C_{14}+C_{23}+C_{24}} \end{cases} \tag{5-9}$$

By substituting the magnitude and phase angle in (5-2), their magnitudes are expressed as,

$$\begin{cases} |V_{13}| = \dfrac{\sqrt{(C_{23}+C_{24})^2\cdot|V_{C1}|^2+(C_{14}+C_{24})^2\cdot|V_{C2}|^2-2(C_{23}+C_{24})(C_{14}+C_{24})\cdot|V_{C1}|\cdot|V_{C2}|\cos\theta}}{C_{13}+C_{14}+C_{23}+C_{24}} \\ |V_{24}| = \dfrac{\sqrt{(C_{13}+C_{14})^2\cdot|V_{C1}|^2+(C_{13}+C_{23})^2\cdot|V_{C2}|^2-2(C_{13}+C_{14})(C_{13}+C_{23})\cdot|V_{C1}|\cdot|V_{C2}|\cos\theta}}{C_{13}+C_{14}+C_{23}+C_{24}} \\ |V_{14}| = \dfrac{\sqrt{(C_{23}+C_{24})^2\cdot|V_{C1}|^2+(C_{13}+C_{23})^2\cdot|V_{C2}|^2+2(C_{23}+C_{24})(C_{13}+C_{23})\cdot|V_{C1}|\cdot|V_{C2}|\cos\theta}}{C_{13}+C_{14}+C_{23}+C_{24}} \\ |V_{23}| = \dfrac{\sqrt{(C_{13}+C_{14})^2\cdot|V_{C1}|^2+(C_{14}+C_{24})^2\cdot|V_{C2}|^2+2(C_{13}+C_{14})(C_{14}+C_{24})\cdot|V_{C1}|\cdot|V_{C2}|\cos\theta}}{C_{13}+C_{14}+C_{23}+C_{24}} \end{cases} \tag{5-10}$$

In a capacitive coupler, the most important capacitive couplings are P_1-P_3 and P_2-P_4, which are between the transmitter and receiver and defined as the main couplings. The voltages between these plates produce significant emissions, which means the voltage magnitude $|V_{13}|$ and $|V_{24}|$ need to be minimized. According to the power equation (5-4) and the voltage magnitude in (5-10), if $|V_{C1}|$ and $|V_{C2}|$ satisfy,

$$|V_{C1}| = \sqrt{\frac{C_{14}+C_{24}}{C_{23}+C_{24}}}\cdot\sqrt{\frac{P_M}{\omega C_M\sin\theta}},\quad |V_{C2}| = \sqrt{\frac{C_{23}+C_{24}}{C_{14}+C_{24}}}\cdot\sqrt{\frac{P_M}{\omega C_M\sin\theta}} \tag{5-11}$$

then, $|V_{13}|$ can reach its minimum value, which is expressed as

$$|V_{13}|_{\min} = \frac{\sqrt{2(C_{23}+C_{24})(C_{14}+C_{24})}}{C_{13}+C_{14}+C_{23}+C_{24}}\cdot\sqrt{\frac{P_M}{\omega C_M}}\cdot\sqrt{\frac{1-\cos\theta}{\sin\theta}} \tag{5-12}$$

Also, if $|V_{C1}|$ and $|V_{C2}|$ satisfy,

$$|V_{C1}| = \sqrt{\frac{C_{13}+C_{23}}{C_{13}+C_{14}}}\cdot\sqrt{\frac{P_M}{\omega C_M\sin\theta}},\quad |V_{C2}| = \sqrt{\frac{C_{13}+C_{14}}{C_{13}+C_{23}}}\cdot\sqrt{\frac{P_M}{\omega C_M\sin\theta}} \tag{5-13}$$

then, $|V_{24}|$ can reach its minimum value, which is expressed as

$$|V_{24}|_{\min} = \frac{\sqrt{2(C_{13}+C_{14})(C_{13}+C_{23})}}{C_{13}+C_{14}+C_{23}+C_{24}}\cdot\sqrt{\frac{P_M}{\omega C_M}}\cdot\sqrt{\frac{1-\cos\theta}{\sin\theta}} \tag{5-14}$$

In a capacitive coupler, according to the structure in Fig. 2-1 and Fig. 3-3, the cross couplings P_1-P_4 and P_2-P_3 are usually small, which means $C_{14}<<C_{13}$, $C_{14}<<C_{24}$, $C_{23}<<C_{13}$, and $C_{23}<<C_{24}$. Then, approximately, (5-11) and (5-13) can be satisfied at the same time, which is expressed as,

$$|V_{C1}| = |V_{C2}| = \sqrt{\frac{P_M}{\omega C_M\sin\theta}} \tag{5-15}$$

Then, $|V_{13}|$ and $|V_{24}|$ can both reach their minimum values simultaneously. To summarize, the six voltages in a capacitive coupler are expressed in Table V-1.

Table V-1. Voltages between metal plates

$\lvert V_{C1}\rvert = \sqrt{\dfrac{P_M}{\omega C_M \sin\theta}}$	$\lvert V_{13}\rvert = \dfrac{C_{24}}{C_{13}+C_{24}} \cdot \sqrt{\dfrac{2P_M}{\omega C_M}} \cdot \sqrt{\dfrac{1-\cos\theta}{\sin\theta}}$	$\lvert V_{14}\rvert = \dfrac{\sqrt{C_{24}^2 + C_{13}^2 + 2C_{13}C_{24}\cos\theta}}{C_{13}+C_{24}} \cdot \sqrt{\dfrac{P_M}{\omega C_M \sin\theta}}$
$\lvert V_{C2}\rvert = \sqrt{\dfrac{P_M}{\omega C_M \sin\theta}}$	$\lvert V_{24}\rvert = \dfrac{C_{13}}{C_{13}+C_{24}} \cdot \sqrt{\dfrac{2P_M}{\omega C_M}} \cdot \sqrt{\dfrac{1-\cos\theta}{\sin\theta}}$	$\lvert V_{23}\rvert = \dfrac{\sqrt{C_{13}^2 + C_{24}^2 + 2C_{13}C_{24}\cos\theta}}{C_{13}+C_{24}} \cdot \sqrt{\dfrac{P_M}{\omega C_M \sin\theta}}$

If the capacitive coupler is symmetric, C_{13}=C_{24}. The voltages between plates are then further simplified as shown in Table V-2.

Table V-2. Simplified voltages between metal plates in a symmetric coupler

$\lvert V_{C1}\rvert = \lvert V_{C2}\rvert = \sqrt{\dfrac{P_M}{\omega C_M \sin\theta}}$	$\lvert V_{13}\rvert = \lvert V_{24}\rvert = \dfrac{\sqrt{2}}{2} \cdot \sqrt{\dfrac{P_M}{\omega C_M}} \cdot \sqrt{\dfrac{1-\cos\theta}{\sin\theta}}$	$\lvert V_{14}\rvert = \lvert V_{23}\rvert = \dfrac{\sqrt{2}}{2} \cdot \sqrt{\dfrac{P_M}{\omega C_M}} \cdot \sqrt{\dfrac{1+\cos\theta}{\sin\theta}}$

A 3.0 kW CPT system is used as an example to illustrate the voltage stresses as shown in Fig. 5-5, where switching frequency is set to be 1 MHz.

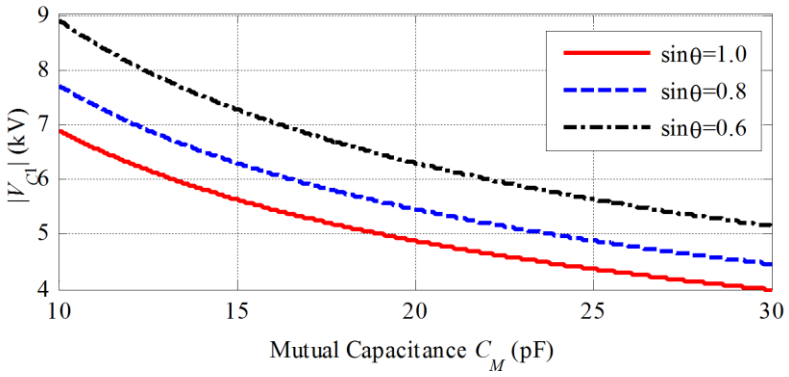

(a) Voltage $|V_{C1}|$

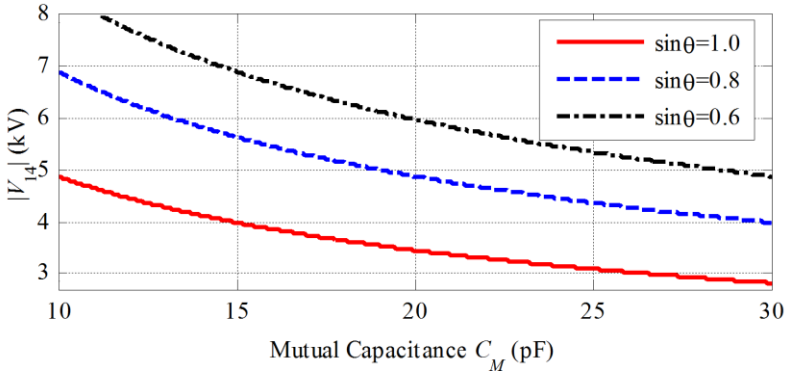

(b) Voltage $|V_{14}|$

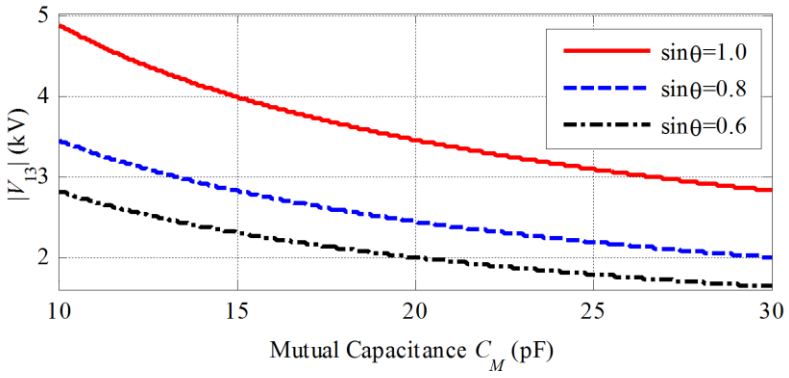

(c) Voltage $|V_{13}|$

Fig. 5-5. Calculated voltage stresses between metal plates when P_M=3.0 kW and f_{sw}=1MHz

Fig. 5-5 shows that and the voltages are in the kV level in this 3.0 kW CPT system. Therefore, it is important to provide reliable insulation on the plates to avoid electric shock. It also shows that increasing C_M is effective for reducing all the three voltages $|V_{C1}|$, $|V_{14}|$ and $|V_{13}|$. Increasing sin(θ) can help to reduce $|V_{C1}|$ and $|V_{14}|$, but it increases $|V_{13}|$.

5.2.3. Plate Voltages in an LCLC-Compensated CPT System

Using the behavior source model of the capacitive coupler, the circuit topology of a double-sided LCLC-compensated CPT system is shown in Fig. 5-6.

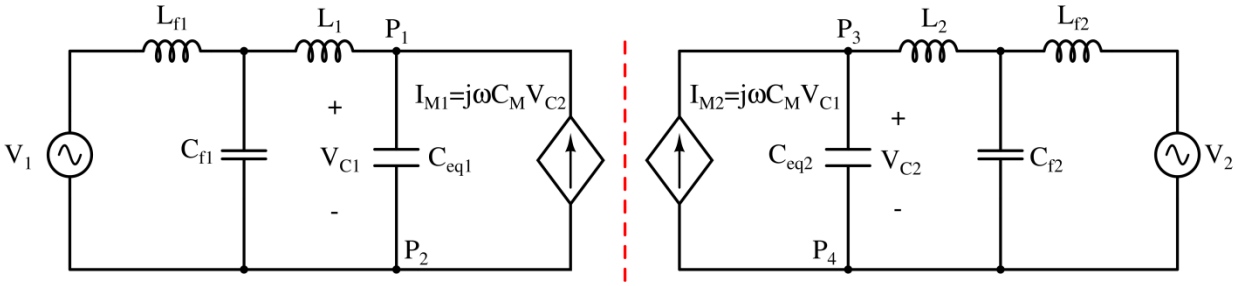

Fig. 5-6. Circuit topology of an LCLC-compensated CPT system with behavior source model

According to the circuit analysis in Chapter II, the voltages V_{C1} and V_{C2} are expressed as,

$$\begin{cases} V_{C1} = \dfrac{C_{f1}}{(1-k_C^2)\cdot C_{eq1}}\cdot|V_1| + j\cdot\dfrac{C_{f2}C_M}{(1-k_C^2)\cdot C_{eq1}C_{eq2}}\cdot|V_2| \\ V_{C2} = \dfrac{C_{f1}C_M}{(1-k_C^2)\cdot C_{eq1}C_{eq2}}\cdot|V_1| + j\cdot\dfrac{C_{f2}}{(1-k_C^2)\cdot C_{eq2}}\cdot|V_2| \end{cases} \tag{5-16}$$

Then, the phase difference θ between V_{C1} and V_{C2} is calculated as,

$$\theta = 90^\circ - \arctan\left(\frac{C_{f1}C_M}{C_{f2}C_{eq1}}\cdot\frac{|V_1|}{|V_2|}\right) - \arctan\left(\frac{C_{f2}C_M}{C_{f1}C_{eq2}}\cdot\frac{|V_2|}{|V_1|}\right) \tag{5-17}$$

If the parameters in the circuit are designed to be symmetric, which means $|V_1|=|V_2|$, $C_{f1}=C_{f2}$, and $C_{eq1}=C_{eq2}$, the voltages are simplified as,

$$\begin{cases} V_{C1} = \dfrac{C_{f1}}{(1-k_C^2)\cdot C_{eq1}} \cdot |V_1| \cdot (1 + j \cdot k_C) \\ V_{C2} = \dfrac{C_{f1}}{(1-k_C^2)\cdot C_{eq1}} \cdot |V_1| \cdot (k_C + j) \end{cases} \tag{5-18}$$

The phase difference θ between V_{C1} and V_{C2} is then calculated as,

$$\theta = 90^\circ - 2\arctan(k_C) \tag{5-19}$$

According to (5-19), the phase difference θ and sin(θ) are illustrated in Fig. 5-7.

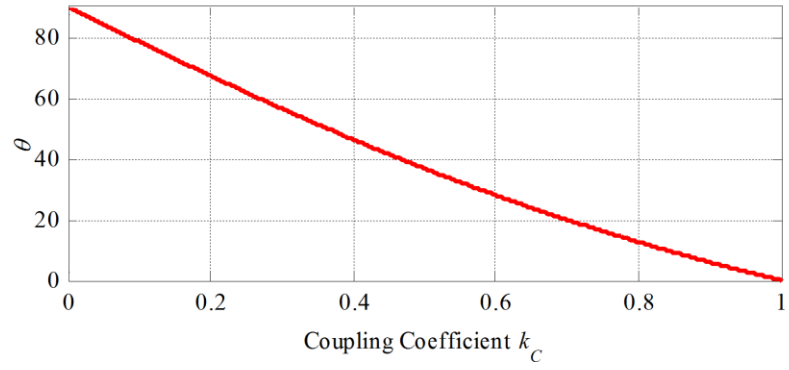

(a) Phase different θ

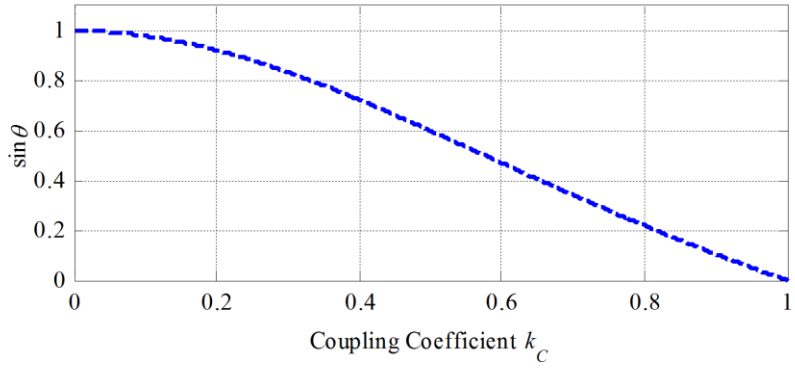

(b) Values of sin(θ)

Fig. 5-7. Phase different θ and sin(θ) at different k_C in LCLC-Compensated CPT system

In a practical CPT system, the capacitive coupling coefficient k_C is usually in the range of (0, 0.30). Fig. 5-7(a) shows that θ is in the range of (56.6°, 90°) and Fig. 5-7(b) shows that the corresponding sin(θ) is very close to 1.0 and in the range of (0.84, 1.0), which means the LCLC compensation circuit can achieve a relative high value of sin(θ).

Therefore, considering the sin(θ) term in the power equations in (5-4), it can be concluded that the LCLC compensation circuit can help maximize the active power P_M transferred to the secondary side, and it can also reduce the reactive power Q_M circulating in the circuit. The system efficiency can be improved. Moreover, considering the sin(θ) term in the voltage expressions in Table V-2, it can be further concluded that the LCLC compensation circuit can also help to reduce the voltages $|V_{C1}|$ and $|V_{14}|$.

The double-sided LCLC-compensated CPT system designed in Chapter II is used as an example to calculate the voltage stresses between plates. According to the circuit parameters in Table II-2, the capacitive coupler achieves C_M=18.4 pF and k_C=0.15. Then, the relationships in Fig. 5-7 show that θ=73° and sin(θ)=0.956. Based on the expressions in Table V-2, the calculated voltages between plates are shown in Fig. 5-8.

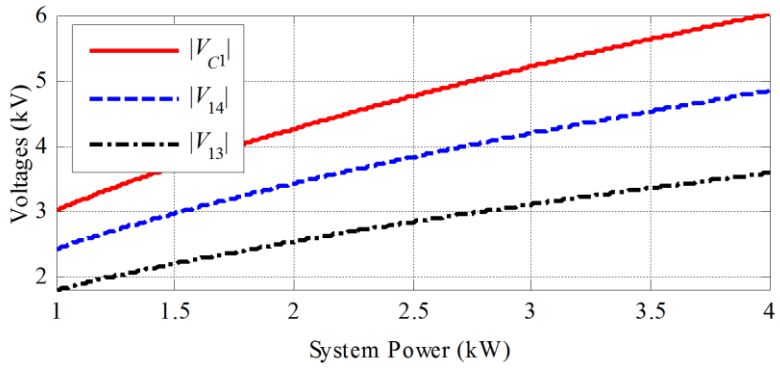

Fig. 5-8. Calculated voltages in an LCLC-compensated CPT system when C_M=18.4 pF and k_C=0.15

When the system power is 3.0 kW, the calculated voltages between plates are $|V_{C1}|=|V_{C2}|$=5.2 kV, $|V_{14}|=|V_{23}|$=4.2 kV, and $|V_{13}|=|V_{24}|$=3.1 kV. Considering the dimensions of the capacitive coupler in Fig. 2-1, the distance between the same-side plates is 500 mm, and the voltage difference is 5.2 kV. The air-gap distance between the transmitter and receiver plates is 150 mm, and the voltage difference is 3.1 kV. Since the breakdown voltage of dry air is about 3.0 kV/mm [8] and its variation with respect to different humidity conditions is within ±25% [9], there is no concern of arcing between plates in this coupler. In the compensation circuit, there are capacitors connected with the plates, and their voltages are also in the kV level, which means multiple capacitors should be connected in series to increase the equivalent voltage rating.

5.3. Electric Field Emissions

5.3.1. Electric Fields Emission of Horizontal Plates

The high voltages between the plates are used to establish electric fields to transfer power. The previous analysis shows that the voltage stresses are increased to the kV level to achieve kW-level power transfer. Higher power requires higher voltages. However, the electric fields are not confined between metal plates in long-distance applications. There are leakage electric field emissions to the surrounding area.

When 3.0 kW power is transferred using the horizontal capacitive coupler in Chapter II, The voltage between the plates are $|V_{C1}|=|V_{C2}|$=5.2 kV, $|V_{14}|=|V_{23}|$=4.2 kV, and $|V_{13}|=|V_{24}|$=3.1 kV. With these voltages, Maxwell is used to simulate the electric fields around the capacitive coupler. The electric field distributions in the *xy*, *yz*, and *xz* planes are shown in Fig. 5-9.

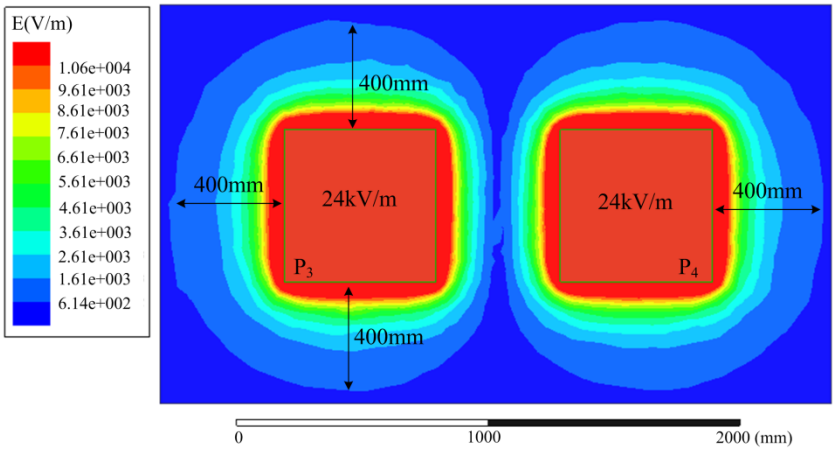

(a) *xy* plane

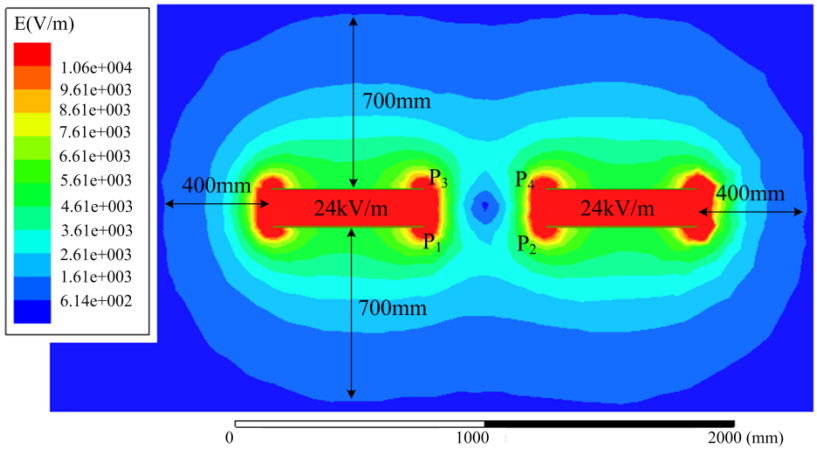

(b) *yz* plane

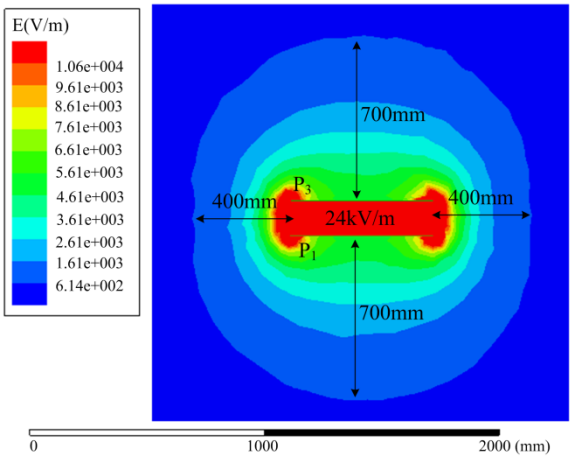

(c) *xz* plane

Fig. 5-9. Electric field emission of a horizontal capacitive coupler

According to IEEE C95.1 standard [7], the electric field strength should be limited below 614V/m for human safety. The simulation in Fig. 5-9 shows that the electric field strength increases rapidly when approaching the capacitive coupler. The safe range is 400 mm away from the side, and 700 mm away from the top and bottom of the coupler. The maximum field strength between the plates can reach 24kV/m.

The direction of the electric field vector (E vector) in the *yz* plane is used to show how the electric field emissions are generated in the capacitive coupler. The electric field vector distribution around the coupler is shown in Fig. 5-10.

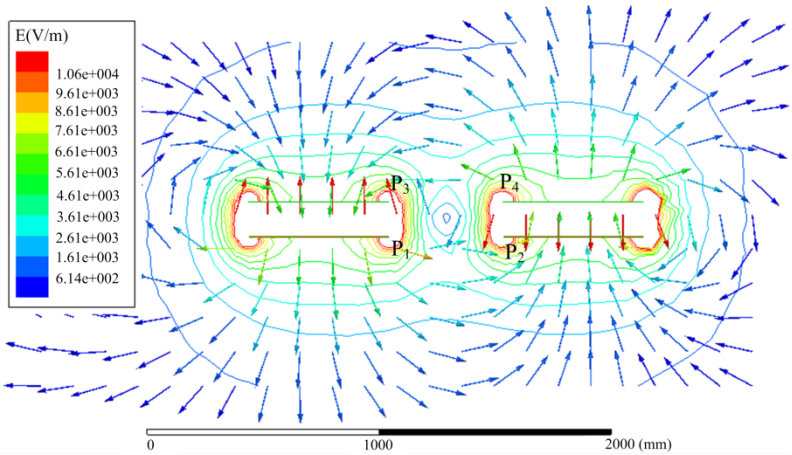

Fig. 5-10. Electric field vector distribution in a horizontal capacitive coupler when P_M=3.0 kW

The shape of the E vector indicates a dipole structure, in which P_1-P_3 act as one pole and P_2-P_4 act as the other pole. The E vector indicates that the electric flux goes from one plate to the

adjacent plates. Since the air-gap between the transmitter and receiver is large, the electric flux can easily escape from the air-gap and cause significant electric field emissions. At the primary side, the voltage difference between P_1 and P_2 is also large, and the electric flux from P_1 needs to travel a much longer distance than the air-gap to arrive P_2, which causes larger electric field emissions at the bottom of the coupler. At the secondary side, the electric flux from P_4 to P3 causes similar emission problem on the top of the coupler.

The electric field emissions are also simulated in misalignment cases, as shown in Fig. 5-11.

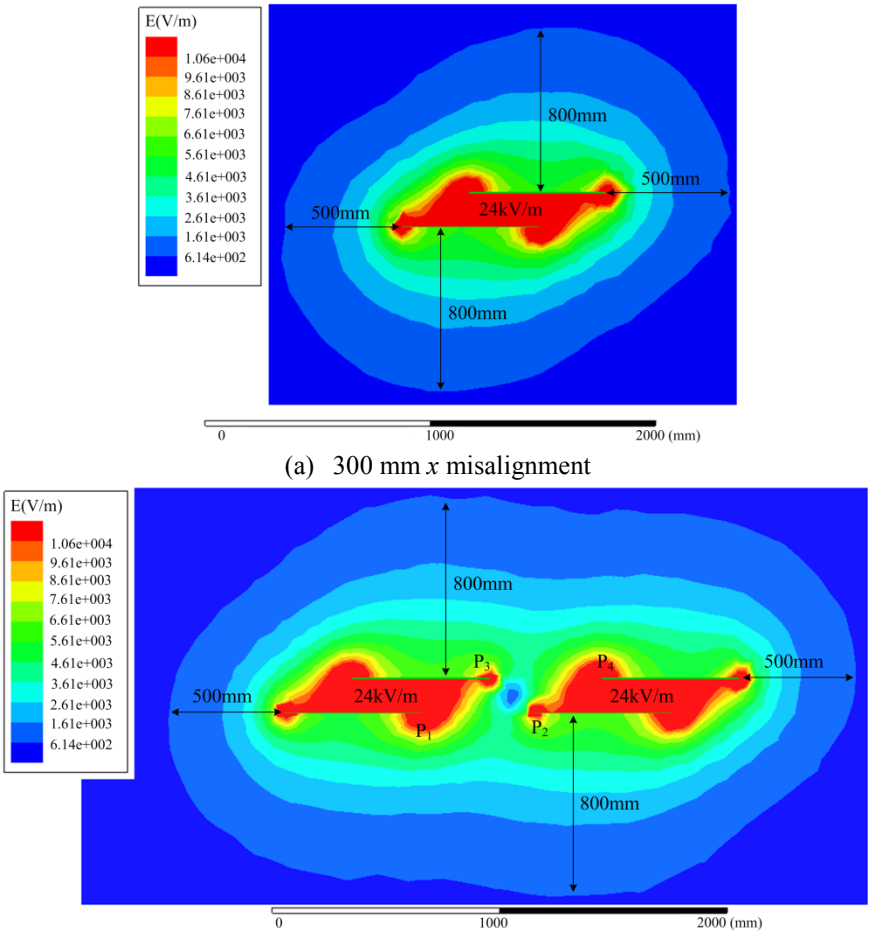

(a) 300 mm *x* misalignment

(b) 300 mm *y* misalignment

Fig. 5-11. Electric field emission of a horizontal coupler at misalignment cases

In the simulation, the same voltage excitations are applied to the plates as in the well-aligned case. When there is 300 mm *x* or *y* direction misalignment, more electric flux escapes from the capacitive coupler. The safe range is now 500 mm away from the side, and 800 mm away from the top and bottom of the capacitive coupler.

5.3.2. Electric Field Emissions of Vertical Plates

The vertical structure of the capacitive coupler introduced in Chapter III is used as another example to study electric field emissions. Based on the coupler structure shown in Fig. 3-3, to achieve comparable power density with the aforementioned horizontal coupler, the dimensions are chosen as l_1=914 mm, l_2=695 mm, d_c=50 mm, and d=150 mm, which realizes C_{13}=C_{24}. According to the behavior source model in Fig.4-3 and (4-2), the equivalent parameters are simulated as C_M=11.2 pF and k_C=0.094. Then, using the expressions in Table V-2, the voltages between plates are calculated and shown in Fig. 5-12.

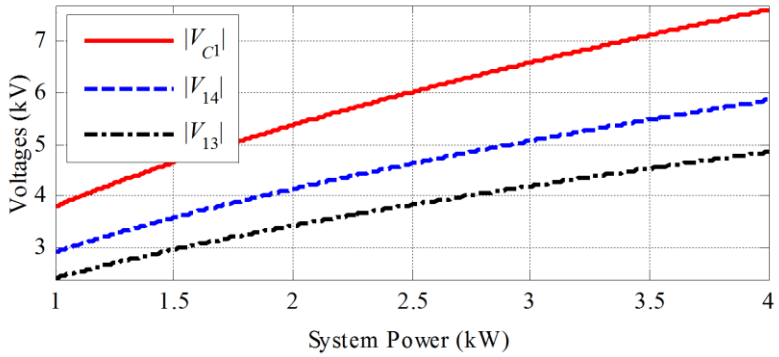

Fig. 5-12. Calculated voltages in an LCLC-compensated CPT system when C_M=11.2 pF and k_C=0.094

In Fig. 5-12, When 3.0 kW power is transferred using the designed vertical coupler, the voltages between plates are calculated as $|V_{C1}|$=$|V_{C2}|$=6.7 kV, $|V_{14}|$=$|V_{23}|$=5.1 kV, and $|V_{13}|$=$|V_{24}|$=4.2 kV. Using these voltages as excitations, the electric field emissions around the vertical coupler are simulated as shown in Fig. 5-13.

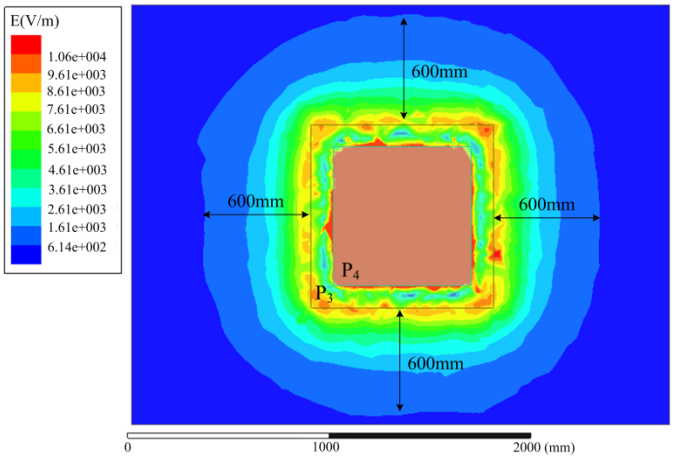

(a) *xy* plane

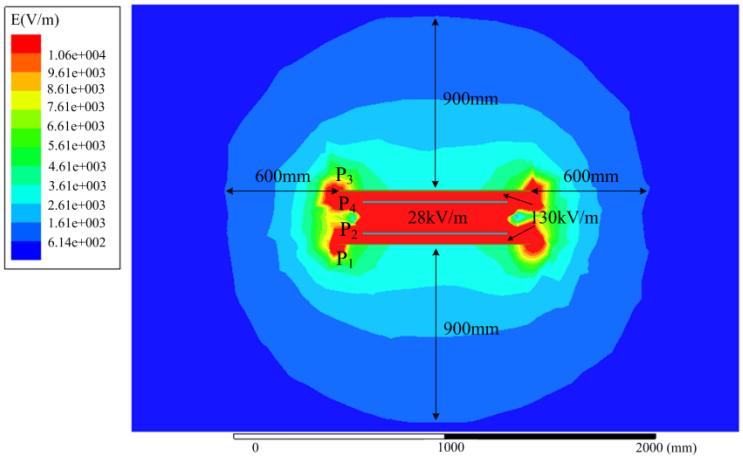

(b) *yz* plane

Fig. 5-13. Electric field emission of a vertical coupler

Fig. 5-13 shows the electric field distribution in *xy* and *yz* planes. Because of the symmetry of the vertical coupler structure, the *xz* plane is the same as the *yz* plane. The simulation shows that the maximum electric field strength between the same side plates is 130kV/m and the electric field strength in the air-gap between the transmitter and receiver is 28kV/m. Since the breakdown field strength of dry air is 3 kV/mm [8] and its variation with humidity is within ±25% [9], the plate distances are large enough to avoid arcing. Considering the limitation of 614V/m in Fig. 5-13, it shows that the safe range is 600 mm away from the side, and 900 mm away from the top and bottom of the vertical coupler. Because the vertical structure is more compact and the plate voltages are higher, the electric field emissions are more severe.

The E vector distribution in the vertical coupler is also simulated as shown in Fig. 5-14.

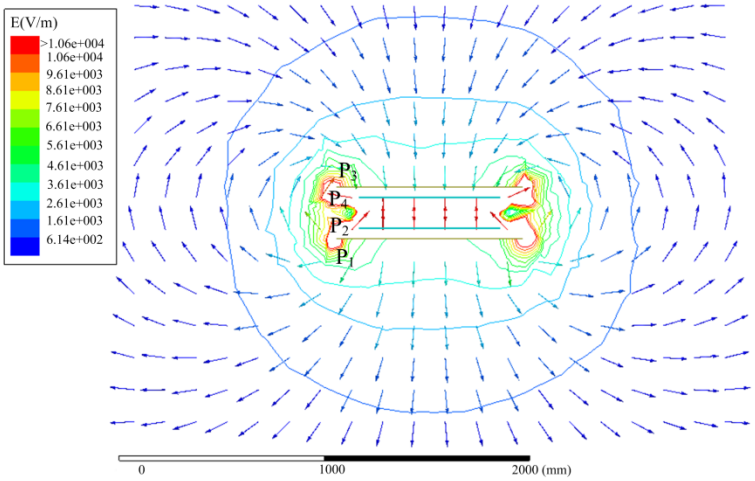

Fig. 5-14. Electric field vector distribution in a vertical capacitive coupler when P_M=3.0 kW

In a vertical capacitive coupler, four plates are arranged in a line, and the shape of E vector indicates a unipolar structure. The larger plates P_1 and P_3 are placed at the outer side of the coupler, and they contribute more to the electric field emissions. Compared to the horizontal coupler, the voltages between plates are increased and the distance between P_1 and P_3 is increased. Therefore, there are more leakage electric fluxes from the air gap.

The electric field emission at 300 mm *x* misalignment is also studied as shown in Fig. 5-15.

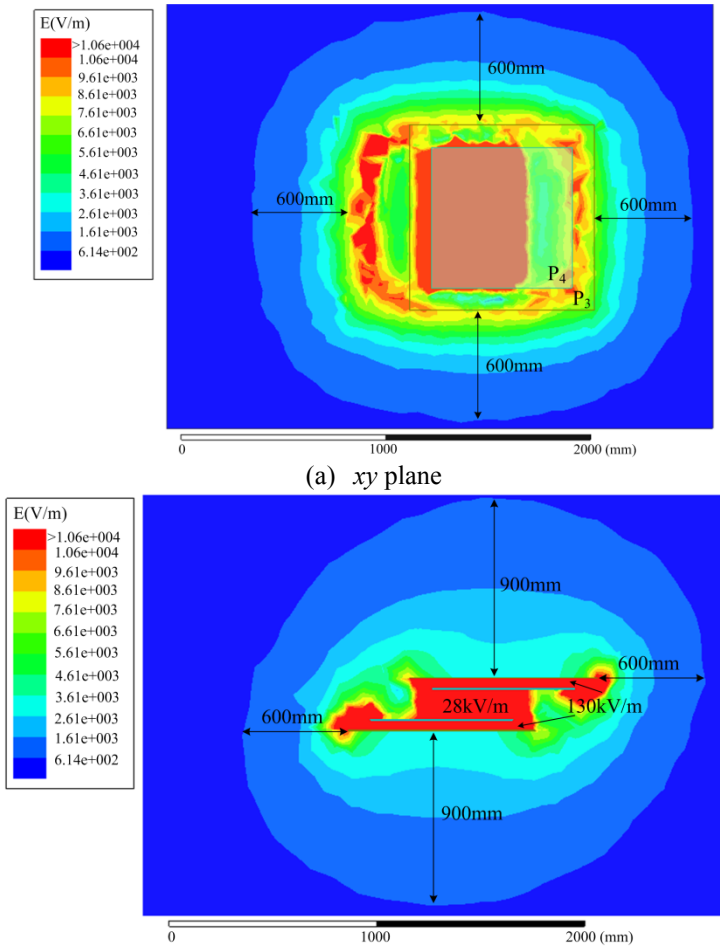

Fig. 5-15. Electric field emission of a vertical coupler at 300 mm *x* misalignment

Since the coupler structure is the same from the *x* and *y* direction, only the *x* misalignment performance is simulated. Compared to the well-aligned case in Fig. 5-13(a), when there is 300 mm misalignment, the electric field distribution is changed. The safe range is still 600 mm away from the side and 900 mm away from the top and bottom of the vertical coupler.

The horizontal and vertical structure can be combined together to reduce the electric field emissions, resulting in a six-plate capacitive coupler [5]. Two additional large plates P_5 and P_6 can be used to cover the capacitive coupler from top and bottom. When the transferred power is also 3.0 kW, the simulated electric field emissions are shown in Fig. 5-16.

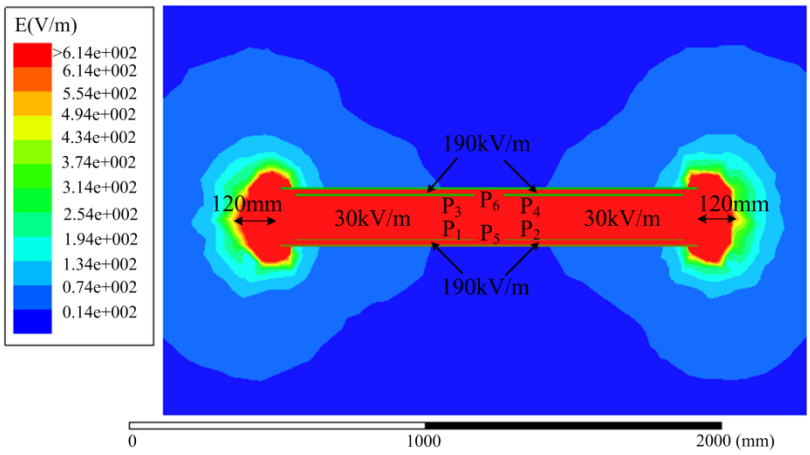

Fig. 5-16. Electric field emissions of a six-plate coupler when P_M=3.0kW

In a six-plate coupler, plates P_1, P_2, P_3, and P_4 are directly connected to the circuit components as a conventional four-plate coupler, and the shielding plates P_5 and P_6 are left floating. Due to the symmetry of the coupler structure, the voltage potentials on the two shielding plates are the same [5]. Therefore, if the transmitter side plate P_5 is grounded, the receiver side plate P_6 is equivalently grounded. In this way, these two additional plates act as a shielding box to the four active plates P_1, P_2, P_3, and P_4. Compared to Fig. 5-9 and 5-13, the electric fields in Fig. 5-16 between the air-gap are much stronger, which means most of the electric fields are concentrated between the air-gap, and the leakage electric fields outside the air-gap are significantly reduced.

Fig. 5-16 also shows that the safe range of a 3.0 kW six-plate coupler is about 120 mm away from the edge of the coupler. Even in the 300 mm misalignment case, further study in [5] shows that the safety range is about 400 mm away from the coupler. In the electric vehicle charging application the vehicle chassis can act as the plate P_6 to simplify the system structure. When plate P_5 is grounded, the vehicle chassis is then equivalently grounded, which reduces both the electric field emissions and voltage potential of the vehicle.

5.4. Foreign Object Influence to CPT System

In practical applications, it is common for foreign objects to exist in the vicinity of a capacitive coupler, which can be metallic or dielectric objects. The appearance of foreign objects can influence the coupling capacitances in the capacitive coupler and the corresponding circuit behavior in the CPT system.

5.4.1. Position of Foreign Objects

The influence of a foreign object relates to its position around the capacitive coupler. A horizontal capacitive coupler, consisting of two pairs of metal plates, is used as an example. There are eleven typical positions for a foreign object to appear, as shown in Fig. 5-17.

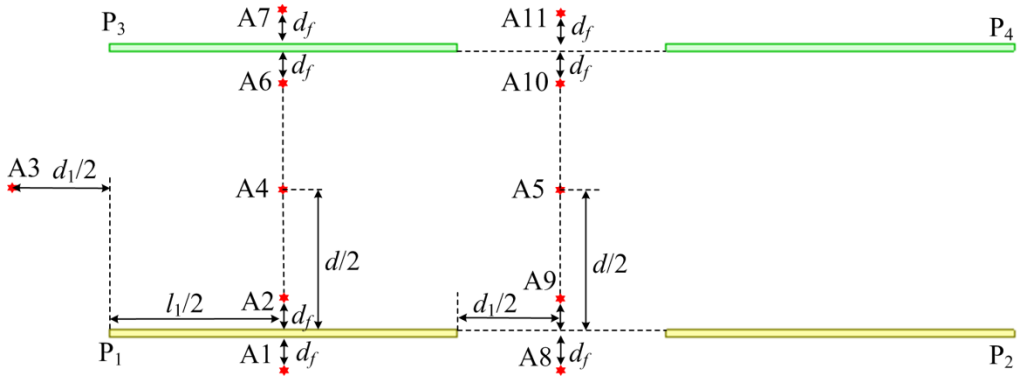

Fig. 5-17. Typical positions of a foreign object in a horizontal coupler

The eleven positions are symmetric, and so only seven of them need to be analyzed, in which positions A1-A5, A8, and A9 are used as examples. Positions A1 and A2 are close to the surface of P_1, and the distance to P_1 is defined as d_f. Position A3 is outside of the plates and its distance to plates is set to be $d_1/2$. Position A4 is in the middle between plates P_1 and P_3. Position A5 is in the center of the coupler. Positions A8 and A9 are in the middle of plates P_1 and P_2.

The plate length is defined as l_1, the air-gap distance is d, and the distance between two pairs of plates is defined as d_1. To be consistent with previous design, the parameters are chosen as l_1=610 mm, d=150 mm, d_1=100 mm, and the plate thickness is 2 mm. Considering the insulation layer, packaging, and the air-gap between the foreign object and P_1, d_f is set at 10 mm.

5.4.2. Metallic Foreign Object Influence to CPT System

A piece of iron, aluminum, or copper, can be used as an example of metallic object. In this analysis, an aluminum plate is selected. Three different sizes of the foreign aluminum plate are studied: 152.5mm×152.5mm, 305mm×305mm, 610mm×610mm. Since the thickness of a foreign metal plate is usually much smaller than the air-gap distance, the influence of thickness to the coupling capacitance can be neglected and it is chosen to be 2 mm in this analysis.

The behavior source model in Fig. 4-3 is used to analyze the capacitive coupler, and all the coupling capacitances between plates are included. Maxwell is further used to simulate the coupling capacitances, and equation (4-2) is used to calculate the equivalent capacitances C_{in1}, C_{in2}, and C_M. When there is no foreign object, the equivalent capacitances are C_{in1}=C_{in2}=27.7pF and C_M=12.5 pF. Compared to the horizontal coupler in Fig. 2-1, C_M is reduced because of the cross couplings. When the foreign aluminum plate appears and its size and position varies, the Maxwell-simulated equivalent capacitances are shown in Table V-3.

Table V-3. Influence of foreign aluminum plate to equivalent capacitances

Size	152.5mm×152.5mm			305mm×305mm			610mm×610mm		
Capacitance / Position	C_{in1}	C_{in2}	C_M	C_{in1}	C_{in2}	C_M	C_{in1}	C_{in2}	C_M
A1-A4	27.7 pF	27.7 pF	12.5 pF	27.7 pF	27.7 pF	12.5 pF	27.7 pF	27.7 pF	12.5 pF
A5	28.0 pF	28.0 pF	12.2 pF	29.0 pF	29.0 pF	11.2 pF	33.0 pF	33.0 pF	7.5 pF
A8	30.6 pF	27.7 pF	12.5 pF	44.1 pF	27.7 pF	12.5 pF	99.4 pF	27.7 pF	12.5 pF
A9	30.9 pF	27.7 pF	12.4 pF	44.2 pF	27.7 pF	11.6 pF	97.4 pF	28.0 pF	8.0 pF

Table V-3 shows that the equivalent capacitances in the capacitive coupler relates to both the size and position of the foreign aluminum plate. When its size is small (152.5mm×152.5mm), its influence on the capacitances is small. When the foreign aluminum plate is close to one pair of plates (positions A1-A7, except A5), its influence on the capacitances can be neglected. In these cases, the foreign aluminum plate also has no influence to the electric field emissions of the coupler, as shown in Fig. 5-18.

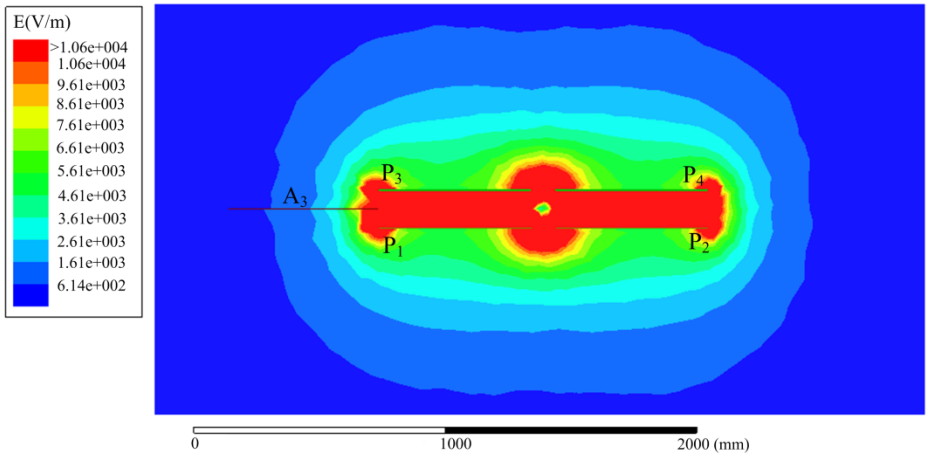

Fig. 5-18. Electric field emissions of a horizontal coupler with a 610mm×610mm aluminum plate at position A3

Fig. 5-18 shows the simulation of electric field emissions in a horizontal coupler with a 610mm×610mm aluminum plate at position A3. It indicates that the electric field is still symmetric and not affected by the foreign object.

When the aluminum plate is large enough and placed close to two same-side plates (position A8, A9, A10 and A11), Table V-3 shows that the self-capacitances C_{in1} and C_{in2} of the primary and secondary sides can be significantly increased. In these cases, the circuit might lose resonance and the power transfer process can be affected.

In electric vehicle charging applications, plates P_1 and P_2 are placed on the ground side. Since the earth ground is a good conductor, it can act as a foreign object that increases C_{in1}. Plates P_3 and P_4 are installed on the vehicle side and the chassis can increase C_{in2}. In the circuit parameter design, as long as these capacitance variations are included, the resonances in the circuit can still be maintained and effective power transfer can be realized. Reference [5] introduces this six-plate capacitive coupler structure and analyzes the working principle. Due to the symmetry of this coupler structure, both the electric field emissions and voltage potential on the chassis are significantly reduced. It needs to be emphasized that this six-plate structure is effective at eliminating the influence of a foreign object at positions A8 and A11, but cannot mitigate the influence of objects at the positions A9 and A10.

When a large aluminum plate is placed close to all four plates (positions A5 and A9), Table V-3 shows that the mutual capacitance C_M can be significantly decreased. This is because the

cross couplings P_1-P_3 and P_2-P_4 are enhanced by the foreign aluminum plate. As a result, the resonance in the circuit can also be affected, and the system power level is therefore reduced.

As a conclusion, in a horizontal capacitive coupler, a small-size metallic foreign object does not significantly affect the normal working of a CPT system. However, a large-size metallic foreign object between the two pairs of plates can have a significant influence to the coupling capacitances and the corresponding working process of the CPT system.

5.4.3. Dielectric Foreign Object Influence to CPT System

We also consider the case of a dielectric foreign object around the capacitive coupler, and two typical positions A2 and A9 are selected as examples. When a dielectric foreign object appears at position A2, the dimensions are shown in Fig. 5-19.

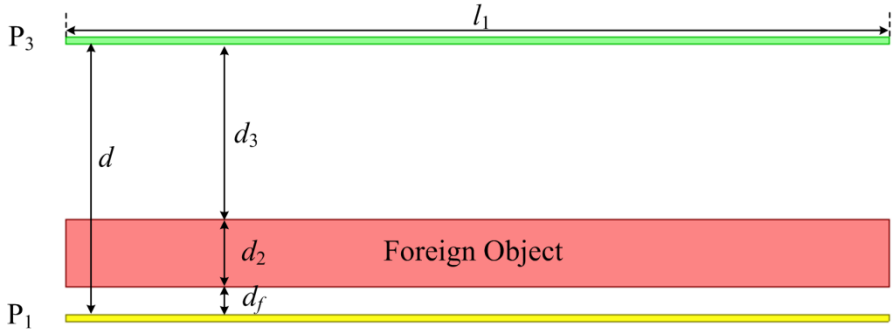

Fig. 5-19. A dielectric foreign object at position A2 around a capacitive coupler

In Fig. 5-19, the dielectric foreign object has the same length as the plates. In a practical application, compared to the aforementioned metallic foreign object, it is common to have a much thicker dielectric foreign object. The total air-gap distance between two plates is d, the thickness of a dielectric foreign object is defined as d_2, and the remaining distance between the foreign object to the upper plate P_3 is defined as d_3.

According to Fig. 2-2 in chapter II, the capacitance between P_1 and P_3 is defined as C_{M1}. With the appearance of a dielectric foreign object, C_{M1} is equivalent to two series capacitances: one is determined by the air and the other is determined by the dielectric foreign object. Since the relative permittivity (ε_r) of a dielectric object is usually larger than that of air (1.0), C_{M1} can be increased. According to the empirical formula in [10], C_{M1} is approximated to be,

$$C_{M1} = \varepsilon_0 \cdot \frac{l_1^2}{(d_3 + d_f + d_2/\varepsilon_r)} \cdot \left[1 + 2.343 \times \left(\frac{d}{l_1}\right)^{0.891}\right] \tag{5-20}$$

In (5-20), when there is no dielectric foreign object (ε_r=1), the capacitance is consistent with (2-2) in chapter II. When there is a dielectric foreign object (ε_r>1), the capacitance is increased.

Maxwell is then used to simulate the coupling capacitance at different thicknesses and materials of the dielectric foreign object. In the simulation, l_1=610mm and d=150mm, and d_f=10mm. The Maxwell-simulated capacitance C_{M1} between the plates is shown in Fig. 5-20.

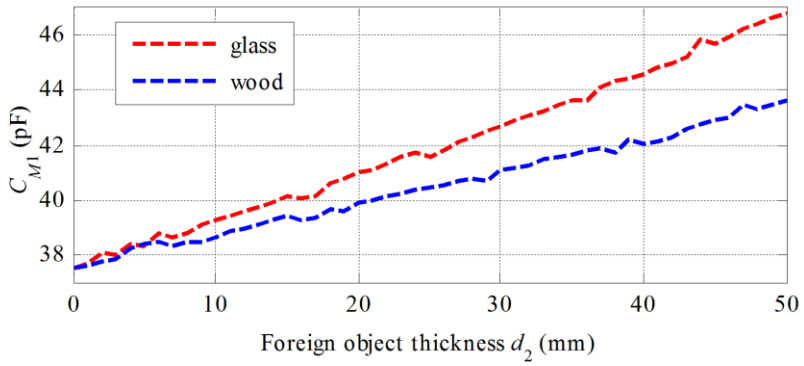

Fig. 5-20. Maxwell-simulated capacitance C_{M1} with dielectric foreign objects

Fig. 5-20 validates that C_{M1} is increased by a dielectric foreign object. There are two common objects analyzed: glass and wood. Their relative permittivity is selected to be 5.5 and 2.5, respectively. It can be seen that C_{M1} increases with increasing permittivity and thickness of the dielectric foreign object. It needs to be noticed that this increasing capacitance can affect the resonance of the circuit and affect the transferred power.

When a dielectric foreign object appears at position A9, it has an influence on both pairs of plates. The dimensions are shown in Fig. 5-21.

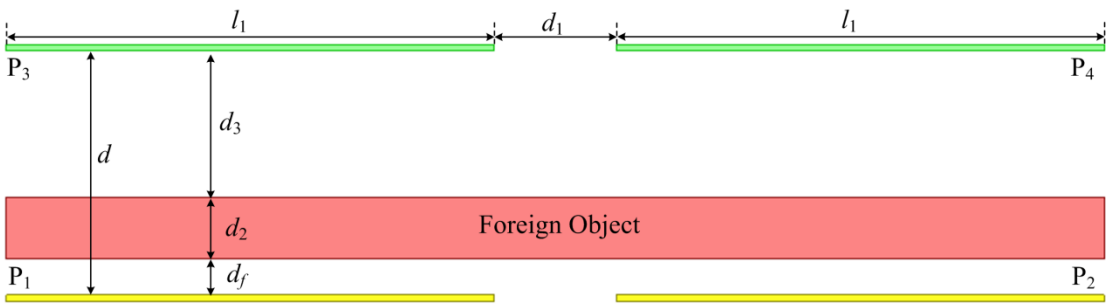

Fig. 5-21. A dielectric foreign object in a horizontal capacitive coupler

The foreign object has the same length as the capacitive coupler. The behavior source model in Fig. 4-3 is used to quantify its influence. When the thickness and material of the dielectric foreign object varies, the Maxwell simulated equivalent capacitances are shown in Fig. 5-22.

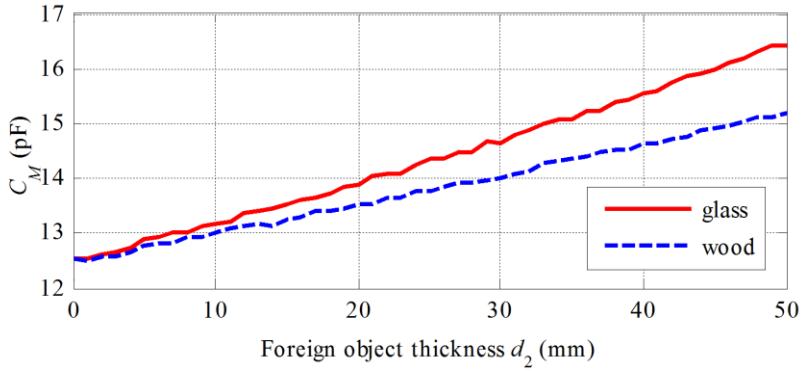

(a) Mutual capacitance C_M

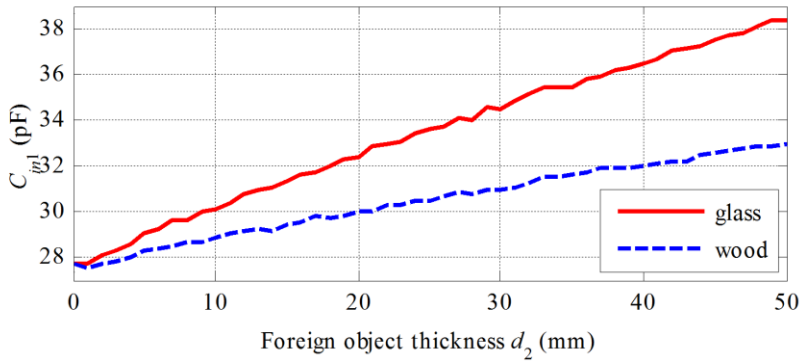

(b) Primary self-capacitance C_{in1}

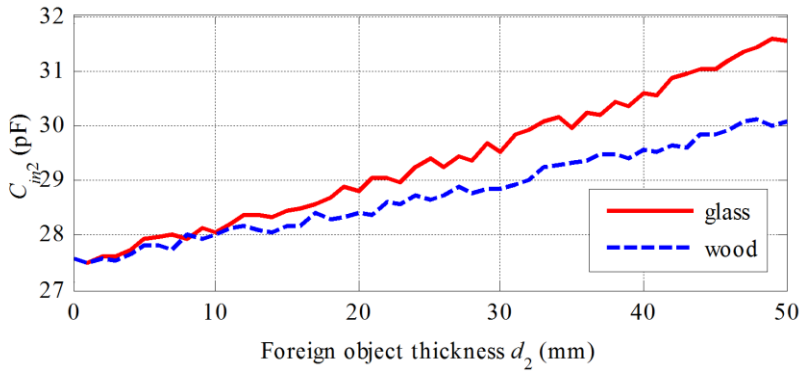

(c) Secondary self-capacitance C_{in2}

Fig. 5-22. Maxwell-simulated equivalent capacitances of a horizontal coupler with a dielectric foreign object

Fig. 5-22(a) shows that the mutual capacitance C_M is increased by the thickness d_2 of the dielectric foreign object. Also, increasing the relative permittivity can also result in an increase of mutual capacitance C_M.

Fig. 5-22(b) and (c) show that the primary and secondary self-capacitances C_{in1} and C_{in2} both increase with the thickness and permittivity of the dielectric foreign object. Since it is closer to the primary plates P_1 and P_2, C_{in1} is more significantly increased.

As a conclusion, in a horizontal capacitive coupler, a dielectric foreign object can increase the coupling capacitances. When the size of the foreign object is large, the capacitances can be significantly increased and the resonances in the circuit are therefore disturbed, which affects the amount of transferred power.

Usually, there are parallel capacitors connected to the same-side plates, such as with the LCLC compensation circuit, which increases the equivalent self-capacitances. The relative variations of capacitances caused by a foreign object, either metallic or dielectric, can be reduced, and the influence to the resonance is then alleviated. This requires studying the sensitivity of the system performance to parameter variations, which can possibly provide a solution to minimizing the foreign object influence through appropriate circuit design. In future research, the sensitivity analysis an corresponding circuit design will be a good area to investigate.

5.5. CPT System Influence to Foreign Object

5.5.1. CPT System Influence to Metallic Foreign Object

Electric fields do not generate significant eddy-current losses in a metallic foreign object, so there is no concern about temperature rise. However, the voltage of a foreign metallic object, which is determined by its position and size, is an important concern. If the metallic foreign object appears on the top or bottom of a capacitive coupler (for example, positions A1, A7, A8, and A11), the aforementioned six-plate coupler structure can help to shield the electric fields, and so its voltage is not affected. If it appears in the air-gap and close to the power transfer plates (for example, positions A2 and A6), its voltage can be close to the plate, which is in the kV range.

In a high-power CPT system, if a human body is grounded and touches the metallic foreign object, there could be current flowing through the body to ground. The magnitude of the current depends on the circuit and the human body impedance. In an LCLC-compensated CPT system,

the circuit topology can be designed to be symmetric in order to reduce the voltages on the plates by half, which can reduce the current flowing through human body as shown in Fig. 5-20.

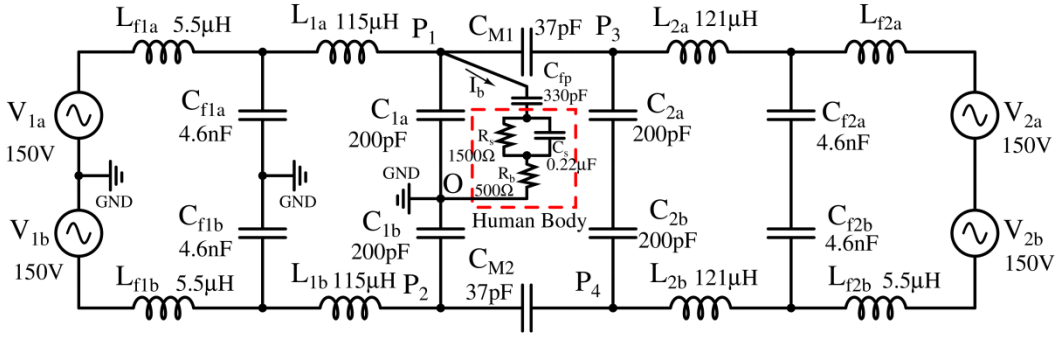

Fig. 5-23. A symmetric circuit topology to reduce current flowing through human body

In Fig. 5-23, due to the symmetry of the circuit topology, the middle point O between C_{1a} and C_{1b} is grounded. In the worst case, the size of a metallic foreign object is as large as the power transferring plate (610mm×610mm) and placed at position A2. Its capacitance C_{fp} with respect to P_1 is therefore about 330pF. The human body model to ground varies depending on position and insulation [11]-[16]. According to the IEC 60990 standard [17], a typical circuit model of the human body is shown in Fig. 5-23. Using this model in circuit analysis, it shows that the appearance of a human body touching the metallic foreign object can disturb the resonance in the circuit. Further circuit simulation shows that the RMS value of current I_b flowing through the human body to ground is 2.2 A. In this case, the CPT system should react to this action and shut down the power transfer process to protect human safety.

According to IEEE C95.6 standard [18], when the frequency is below 3 kHz, there is a dangerous electric shock problem. The current can flow through internal organs, especially the heart, which often leads to irreversible neurological and cardiac damage. The safe limit of low-frequency current in the human body is very strict, which is 0.50 mA.

According to IEEE C95.1 standard [7], when the frequency is higher than 100 kHz, the current flows along the surface of the human body, and there is no internal current [19]-[21]. There is therefore no concern of electric shock. The main concern caused by high-frequency current is the heating effect, which is called “RF burning”. It is required that, over 6 minutes

duration time, the current should be lower than 16.7 mA to avoid apparent heating effect for the touch of general public. For short-time exposure, the maximum energy density during any 100 ms period should be lower than 28.8J/kg [7]. In this CPT system, the induced energy density in human body depends on the contact position and effective time. In practical application, a protection mechanism (for example: 100 ms) is required shut down the system when human touch occurs and it is also an important research area in future work.

There could also be an electric arc or spark when a human touches a metallic foreign object. The maximum suggested RMS value of the plate voltage is limited to140 V to avoid arcing [7]. In future research, the system will be optimized to eliminate this arcing issue.

5.5.2. Conductive Power Losses in Foreign Object

For a foreign object in a CPT system, one critical concern is its temperature rising due to the high-frequency electric fields. The charge relaxation process in the foreign object can induce power loss. According to [22], the charge relaxation time τ_e is expressed as

$$\tau_e = \varepsilon_r \varepsilon_0 / \sigma_0 \,, \tag{5-21}$$

where, σ_0 is the conductivity of the foreign object.

When the relative permittivity ε_r and conductivity $\sigma_0$varies, τ_e is shown in Fig. 5-24.

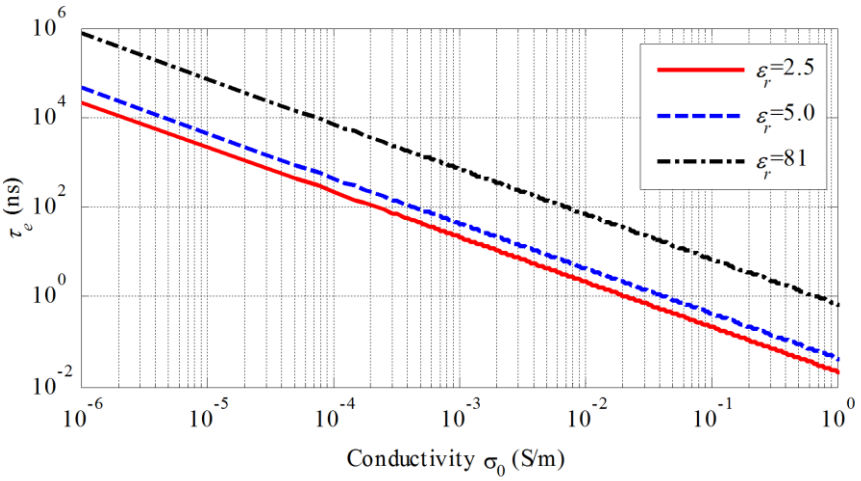

Fig. 5-24. Charge relaxation time of a foreign object at different ε_r and σ_0

Fig. 5-24 shows that the charge relaxation time τ_e increases with increasing ε_r, but decreases with increasing σ_0. In this system, the switching frequency is 1 MHz, resulting in a switching

period of 1000 ns. For a foreign object, if its charge relaxation time τ_e is close to the switching period, the power loss can be significant [22]. For example, for drinking water, if its conductivity is 0.01S/m, its charge relaxation time is about 71.6 ns, which is much smaller than 1000 ns. Therefore, if drinking water appears close to the capacitive coupler, it will essentially behave as a metal object at the 1 MHz operating frequency.

The simple geometry in Fig. 5-19 is used to estimate the power loss in a foreign object. The voltage between the plates is defined as V_{13}, the electric field strength in the air-gap is defined as E_1, the electric field strength in the foreign object is defined as E_2, the charge density on the surface of the foreign object is defined as σ_f, and its conductivity is defined as σ_0. According to [22], their relationships are expressed as,

$$\begin{cases} V_{13} = \vec{E}_1 \cdot (d_3 + d_f) + \vec{E}_2 \cdot d_2 \\ \vec{\sigma}_f = \varepsilon_0 \varepsilon_r \cdot \vec{E}_2 - \varepsilon_0 \cdot \vec{E}_1 \\ d\vec{\sigma}_f / dt = j\omega \vec{\sigma}_f = -\sigma_0 \cdot \vec{E}_2 \end{cases} \tag{5-22}$$

The first equation is the relationship between excitation voltage and the electric field strength, the second equation is Coulomb's law, and the third equation is conservation of charge. Then, the electric field strength in the foreign object is expressed as,

$$\vec{E}_2 = \frac{1}{\left(\varepsilon_r + \dfrac{\sigma_0}{j\omega\varepsilon_0}\right) \cdot (d_3 + d_f) + d_2} V_{13} \tag{5-23}$$

According to [22], the magnitude of E_2 is used to calculate the current density J in the foreign object. Then, the volume power loss density P_D, and the total power loss P_{loss} in the foreign object are further calculated as,

$$\begin{cases} J = \sigma_0 \cdot |E_2| \\ P_D = \dfrac{1}{2} \cdot J^2 / \sigma_0 \\ P_{loss} = P_D \cdot l_1^2 \cdot d_2 \end{cases} \tag{5-24}$$

In this analysis, it needs to be mentioned that the dimensions are l_1=610 mm, d_2=50 mm, d_3=90 mm, and d_f=10 mm. Using (5-23) and (5-24), the power loss in the foreign object can be calculated with different relative permittivity ε_r and conductivity σ_0, as shown in Fig. 5-25.

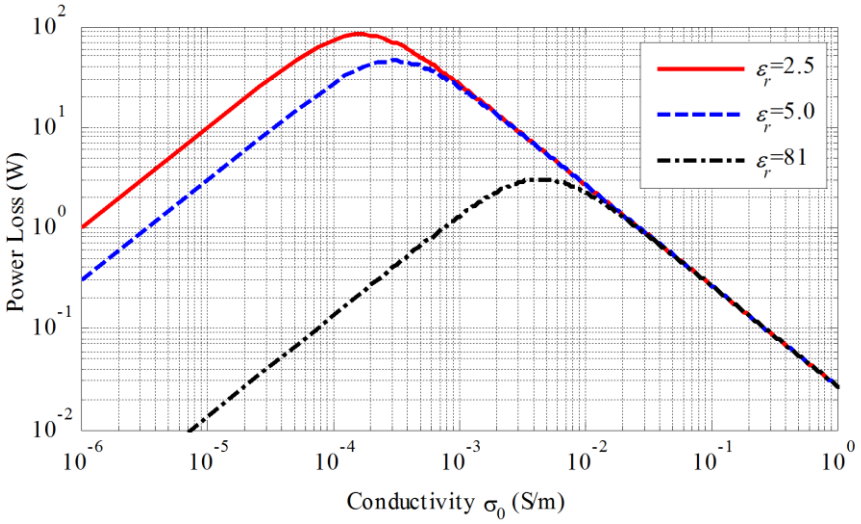

Fig. 5-25. Power losses in a foreign object at different ε_r and σ_0

This shows that the power loss reduces with increasing relative permittivity ε_r. For a given ε_r, while the conductivity σ_0 increases, the power loss first increases and then decreases. If dry wood (ε_r=2.5) is used as the foreign object, since its conductivity is in the range of 10^{-14} to 10^{-16} S/m [23], Fig. 5-25 shows that the induced power loss is less than 0.1 W, which can be neglected. If drinking water (ε_r=81) is used as the foreign object, its conductivity is in the range of 10^{-3} to 10^{-2} S/m [24], Fig. 5-25 shows that the maximum power loss is approximately 3 W. Considering the system power is 3.0 kW, this power loss result in a reduction of system efficiency of about 0.1%, which can be neglected.

Using Newton's law of cooling and assuming the power is dissipated through a free convection process, the temperature rising ΔT is calculated as,

$$\Delta T = \frac{q}{h_c \cdot A} \tag{5-25}$$

where q is the power loss, A is the surface of the foreign object, and h_c is the convection heat transfer coefficient. Using the given dimension, A is calculated as 0.866 m^2. According to [25], h_c can be estimated to be 20 W/(m^2.°C) considering the air flow. Then, the calculated temperature rise of drinking water is about 0.18°C. This analysis represents a worst-case scenario, in which the thickness of the foreign object is as large as 50 mm. In practice, its thickness will likely be much smaller. Then, the power loss and temperature rise is also much smaller.

Further experiments were conducted to test the influence of a foreign object on the CPT system. When a 100 mm×100 mm×300 mm oak wood was placed between the air-gap, there was no apparent influence to the system power and efficiency. After 10 minutes continuous operation, there was no appreciable temperature rise on the surface of the wood. Drinking water was also used as a foreign object in experiments. When four gallons of drinking water was placed between one set of metal plates, there is no apparent influence to the system power and efficiency. However, when one gallon of water was placed between two sets of metal plates, the system power and efficiency are significantly reduced, which means the power transfer process is disturbed. This occurs because the charge-relaxation time-constant of drinking water is much smaller than the switching period, which means drinking water behaves similar to metal. As a result, when water is positioned across both plates, it effectively short-circuits the coupling between primary and secondary. In future research, the influence of foreign object to the CPT system will be studied in detail.

5.6. Conclusion

This chapter presented the study of safety issues in a CPT system, including plate voltages, electric field emissions, and foreign object influence. In a long-distance and high-power CPT system aimed at the electric vehicle charging application, the mutual coupling capacitance is in the tens of pF range, resulting in the voltages of plates in the kV range. These high voltages require reliable insulation on the surface of the metal plates. Also, they can induce strong electric field emissions to the surrounding environment, and the IEEE C95.1 standard requires that the field strength should be lower than 614 V/m at 1 MHz for human safety concern. Further analysis shows that, using a six-plate coupler structure, the safe range of a 3.0 kW CPT system is 120 mm away from the edge of the coupler.

In a practical vehicle charging application, it is common to have metallic or dielectric foreign object. Depending on the size and position, analysis shows that the foreign objects can influence the coupler capacitances. If the variations of capacitances are significant, the

resonances in the circuit can be disturbed and the power transfer process is therefore affected.

The electric fields in a CPT system can also influence the foreign object. For a metallic foreign object, its voltage can be as high as kV level when it is placed on the surface of the coupler. If a human touches it, there could be high-frequency current flowing through the human body. According to the IEEE C 95.1 standard, the high-frequency current does not cause neurological and cardiac damage, but there is heat generated. Then, a protection mechanism is required to act in 100 ms to avoid temperature rise of human body.

For a foreign object, electric fields can generate internal heat, which could cause temperature rise. In worst case, the analysis shows that the power loss in drinking water is about 3.1 W, and the temperature rise is 0.18°C. For dry wood, the power loss and temperature rise can be neglected. Further experiments also validate these analyses.

5.7. References

[1] M. Chabalko, J. Besnoff, M. Laifenfeld, D. Ricketts, "Resonantly Coupled Wireless Power Transfer for Non-Stationary Loads with Application in Automotive Environments," *IEEE Trans. Ind. Electron.*, vol. 64, no. 1, pp. 91-103, 2017.

[2] Y. Su, H. Ma, S. Xie, Y. Zhao, X. Dai, "Analysis on Safety Issues of Capacitive Power Transfer System," *Intern. J. Appl. Electromag. Mechan*., pp. 1-12, 2016, doi: 10.3233/JAE-160046.

[3] F. Lu, H. Zhang, H. Hofmann, C. Mi, "A Double-Sided LCLC-Compensated Capacitive Power Transfer System for Electric Vehicle Charging," *IEEE Trans. Power Electron.*, vol. 30, no. 11, pp. 6011-6014, 2015.

[4] H. Zhang, F. Lu, H. Hofmann, W. Liu, C. Mi, "A Four-Plate Compact Capacitive Coupler Design and LCL-Compensated Topology for Capacitive Power Transfer in Electric Vehicle Charging Application," *IEEE Trans. Power Electron.*, vol. 31, no. 12, pp. 8541-8551, Dec. 2016.

[5] H. Zhang, F. Lu, H. Hofmann, W. Liu, C. Mi, "A Six-Plate Capacitive Coupler to Reduce Electric Field Emission in Large Air-gap Capacitive Power Transfer," *IEEE Trans. Power Electron.*, 2017, doi: 10.1109/ TPEL.2017.2662583.

[6] International Commission on Non-Ionizing Radiation Protection, "*ICNIRP guidelines for limiting exposure to time-varying electric, magnetic and electromagnetic fields* (*1 Hz to 100 kHz*)," Health Phys., vol. 99, pp. 818–836, 2010.

[7] *IEEE Standard for Safety Levels with Respect to Human Exposure to Radio Frequency Electromagnetic Fields*, *3 kHz to 300 GHz*, IEEE Standard C95.1–2005, 2006.

[8] Tipler, Paul A. *College Physics*. Worth, 1987: 467.

[9] D. Rodriguez, R.S. Gorur, P.M. Hansen, "Effect of Humidity on the Breakdown Characteristics of Air in Uniform Field for the very Low Frequency (VLF) Band," *IEEE Trans. Dielec. Elec. Insul.*, vol. 16, no. 5, pp.

1397-1403, 2009.

[10] H. Nishiyama and M. Nakamura, “Form and capacitance of parallel-plate capacitor,” *IEEE Trans. Compon. Packag. Manuf. Tech. A*, vol. 17, no. 3, pp. 477–484, Sep. 1994.

[11] Electrostatic Discharge Association, “Human Body Model (HBM) – Component Level: For Electrostatic Discharge Sensitivity Tesing,” ESDA JS-001-2010.

[12] K. Chinen, I. Kinjo, A. Zamami, J. Irei, K. Nagayama, “New Equivalent-electrical Circuit Model and a Practical Measurement Method for Human Body Impedance,” *Bio-Medical Materials and Engineering*, vol. 26, no. s1, pp. S779-S787, 2015.

[13] V. Santis, P. Beeckman, D. Lampasi, M. Feliziani, “Assessment of Human Body Impedance for Safety Requirements against Contact Current for Frequencies up to 110 MHz,” *IEEE Trans. Bio. Eng.*, vol. 58, no. 2, pp. 390-396, 2011.

[14] N. Cho, J. Yoo, S. Song, J. Lee, S. Jeon, H. Yoo, “The Human Body Characteristics as a Signal Transmission Medium for Intrabody Communication,” IEEE Trans. Micro. Theory Techn., vol. 55, no. 5, pp. 1080-1086, 2007.

[15] C. Nonet, R. Areny, “A Novel Method to Estimate Body Capacitance to Ground at Mid Frequencies,” *IEEE Trans. Instr. Meas.*, vol. 62, no.9, 2519-2525, 2013.

[16] N. Jonassen, “Human Body Capacitance: Static or Dynamic Concept?” Electrical Overstress, pp. 111-117, 1998, doi: 10.1109/EOSESD.1998.737028.

[17] International Electrotechnical Commission, “Method of Measurement of Touch current and Protective Conductor Current,” IEC 60990:1999.

[18] *IEEE Standard for Safety Levels with Respect to Human Exposure to Radio Frequency Electromagnetic Fields, 0–3 kHz*, 2002, IEEE Standard C95.6–2002, 2002.

[19] K. Jokela, L. Puranen, O. Gandhi, “Radio Frequency Currents Induced in the Human Body for Medium-Frequency/High-Frequency Broadcast Antennas,” *Health Phys.*, vol. 66, no. 3, pp. 237-44, 1994.

[20] O. Gandhi, “Electromagnetic Fields: Human Safety Issue,” *Annu. Rev. Biomed. Eng.*, no. 4, pp. 211-234, 2002.

[21] D. Hill, J. Walsh, “Radio-Frequency Current through the Feet of a Grounded Human,” *IEEE Trans. Electromag. Comp.*, vol. EMC-27, no. 1, pp. 18-23, 1985.

[22] Melcher, James R. *Continuum Electromechanics*. Cambridge, MA: MIT Press, 1981.

[23] R.C. Weatherwax, A.J. Stamm, “The Electrical Resistivity of Resin-Treated Wood and Laminated Hydrolyzed-Wood and Paper-based Plastics,” Electrical Engineering, vol. 64, no. 12, pp. 833-838, 1945.

[24] F. Meghnefi, M. Farzaneh, C. Volat, “Measurement of the Evolution of Drippling Water Conductivity of an Ice-Covered Insulator During a Melting Period,” *Proc. Elec. Insul. Dielec. Phen. Conf.*, 236-239, 2008.

[25] A. Samson, T. Torzewicz, T. Raszkowski, “Modeling of Average Radiation and Convection Heat Transfer Coefficient Value in Electronic Systems,” *Proc. Mix. Design. Integ. Cir. Syst. Conf.*, pp. 271-275, 2016.

CHAPTER VI

CONCLUSIONS AND FUTURE WORK

6.1. Conclusions

This dissertation has demonstrated that CPT technology is an effective method to realize high-power and long-distance power transfer for electric vehicle charging applications. Compared to previous CPT technology, the breakthroughs of this work include: increasing transfer power by two orders of magnitude (from several tens of watts to several kW), an increase of transfer distance by two orders of magnitude (from less than 1 mm to hundreds of mm), and an improvement of transfer efficiency (from less than 30% to over 90%). The main contributions and achievements can be summarized in four parts.

First, a double-sided LCLC compensation circuit has been proposed to realize high-power, long-distance, and high-efficiency capacitive power transfer. Two pairs of 610mm×610mm aluminum plates are used as the capacitive coupler. Since the air-gap distance is hundreds of mm, the coupling capacitance is in the pF range. The proposed LCLC compensation circuit can increase the equivalent self-capacitance and establish resonances to increase the system power. The fundamental harmonic approximation (FHA) method is used to analyze the working principle of the proposed circuit, from which the resonance relationships and output power equations are provided. Moreover, a prototype is designed and implemented to validate the circuit. Experimental results show that the prototype can achieve 2.4 kW power transfer across an air-gap distance of 150 mm with a dc-dc efficiency of 90.8%. The LCLC compensation circuit is also compared with the LC compensation circuit. The advantages of LCLC compensation lie in: more flexibility to adjust system power and higher efficiency.

Second, the CPT technology has been combined with IPT technology in a single system. Since IPT technology has been studied for more than 20 years in electric vehicle charging applications, it is ready for commercial products. The combination of CPT technology with IPT can help to extend the usage of this technology. In a combined system, the coupling plates of the CPT system work as compensation capacitors for the IPT system, and the coupling coils of the IPT system work as compensation inductors for the CPT system. In this way, the compensation circuit topology of the combined system is simplified, and the circuit components are better used in the power transfer process. In this dissertation, an LC-compensated IPT-CPT combined system has been proposed and designed as an example to illustrate this idea. The working principle of the combined system is presented in detail. A prototype is further designed and implemented to validate the combined system. Experimental results show that the system output power reaches 2.84 kW, in which the IPT system contributes 72% of the total power and the CPT system contributes the remaining 28%. With the help of the inductive couplings, the efficiency of the combined system is 94.4%.

Third, CPT technology has been applied to realize a dynamic charging system for electric vehicles. Compared to conventional IPT technology, a CPT system does not need high circulating currents to establish magnetic fields. It instead utilizes voltages on metal plates to establish electric fields, and so the power losses in the capacitive coupler can be much lower than the inductive coupler. A long-track CPT system has been proposed, in which the transmitter plates are much longer than the receiver plates and can transfer power to multiple receivers simultaneously. It can also reduce the received power pulsation when the receiver is moving along the transmitter track. A scaled-down prototype is designed and implemented to validate the dynamic CPT system. The length of the transmitter plate is 1200 mm, and the length of the receiver plate is 300 mm. Experimental results show that the dynamic CPT system can achieve 154.7W power transfer across an air-gap distance of 50 mm with a dc-dc efficiency of 85.4%. When the receiver moves along the transmitter, the power pulsation is within ±4.0% of the nominal power. Also, the proposed dynamic CPT system has good misalignment performance.

Fourth, a safety study of the CPT system was conducted. The safety issues in a CPT system include four aspects: high voltage between plates, electric field emissions, foreign object influence on a CPT system, and the CPT system influence on a foreign object. The theoretical principle of capacitive power transfer is derived, which shows that the transfer power is proportional to the switching frequency, mutual capacitance, and the voltages between plates. When the mutual capacitance is in the pF range, the plate voltages are required to be in the kV range in order to achieve kW power transfer. Therefore, there should be reliable insulation on the surface of the metal plates. Since the air-gap distance in electric vehicle charging application is in the hundreds of mm range, there is a large amount of leakage electric flux emitted to the surrounding environment, which can cause electromagnetic interference (EMI). According to the IEEE C95.1 standard, the electric field strength has to be limited below 614V/m at 1 MHz for human health consideration. A six-plate coupler structure has been proposed to reduce the electric field emissions, and the safe range is about 120 mm away from the edge of the capacitive coupler. This work also shows that the appearance of foreign objects in a CPT system can change the coupling capacitance. The capacitance variation can then disturb the resonances and reduce power. The electric fields can also influence the foreign object. For a metallic foreign object, its voltage can increase to kV, and cause high current flowing through a human body when touched, which can cause heating problem. A protection mechanism is required to shut down the system quickly in order to avoid danger. For a dielectric foreign object, there is temperature rise. However, it is shown that the temperature rise is limited to 0.18°C in a 3.0 kW CPT system.

6.2. Future Works

Although this work has accomplished some significant achievements, there is still plenty to be investigated before CPT technology comes to real life applications. There are four major directions for future research: a generalized circuit design method of the compensation network for a CPT system, a more compact and efficient coupler structure to improve system power density, the consequences of increasing the system switching frequency, and further improving

the safety properties of CPT systems in a practical application.

First, a generalized method to design compensation circuit for a CPT system needs to be derived. This paper proposes a double-sided LCLC circuit topology and compares it with the double-sided LC compensation. It is straightforward to add more LC networks to the compensation circuit, which requires studying the influence of these multiple networks to the CPT system property. Future research should determine the optimal number of LC compensation circuits to maximize system power and efficiency.

Second, the power density of a CPT system can possibly be improved through the coupler structure design. The power density of the designed CPT system is about 2kW/m^2, which is still not comparable to that of an IPT system (30kW/m^2 or even higher). Considering the IPT-CPT combined system in this dissertation, the integration of inductive and capacitive coupler is an effective method to improve the system power density. In this way, the electric and magnetic fields concentrate in a single coupler. The resulting coupler structure should be optimized to minimize power losses.

Third, higher switching frequencies result in higher power and reduced-size passive components. With the continuing development of semiconductor devices, it is expected to have high power devices with tens or even hundreds of MHz switching capability in the near future. However, high frequency operation can induce more radiation loss to the surrounding environment, which reduces the system efficiency and create safety issues. Especially in the dynamic CPT system, where the transmitter plate length can be tens or even hundreds of meters, increasing the switching frequency is more challenging, due to the effects of parasitic inductance.

Fourth, the safety of a CPT system should be further improved. The high voltages on the power transfer plates are the cause of the safety issues, which include potential electric shock, electric field emissions, and foreign object influence. Therefore, measures need to be taken to reduce the plate voltages, such as increasing the mutual capacitance or increasing the switching frequency, which will cause other side effects. Therefore, further research is needed to resolve the conflict between high voltage and safety requirements.

In summary, CPT technology has been developed for high-power and long-distance applications. It has been shown to be a viable alternative to conventional IPT technology. In the future, more effort should be conducted to improve its power density, efficiency, and safety for real life applications.